UNIVERSITÀ DEGLI STUDI DI PADOVA

DIPARTIMENTO DI FISICA e ASTRONOMIA "GALILEO GALILEI"

Scuola di dottorato di ricerca in fisica
Ciclo XXVIII

Study of multiple vertices neutrino interactions in the OPERA experiment

Doctoral dissertation of
Marco Roda

Director of the doctoral school: **Prof. Andrea Vitturi**

Supervisor: **Dott. Alessandro Bertolin**

to my sister Lisa

Summary

OPERA is a long baseline neutrino experiment designed for ν_τ searches in an almost pure ν_μ beam. The detection is performed on an event-by-event basis which is possible thanks to the high spatial resolution of the detector. In fact, the set-up is able to observe very short decaying particles produced in neutrino interactions, such as tau or charmed particles. In particular, the experiment searches for events with one secondary vertex within 1 mm from the primary one.

An event was recorded with an unexpected topology: instead of one secondary vertex it has two. Such an event was completely unexpected and a totally new analysis was required in order to understand its nature. The possibilities taken into account include most of the combinations of tau, charmed particle and hadron re-interaction within the lead.

The new software, based on GEANT4, was set-up and successfully tested using a dedicated OPERA test beam. Thus, an ad hoc Monte Carlo generation was prepared in order to describe the properties of such a rare observation. Finally, a sample having the interesting topology was obtained and a blind procedure for the event identification could be developed.

The event turned out to be very likely an ν_τ interaction with charm production with a significance close to $3.5\,\sigma$.

Riassunto

OPERA è un esperimento per lo studio di neutrini da fascio progettato per ricerca di ν_τ in un fascio quasi puro di ν_μ. La ricerca è basata su un'analisi evento per evento che è resa possibile dall'elevata risoluzione spaziale del rivelatore. Infatti, l'apparato è in grado di osservare particelle emesse durante un'interazione di neutrino che decadono entro brevi distanze. In particolare, l'esperimento ricerca eventi che presentano vertici secondari entro circa un millimetro dal vertice primario di interazione.

Un evento interessante è stato osservato con una topologia inaspettata: invece un solo vertice secondario ne sono stati osservati due. Questo tipo di eventi era completamente inaspettato e una nuova analisi era necessaria per capire la natura dell'evento. Le possibilità considerate includono quasi tutte le combinazioni di tau, particelle charmate e reinterazioni adroniche nel piombo.

Un nuovo algoritmo di simulazione, basato su GEANT4, è stato sviluppato e testato con successo usando i dati di uno dei test beam di OPERA. Quindi, una nuova produzione Monte Carlo è stata preparata per poter descrivere le proprietà di questo raro fenomeno. Infine, è stata preparata un'analisi per l'identificazione dell'evento osservato.

L'evento è risultato essere molto probabilmente un'interazione di ν_τ con produzione di charm, con una significanza di quasi $3.5\,\sigma$.

Contents

Introduction

Neutrinos are some of the most fascinating particles of the Standard Model (SM) of particle physics and, together with photons, they are the most abundant particles in the whole universe. Such a kind of particles was predicted for the first time in 1930 by Wolfgang Pauli [1], but physicists managed to reveal them only in 1956 [2]. Pauli postulated the existence of a neutral particle with a very small mass in order to explain the continuous electron energy spectrum found in β decays and called it neutron.

In 1932, Chandwick discovered what we now call neutron [3], as a neutral component of the nucleus. Its mass was close to the proton one, which was by far too large for Pauli's neutron and Fermi proposed to call the missing particle of the β decay *neutrino*.

With the first nuclear power plants, neutrino detection could finally happen. This was done in the Savannah River Site according to the reaction

$$\overline{\nu} + p \rightarrow n + e^{+} \ .$$

The experimental set-up consisted of 400 liters of water and cadmium chloride. Neutrinos interacted with the target protons yielding a neutron and a positron in the final state. The target was surrounded by scintillators that detected the photons from positron annihilation and neutron capture. Once neutrinos had been detected the study of their properties could actually start.

Nowadays neutrinos are studied using all kinds of sources: reactor power plants, the Sun, neutrino beams from decay of accelerated pions, cosmic neutrinos and even neutrinos produced from the Earth crust and mantle. Phenomenology and detection procedures are extremely different depending on neutrino energies and on the neutrino flavour which has to be detected. The only common point, is that they all are very massive experiments in order to supply with luminosity to the low neutrino cross section with matter.

This work proposes the first analysis procedure to be applied to multiple secondary vertices events within the OPERA experiment. The analysis aims to identify heavy particles that can be produced via neutrino interactions within the experiment. Chapter 1 is a general overview of the established theoretical and experimental understanding of neutrino physics. Chapter 2 describes OPERA, its usual procedures and analysis stream. In chapter 3 the observed event that motivated this work is described in detail and the

main purpose of the following analysis is discussed. The analysis required the development of a completely new simulation and part of it was tested using a dedicated test beam, whose results are presented in chapter 4. Finally, chapters 5 and 6 present the actual analysis dedicated to multiple secondary vertices interactions.

Chapter 1

Neutrino physics

Neutrinos are neutral fermions with half integer spin which interact only through weak interaction and gravity. Their mass is much smaller compared to all the other known particles and, so far, all experiments have been able to set only upper limits, that's why they were thought to be massless for a long time.

Nowadays, three different types of neutrinos were observed and they all were successfully included in the Standard Model (SM) of particles physics, as massless particles. Recently, the discovery of neutrino oscillations [4] required extensions of the SM in order to allow neutrinos to be massive.

This chapter presents a general overview of the theory related to neutrino oscillation, after a brief description of neutrino in the SM. Then, some major experiments related to neutrino physics will be presented and their results discussed.

1.1 Neutrinos in Standard Model and beyond

The Standard Model is a very successful model which is able to describe a large variety of processes observed in particle physics experiments, the last being the Higgs particle discovery [5].

The SM is a chiral model, which means that the right-handed and left-handed parts of a spinor field could be treated separately. Only left-handed neutrinos are inserted in the standard model because interacting neutrinos are observed to be always left-handed [6]. Also, neutrinos are not inserted as stand-alone fields, but they are defined in lepton doublets, which are left-handed:

$$(L_\alpha)_L \equiv \begin{pmatrix} \nu'_\alpha \\ \ell'_\alpha \end{pmatrix}_L = \frac{1-\gamma^5}{2} \begin{pmatrix} \nu'_\alpha \\ \ell'_\alpha \end{pmatrix} \tag{1.1}$$

where the ℓ'_α fields are related to the charged leptons. The SM contains three copies of this structure. Naively, it could be said that there is one copy for each known charged lepton, but this is not true: at this stage the three copies

are not the physical observed fields. These doublets are all subject to the same gauge transformation of $SU(2) \otimes U(1)_Y$, with $Y = -\frac{1}{2}$. In this very convention, the Higgs doublet has $Y = \frac{1}{2}$.

Once the spontaneous symmetry breaking mechanism has been applied, the following neutrinos couplings with the gauge bosons are created [7]:

$$\mathcal{L}_W^\nu = \frac{g}{\sqrt{2}} W_\mu^+ \sum_\alpha \overline{\nu'_L}^{\,\alpha} \gamma^\mu \ell'^{\,\alpha}_L + \frac{g}{\sqrt{2}} W_\mu^- \sum_\alpha \overline{\ell'_L}^{\,\alpha} \gamma^\mu \nu'^{\,\alpha}_L \tag{1.2}$$

$$\mathcal{L}_Z^\nu = \frac{g}{2\cos\theta_W} Z_\mu \sum_\alpha \overline{\nu'_L}^{\,\alpha} \gamma^\mu \nu'^{\,\alpha}_L \tag{1.3}$$

where g is the $SU(2)$ coupling constant and θ_W is the Weinberg's angle. It's important to note that these fields are not physical since their masses are not yet defined.

The SM on its own is not able to allow mass term for neutrinos. In section 1.2.1 it will be shown that massless neutrinos can not oscillate. This means that the SM has to be extended in order to predict this kind of phenomenology.

1.1.1 Mechanisms for neutrino masses

There are several ways to create massive neutrinos starting from the SM. The general procedure is to obtain effective couplings such as a Dirac mass term

$$m \left(\overline{\nu}_L \nu_R + \overline{\nu}_R \nu_L \right) \tag{1.4}$$

or a Majorana mass term

$$\frac{m}{2} \left(\overline{\nu^c_L} \nu_L + \overline{\nu}_L \nu^c_L \right) \quad \text{or / and} \quad \frac{m}{2} \left(\overline{\nu^c_R} \nu_R + \overline{\nu}_R \nu^c_R \right) \tag{1.5}$$

where $\nu^c \equiv \mathscr{C} \overline{\nu}^T$ and $\mathscr{C}$ is the charge conjugation matrix [8, Section 2.11.1].

It's interesting to notice that, so far, neutrinos are the only particles which could get the mass from the Majorana mechanism, since they are the only known elementary neutral fermions. Experiments designed to proof the Majorana nature of neutrino mass are ongoing: they look for neutrino-less double beta decay, but none of them has been conclusive and both Dirac and Majorana mass terms can still be taken into account.

Regardless of the underlying mechanism that produces such mass terms, the implementation in the SM in not trivial. In fact, all new fields and all new couplings must respect the SM gauge group. The mechanisms proposed to describe neutrino masses can be grouped in three different categories.

Pure Dirac mass

The simplest possibility is the addition of three right-handed neutrino fields which do not transform under any of the SM gauge symmetries, which means

adding three sterile neutrinos. These fields are going to be used to build Dirac's mass terms. This is very simple but also extremely unsatisfactory since this extension of the SM can not predict the neutrino mass smallness with respect to other particles, which is one of their main features. A complete derivation of the Dirac neutrino masses can be seen in section 1.1.2.

Pure Majorana mass

Giving up the SM restriction on couplings of the 5^{th} order or more on the masses, the SM itself, without any other new field, could provide Majorana mass terms for neutrinos. The paradigm for this scenario is given by couplings between the Higgs doublet and the lepton doublets such as $\overline{L_{_L}^c} H H L_{_L}$: such kind of terms produces Majorana mass terms after the Higgs spontaneous symmetry breaking and the value of the neutrino mass is proportional to the coupling constant of these terms. This could provide an explanation for the low neutrino masses since the coupling constants would have the dimension of an inverse mass. In fact, this dimensional coupling constant is interpreted as a remnant of a higher energy scale particle which behaves like a suppression factor at the energies achieved so far. Of course, the introduction of Lagrangian terms of order higher than 4 implies that the model is not re-normalizable.

See-Saw mechanism

Exploring the possibilities offered by new physics, the see-saw mechanism can both explain the smallness of neutrino masses and the only presence of left-handed active neutrinos. The main idea can be explained using a one generation neutrino case, in which there are both Majorana and Dirac mass terms. Furthermore, a heavy right-handed neutrino is required. In this case the most general mass term is:

$$\mathcal{L}_m = \begin{pmatrix} \overline{\nu}_{_L} & \overline{\nu}_{_R} \end{pmatrix} \begin{pmatrix} 0 & m \\ m & M \end{pmatrix} \begin{pmatrix} \nu_{_L} \\ \nu_{_R} \end{pmatrix} \quad \text{with} \quad M \gg m \tag{1.6}$$

where the left-handed Majorana mass term is zero because it is forbidden by SM symmetries. This is close to the SM case, since there is no way to create a Majorana mass with left-handed neutrinos as they come in $SU(2)$ doublet. At the same time, it is possible to create all the other couplings just adding a new $\nu_{_R}$ sterile field, since $\nu_{_R}$ is not related to any of the gauge groups.

Once these couplings have been diagonalized, two different mass eigenstates will be obtained:

$$|m_1| \simeq \frac{m^2}{M} \tag{1.7}$$

$$m_2 \simeq M \tag{1.8}$$

where the m_1 eigenvector is mainly composed be the left-handed neutrinos, and the m_2 eigenvector is almost equal to the right-handed one. This is known as type I see-saw mechanism [9].

There are two other types of see-saw: they all require new physics in the form of a Higgs triplet (type II) [10] or of a fermion triplet (type III) [11]. The new physics has to be related to higher energy scales in order to guarantee high mass for the triplets. Of course the complete implementation in the SM is much more complicated because it has to take into account the three generation of leptons and it is not discussed in this work.

1.1.2 Neutrino masses

Once a neutrino right-handed singlet has been defined, as a $\nu_{_R}$ or a charge conjugated $\nu_{_L}$, it is possible to construct mass terms for neutrinos. For simplicity, the construction will be presented using a right handed neutrino.

The possible terms that can lead to a neutrino mass are contained in the Yakawa couplings of the lepton doublets with the Higgs doublet:

$$\mathcal{L}_{LH\nu} = -\sum_{\alpha,\beta}\left(\lambda_{\alpha\beta}\overline{L}_{_L}^{\alpha}\widetilde{H}^{c}\nu_{_R}^{\prime\,\beta} + \text{h.c.}\right) \tag{1.9}$$

where $\widetilde{H}^c = i\sigma_2 H^*$ and $\sigma_2 = \begin{pmatrix} 0 & -i \\ i & 0 \end{pmatrix}$, while H is the Higgs doublet. The Yukawa coupling matrix λ can be a general complex matrix. After the symmetry braking, these terms can be split:

$$\mathcal{L}_{LH\nu} = \mathcal{L}_{\nu}^{m} + \mathcal{L}_{\nu H} \tag{1.10}$$

$$\text{and} \quad \mathcal{L}_{\nu}^{m} = -\frac{v}{\sqrt{2}}\sum_{\alpha,\beta}\left(\lambda_{\alpha\beta}\overline{\nu_{_L}^{\prime}}^{\alpha}\nu_{_R}^{\prime\,\beta} + \lambda^{*}_{\beta\alpha}\overline{\nu_{_R}^{\prime}}^{\alpha}\nu_{_L}^{\prime\,\beta}\right) \tag{1.11}$$

where $\frac{1}{\sqrt{2}}\begin{pmatrix} 0 \\ v \end{pmatrix}$ is the vacuum expectation value of the Higgs field and $\mathcal{L}_{\nu H}$ is a term which contains the interactions between the Higgs particle and the neutrinos.

Given a general complex matrix M, with $\det M \neq 0$, there are two unitary matrices, namely U_ℓ and U_r, such as $U_\ell^\dagger M U_r = D$ where $D_{ij} = d_i\delta_{ij}$ and the d_i are real and positive, see [12]. This means that the mass terms can be diagonalized:

$$\mathcal{L}_{\nu}^{m} = -\frac{v}{\sqrt{2}}\sum_{\alpha,\beta,i,j}\left(\overline{\nu_{_L}^{\prime}}^{\alpha}U_{\ell}^{\alpha i}d_{ij}U_{r}^{\dagger\,j\beta}\nu_{_R}^{\prime\,\beta} + \text{h.c.}\right) \tag{1.12}$$

$$= -\sum_{i=1}^{3} m_i\left(\overline{\nu}_{_L\,i}\nu_{_R\,i} + \overline{\nu}_{_R\,i}\nu_{_L\,i}\right) \tag{1.13}$$

where some new physical fields were defined, namely

$$\nu_{L}^{i} \equiv \sum_{j=1}^{3} U_{\ell}^{\dagger ij} \nu_{L}^{\prime j} \qquad \nu_{R}^{i} \equiv \sum_{j=1}^{3} U_{r}^{\ ij} \nu_{R}^{\prime j} \tag{1.14}$$

which have defined masses equal to $m_i = d_i \frac{v}{\sqrt{2}}$.

1.1.3 Lepton Masses

Also for the charged leptons, there is the same mass eigenstate definition problem. In this case, the procedure is even more straightforward than in the neutrino case, since the only way to produce mass terms is trough a Dirac mechanism. Once again a coupling between the lepton doublets and the Higgs doublet is required:

$$\mathcal{L}_{LHl} = -\sum_{\alpha\beta} \left(\Gamma_{\alpha\beta} \overline{L}_{L}^{\alpha} H \ell_{R}^{\prime \beta} + \text{h.c.} \right) \tag{1.15}$$

where Γ is the matrix of all the possible Yukawa couplings. After the spontaneous symmetry breaking these terms give origin to mass terms and to lepton-Higgs couplings:

$$\begin{aligned} \mathcal{L}_{LHl} &= -\frac{v}{\sqrt{2}} \sum_{\alpha\beta} \left(\Gamma_{\alpha\beta} \overline{\ell_{L}^{\prime}}^{\alpha} \ell_{R}^{\prime \beta} + \text{h.c.} \right) + \mathcal{L}_{\ell H} & (1.16) \\ &= -\sum_{\alpha=e,\mu,\tau} M_{\alpha} \left(\overline{\ell}_{L}^{\alpha} \ell_{R}^{\alpha} + \overline{\ell}_{R}^{\alpha} \ell_{L}^{\alpha} \right) + \mathcal{L}_{\ell H} & (1.17) \end{aligned}$$

Once again, the Yukawa coupling terms were diagonalized and the new definitions of the physical leptons are:

$$\ell_{L}^{\alpha} \equiv \sum_{\beta=1}^{3} V_{\ell}^{\dagger \alpha\beta} \ell_{L}^{\prime \beta} \qquad \ell_{R}^{\alpha} \equiv \sum_{\beta=1}^{3} V_{r}^{\ \alpha\beta} \ell_{R}^{\prime \beta} \tag{1.18}$$

where V_ℓ and V_r are unitary matrix such that $V_\ell^\dagger \Gamma V_r = D$ and $D_{\alpha\beta} = M_\alpha \delta_{\alpha\beta}$.

1.1.4 Mixing

The new fields definitions obtained in equations 1.14 and 1.18 have to be applied to the remaining part of the SM Lagrangian. The kinematic terms are invariant under U or V transformations and so are the couplings with the Z boson (equation 1.3) and the photon: this is a general feature of neutral current SM interactions [13].

What is not invariant is the coupling with the W, equation 1.2. Using the physical fields, the final form of the W couplings between neutrinos and charged leptons is then:

$$\mathcal{L}_{W}^{\nu} = \frac{g}{\sqrt{2}} W_{\mu}^{+} \sum_{\alpha,i} \overline{\nu}_{L}^{i} U^{\dagger i\alpha} \gamma^{\mu} \ell_{L}^{\alpha} + \frac{g}{\sqrt{2}} W_{\mu}^{-} \sum_{\alpha,i} \overline{\ell}_{L}^{\alpha} \gamma^{\mu} U^{\alpha i} \nu_{L}^{i} \tag{1.19}$$

where a new matrix $U \equiv V_\ell^\dagger U_\ell$ were defined, which is known as the PMNS[1] matrix.

The PMNS matrix is, in general, a $N \times N$ unitary matrix and therefore it has N^2 degrees of freedom divided in $\frac{N(N-1)}{2}$ angles and $\frac{N(N+1)}{2}$ phases. Not all the phases are physical since some of them can be reabsorbed through a redefinition of the leptons fields[2], in the form $\psi \to e^{i\phi}\psi$. The number of physical phases for Dirac neutrinos is then $\frac{(N-1)(N-2)}{2}$. In case of Majorana neutrinos there are $N-1$ other phases that cannot be reabsorbed. A detailed description of the degrees of freedom of the PMNS matrix can be found in [8, Section 6.7.3]. Finally, the usual parameterization of the PMNS matrix, with only Dirac phases, is:

$$U^D \equiv \begin{pmatrix} 1 & 0 & 0 \\ 0 & c_{23} & s_{23} \\ 0 & -s_{23} & c_{23} \end{pmatrix} \begin{pmatrix} c_{13} & 0 & s_{13}e^{-i\delta} \\ 0 & 1 & 0 \\ -s_{13}e^{i\delta} & 0 & c_{13} \end{pmatrix} \begin{pmatrix} c_{12} & s_{12} & 0 \\ -s_{12} & c_{12} & 0 \\ 0 & 0 & 1 \end{pmatrix} \quad (1.20)$$

where $s_{ij} = \sin\theta_{ij}$ and $c_{ij} = \cos\theta_{ij}$.

These results was presented using a pure Dirac mass mechanism, but a PMNS matrix occurs whatever is the mass source. The only difference appears in presence of Majorana phases: in this case the usual parameterization of the PMNS matrix has the form

$$U \equiv U^D U^M = U^D \begin{pmatrix} 1 & 0 & 0 \\ 0 & e^{i\lambda_2} & 0 \\ 0 & 0 & e^{i\lambda_3} \end{pmatrix} \quad (1.21)$$

From now on, neutrino mass eigenstates will be identified using Latin letter subscripts, like ν_i, while flavour eigenstates will be labelled using Greek letter subscripts, ν_α. The relationships between these states are given by the first Charge Current coupling terms of equation 1.19: they are

$$\nu_\alpha = \sum_i U^*_{\alpha i}\,\nu_i \quad \text{and} \quad \nu_i = \sum_\alpha U_{\alpha i}\,\nu_\alpha\ . \quad (1.22)$$

From the same Lagrangian term it is possible to derive the same transformations for anti-neutrinos:

$$\overline{\nu}_\alpha = \sum_i U_{\alpha i}\,\overline{\nu_i} \quad \text{and} \quad \overline{\nu_i} = \sum_\alpha U^*_{\alpha i}\,\overline{\nu}_\alpha\ . \quad (1.23)$$

The PMNS matrix has a counterpart in the quark sector: the CKM[3] matrix. Although the construction of the CKM matrix is very similar to the lepton mixing matrix, the phenomenology is completely different due to the odd neutrinos properties. A very interesting fact is that the two mixing matrices have very different shapes: the CKM one is almost diagonal while in the PMNS matrix all the angles have been found to be surprisingly large.

[1] Pontecorvo–Maki–Nakagawa–Sakata

[2] the number of reabsorbed phases is $2N-1$

[3] Cabibbo – Kobayashi – Maskawa

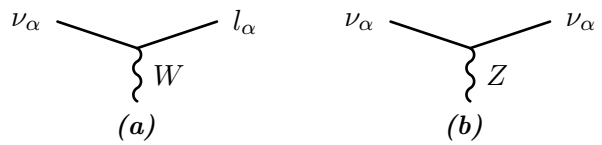

Figure 1.1: *Partial Feynman diagrams for neutrino or anti-neutrino interactions: Charged Current (a) and Neutral Current (b). The Lagrangian terms for the CC interaction diagram can be seen in equation 1.19.*

Lepton number violation

The SM presents global continue symmetries which were not requested during construction. The Noether theorem assures there are conserved quantities associated to each of these symmetries. In particular, the SM has three conserved lepton numbers, L_e, L_μ, L_τ, one for each observed flavor. They are defined as

$$L_\alpha \equiv N_{\ell_\alpha} + N_{\nu_\alpha} - N_{\overline{\ell_\alpha}} - N_{\overline{\nu_\alpha}} \tag{1.24}$$

The introduction of a mixing matrix breaks these three global symmetries and only one is left: $L \equiv L_e + L_\mu + L_\tau$. The presence of Majorana mass terms also induces a violation of the lepton number, since the mass term itself is a lepton number violating term with $\Delta L = 2$. Anyway, such a kind of process is yet to be observed.

1.1.5 Neutrino interactions

From the interaction point of view, neutrinos can be treated as massless particles of a defined flavour. Neutrino can interact only through W exchange, which leads to a Charge Current (CC) interaction, or Z exchange, which is the so called Neutral Current (NC) interaction. The basic diagrams can be seen in Figure 1.1. Due to this high mass boson exchange, neutrino interactions are extremely weak. In real neutrino experiments, these W and Z can be coupled only with ordinary matter: nuclei and electrons.

The possible processes which can be triggered by a neutrino depend on the neutrino energy and determine the experimental technique used for the detection. Here is a list of relatively common neutrino processes ordered by increasing threshold.

NC nuclear recoil happens at low energy neutrino, typically $E \lesssim 50$ MeV, for medium A nuclei. This is the dominant process at these energies by about one order of magnitude, but it is very difficult to detect since it only produces very small recoils. Anyway, such a process is extremely interesting since it has no lower threshold.

ν_e CC on neutron is the typical ν_e CC interaction and the complete reaction can be written as $\nu_e + n \to e^- + p$. This process has no threshold on free neutrons. On other specific nuclei, mostly meta-stable, if the final proton is not ejected, the reaction can be exothermic.

Neutrino elastic scattering on electron is available for both neutrino and anti-neutrino. It is not a pure CC or NC interaction since it is the interference of the two processes. The CC diagrams are different between neutrinos (Figure 1.2b) and anti-neutrinos (Figure 1.2c) while the NC one is the same (Figure 1.2a). The threshold of this process is due to the bounding energy between the electron and the nucleus: this is within 10 and 100 keV.

$\overline{\nu}_e$ CC on proton is the typical $\overline{\nu}_e$ CC interaction and the complete reaction is $\overline{\nu}_e + p \to e^+ + n$. With respect to his neutrino version, it has a threshold of 1.8 MeV on free protons due to the mass difference between protons and neutrons and also to the positron production. On nucleus bounded protons the threshold can be higher.

Neutrino Quasi-Elastic scattering is the dominant reaction near the threshold point of CC interactions. For neutrino, it can be summarized as $\nu_\alpha + n \to \ell_\alpha^- + p$ while for anti neutrino it is $\overline{\nu}_\alpha + p \to \ell_\alpha^+ + n$. If the initial nucleon is inside a nucleus the outgoing nucleon will be expelled. The threshold depends on the neutrino flavour: it is in tens of MeV range for the electron, about hundred MeV for muons and 3.5 GeV for taus. The final state baryon can be also a Λ^0 particle (for anti-neutrino) or a Λ_c^+ (for neutrino).

Deep Inelastic Scattering (DIS) can be summarized as $\nu_\alpha + N \to \ell_\alpha + X$ for both neutrinos and anti-neutrinos, where at least a new hadron is created in the final state. These are the dominant processes at energies far from the threshold of the CC scattering. In this regime, neutrinos are sensitive also to the sea quark inside the nucleus and strange or charmed particles can be produced in the final state. There is also a NC version of this process, with slightly lower thresholds.

1.2 Neutrino oscillation theory

Since its discovery in 1998, neutrino oscillations are among the most established phenomena that occur beyond the standard model and, so far, oscillations are also our more effective tool for the investigation of the lepton sector. They occur since the neutrino flavours have no defined mass and so they are not eigenstates of the free Hamiltonian. This can not be avoided, because the neutrino flavour is the only property which can be measured

when a neutrino is produced: it is the flavour of the lepton produced at the same time with the neutrino.

1.2.1 Neutrino oscillations in vacuum

The propagator of a mass eigenstate neutrino $|\nu_j\rangle$, with energy E in the laboratory frame is given by:

$$|\nu_j(t,L)\rangle = e^{-iEt+ip_jL}\,|\nu_i(0,0)\rangle \tag{1.25}$$

While E is the same, regardless of the mass of the eigenstate, p_j depends on the mass value:

$$\begin{aligned} p_j &= \sqrt{E^2-m_j^2} && (1.26)\\ &\simeq E-\frac{m_j^2}{2E} && (1.27)\end{aligned}$$

such that

$$Et-p_jL \simeq E(t-L)+\frac{L}{2E}m_j^2 \tag{1.28}$$

Now that the propagation for Hamiltonian eigenstates is defined, it is possible to provide the evolution of a flavour defined neutrino with energy E:

$$\begin{aligned} |\nu_\alpha(t,L)\rangle &= \sum_{j=1}^{3} U_{\alpha j}^*\,|\nu_j(t,L)\rangle && (1.29)\\ &= e^{-iE(t-L)}\sum_{j=1}^{3} U_{\alpha j}^* e^{-i\frac{L}{2E}m_j^2}\,|\nu_j(0,0)\rangle && (1.30)\\ &= e^{-iE(t-L)}\sum_{j=1}^{3}\sum_{\gamma=e,\mu,\tau} U_{\alpha j}^* e^{-i\frac{L}{2E}m_j^2}U_{\gamma j}\,|\nu_\gamma(0,0)\rangle && (1.31)\end{aligned}$$

Thus, the transition amplitude $\nu_\alpha \to \nu_\beta$ is given by:

$$\begin{aligned} \mathcal{A}_{\alpha\to\beta}(E,L) &= \langle\nu_\beta(0,0)|\nu_\alpha(t,L)\rangle && (1.32)\\ &= e^{-iE(t-L)}\sum_{j=1}^{3} U_{\alpha j}^* e^{-i\frac{L}{2E}m_j^2}U_{\beta j} && (1.33)\end{aligned}$$

Note that $E(t-L)$ is simply a global phase, not physical, that's why t has not been inserted in the $\mathcal{A}_{\alpha\to\beta}$ dependencies. Finally, the probability of the $\alpha\to\beta$ transition is given by:

$$\begin{aligned} \mathscr{P}_{\alpha\to\beta}(E,L) &= |\mathcal{A}_{\alpha\to\beta}(E,L)|^2 && (1.34)\\ &= \delta_{\alpha\beta}-4\sum_{j<k}\mathfrak{Re}\left[U_{\alpha j}U_{\beta j}^*U_{\alpha k}^*U_{\beta k}\right]\sin^2\left(\frac{\Delta m_{jk}^2\,L}{4E}\right)\\ &\quad +2\sum_{j<k}\mathfrak{Im}\left[U_{\alpha j}U_{\beta j}^*U_{\alpha k}^*U_{\beta k}\right]\sin\left(\frac{\Delta m_{jk}^2\,L}{2E}\right) && (1.35)\end{aligned}$$

where $\Delta^2_{ij} \equiv m^2_i - m^2_j$. In case of massless neutrinos, oscillation can not occur since all the Δ^2_{ij} are zero and so are the transition probabilities.

For anti-neutrino the oscillation formula is different and, in particular, the anti-neutrino oscillation process is the CP transformed of equation 1.35. From equations 1.22 and 1.23 the CP transformation of the PMNS matrix is $U \xrightarrow{CP} U^*$ while all the other terms are invariant under CP transformations, thus:

$$\begin{aligned} \mathscr{P}_{\bar{\alpha}\to\bar{\beta}}(E,L) &= \mathscr{P}_{\alpha\to\beta}(E,L;U\to U^*) && (1.36)\\ &= \delta_{\alpha\beta} - 4\sum_{j<k} \mathfrak{Re}\left[U_{\alpha j}U^*_{\beta j}U^*_{\alpha k}U_{\beta k}\right]\sin^2\left(\frac{\Delta m^2_{jk}\,L}{4E}\right) \\ &\quad -2\sum_{j<k} \mathfrak{Im}\left[U_{\alpha j}U^*_{\beta j}U^*_{\alpha k}U_{\beta k}\right]\sin\left(\frac{\Delta m^2_{jk}\,L}{2E}\right) && (1.37)\end{aligned}$$

Previous results were obtained in natural units. Restoring the proper IS units, the arguments of each sine have to be multiplied by the factor $\frac{c^3}{\hbar} = 5.068$ GeV km^{-1} (eV/c^2)$^{-2}$.

Despite the fact that this plane-wave derivation is useful and quite established, it is not totally consistent. Energy-momentum conservation is a bound for the energies and momentum of neutrinos, since all the neutrinos are coming from the decaying process of a particle with a definite mass. Thus, energy-momentum conservation is actually preventing to state that the energy of a flavour defined state is equal to the energy its decomposition in mass defined states, as implicitly assumed in equation 1.31. In order to overcome this problem, it is necessary to treat neutrinos and the other particles participating in the production and detection processes as wave packets [8, Section 8.2]. However, in practical applications, the wave-packet treatment can be avoided because the oscillation probability obtained with the wave-packet treatment cannot be distinguished from the plane-wave oscillation probability once the latter has been averaged over a Gaussian $\frac{L}{E}$ distribution which corresponds to a detector resolution response.

1.2.2 Matter effect

Once neutrinos are in matter, the free Hamiltonian has to be changed since the neutrinos are subject to the potential due to NC and CC coherent interactions. The NC interactions with the electrons are the same for each flavour, but electron neutrinos (and electron anti-neutrinos) have an additional contribution due to W exchange, see Figure 1.2. The effective potential [8, Section 9.1] is

$$\begin{aligned} V_{CC} &= \sqrt{2}\,G_F N_e \quad \text{for electron neutrinos} && (1.38)\\ \overline{V}_{CC} &= -\sqrt{2}\,G_F N_e \quad \text{for electron anti-neutrinos} && (1.39)\end{aligned}$$

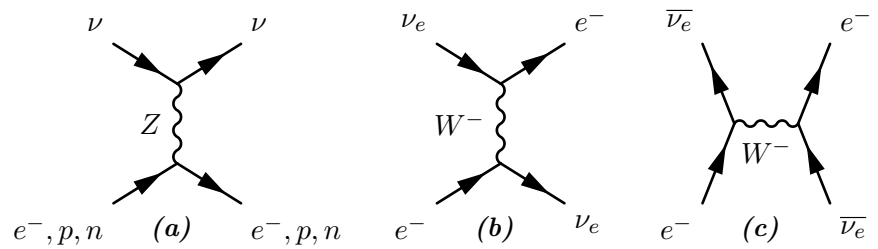

Figure 1.2: *Feynman diagrams for coherent interactions between neutrinos and electrons in matter. Diagram (a) is the NC interaction between all neutrino flavours with electrons, protons and neutrons. The same diagram can be applied also for $\overline{\nu}$. (b) is the CC interaction contribution specific for electron neutrinos and (c) is the CC component for the anti-neutrino interactions.*

where G_F is the Fermi constant and N_e is the electron density of the medium. This effect was firstly noticed by Mikheyev, Smirnov and Wolfenstein [14, 15] that's why it is also known as the MSW effect.

Due to this term, the mass eigenstates are no more eigenvector of the Hamiltonian which can be written as

$$\mathscr{H}\begin{pmatrix}|\nu_1\rangle\\|\nu_2\rangle\\|\nu_3\rangle\end{pmatrix} = \left[U^T\begin{pmatrix}V_{CC}&0&0\\0&0&0\\0&0&0\end{pmatrix}U^* + \frac{1}{2E}\begin{pmatrix}m_1^2&0&0\\0&m_2^2&0\\0&0&m_3^2\end{pmatrix}\right]\begin{pmatrix}|\nu_1\rangle\\|\nu_2\rangle\\|\nu_3\rangle\end{pmatrix} \tag{1.40}$$

Note that the Hamiltonian terms proportional to the identity matrix have been omitted.

There are no general solutions to this problem, since N_e can depend on the space coordinates as well. This process is very important in transitions lead by electron neutrinos in dense media such as solar neutrinos oscillations or neutrinos from supernovae, while it is not leading in other situations, like ν_μ oscillation experiments.

1.2.3 Open questions about Neutrino Oscillations

Despite the fact that oscillations were discovered less than 20 years ago, the lepton mixing sector is rather well known. For instance, all the mixing angles have been measured together with all the modules of the squared mass differences. Anyway there are two experimental major issues about the oscillation parameters.

The first is the value of the δ_{CP} phase, which is unknown due to the fact that no experiment is yet sensitive to this parameter. Also, this was not considered an important topic since the requirement for being able to measure this value is that all the three mixing angles are different from zero. This was lately observed only in 2012 by the Daya Bay experiment [16].

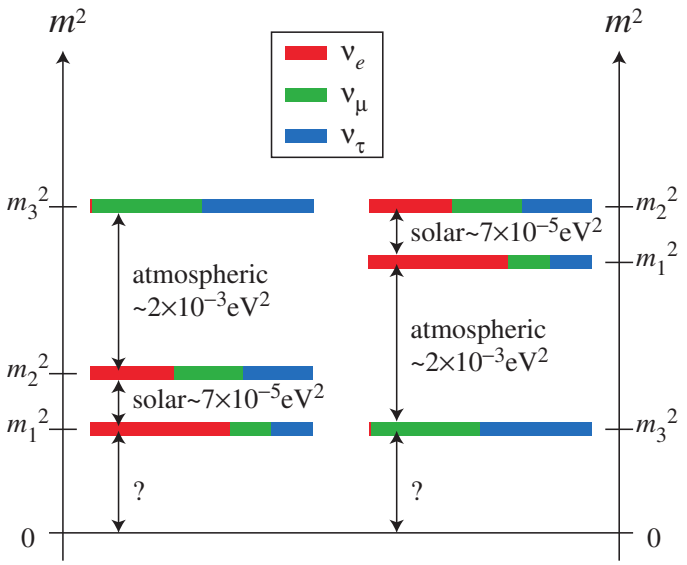

Figure 1.3: *Neutrino masses spectra obtained from neutrino oscillation experiments [18]. The left plot represents the so called normal hierarchy, while the right plot is the inverted hierarchy.*

The second open question is the hierarchy. In principle, the oscillation probability depends also on the sign of the squared masses differences. Anyway, this dependence is very small and beyond the actual experimental sensitivity. Thus, from the experimental point of view, only the modules of the squared mass differences are know with a satisfactory statistical significance: this is the so called hierarchy problem. This problem was solved for the two eigenstates separated by the smallest Δm^2, the so called Δm^2_{21}, which is known to be positive. The sign was determined using the different matter effects between neutrino and anti-neutrino [17]. The case of the larger squared mass difference is yet to be solved and the present understanding of neutrino mass models is summarized in Figure 1.3.

1.3 Neutrino experiments

Neutrino experiments cover a wide range of energies and they use different physics processes in order to measure the parameters of the SM lepton sector, namely the three neutrino masses and the parameters of the PMNS matrix.

From the experimental point of view, the mixing parameters can be extracted from the measurement of the oscillation probabilities as a function of the incoming neutrino energy. Of course, no experiment can measure at the same time all the possible flavour combinations of oscillation patterns, due to both physical and technological reasons. In order to measure the oscillation probabilities, a typical neutrino oscillation experiment has the

detectors placed in two different sites: near and far, with respect to the neutrinos source. The comparison between the spectra extracted from the different sites leads to the neutrino oscillation probabilities.

Oscillation experiments can be classified in two main categories depending on the oscillation pattern they look for: appearance and disappearance experiments.

Disappearance experiments are used to determine the survival probability of one neutrino flavour, namely $\mathscr{P}(\alpha \to \alpha, E)$. In these experiments the near detector is extremely important because it allows to control the generally large experimental uncertainties on the neutrino fluxes. Usually, these experiments benefit of large statistics. Unfortunately these experiments are completely insensitive to the CP phase of the lepton sector. In fact, in disappearance mode, the mixing factor of equation 1.35 can be reduced:

$$U_{\alpha j}U^*_{\beta j}U^*_{\alpha k}U_{\beta k} \xrightarrow{\beta=\alpha} U_{\alpha j}U^*_{\alpha j}U^*_{\alpha k}U_{\alpha k} = |U_{\alpha j}|^2 |U_{\alpha k}|^2 \tag{1.41}$$

which has no imaginary part.

Disappearance experiments aim to measure transitions between different neutrino flavours. If the final flavour to be searched for is not present in the initial beam, backgrounds can be very small and a proper near detector is not really mandatory. In this particular case, an experiment can be sensitive to rather small values of the mixing angle.

1.3.1 Reactor neutrino experiments

This type of experiments were the first used to discover neutrinos. In such a kind of set-up, the neutrino sources are nuclear power plants cores. Inside a core, the fissile fuel undergoes a fission process generally like

$$^{235}_{92}U + n \longrightarrow X_1 + X_2 + 2n \tag{1.42}$$

where X_1 and X_2 are two nuclei with atomic number about 90 and 140, respectively. In the final state the total number of protons is bigger than in the initial state: for each new proton an anti-neutrino is produced through a β-decay.

The anti-neutrinos are detected through the inverse β-decay $\overline{\nu}_e + p \to n + e^+$ in a liquid scintillator. The neutron in the final state is used as a trigger since it produces a photon of 2.2 MeV when it is captured by a proton, with a delay of about 180 μs. In presence of a small fraction of Gadolinium, the neutron free path can be reduced by an order of magnitude and the final trigger photon energy is 8 MeV.

The neutrino spectrum depends on the fuel isotopes and it usually ranges up to 10 MeV. The observed neutrino energy spectrum has a peak between 3

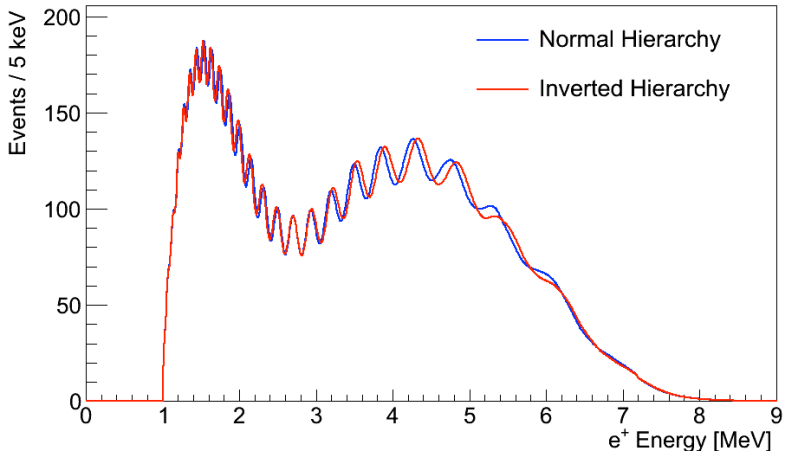

Figure 1.4: *Expected positron spectrum at the JUNO experiment [22]. The solar oscillation (Δm^2_{21}) causes the broad deficit between 2 and 4 MeV. The normal (blue) versus inverted (red) hierarchy results in an effective shift in the phase of the high-frequency oscillation. In this example, Δm^2_{31} has been changed to $-\Delta m^2_{31}$ in inverting the hierarchy.*

and 4 MeV, while the detectable lower edge is 1.8 MeV, which is the threshold for the CC $\overline{\nu}_e$ interaction. Due to such low energies there is no chance to produce muons or taus, therefore the only oscillation experiments which can be performed using reactors are disappearance experiments.

Despite the disappearance limitation, reactor experiments were able to contribute to the determination of θ_{12} with KamLAND results [19] while Daya Bay recently claimed the first measurement of θ_{13} [20].

The next generation of reactor neutrino experiments is expected to approach the hierarchy problem looking at the interference term between Δm^2_{21} and Δm^2_{31}. To do so, experiments like JUNO[4] [21] will be far more massive than present reactor experiments (20 kt) in order to achieve the statistical sensitivity needed to measure this tiny effect. These experiments will require an extreme energy resolution in order to distinguish between the normal and the inverted hierarchy spectra, see Figure 1.4.

1.3.2 Solar neutrino experiments

By definition, solar neutrinos are produced in the fusion reactions inside the Sun core. The Sun produces electron neutrinos with two different processes: the pp chain and the CNO cycle. Each process is composed of several different reactions and some of them have a neutrino in the final state. The total solar

[4] Jiangmen Underground Neutrino Observatory

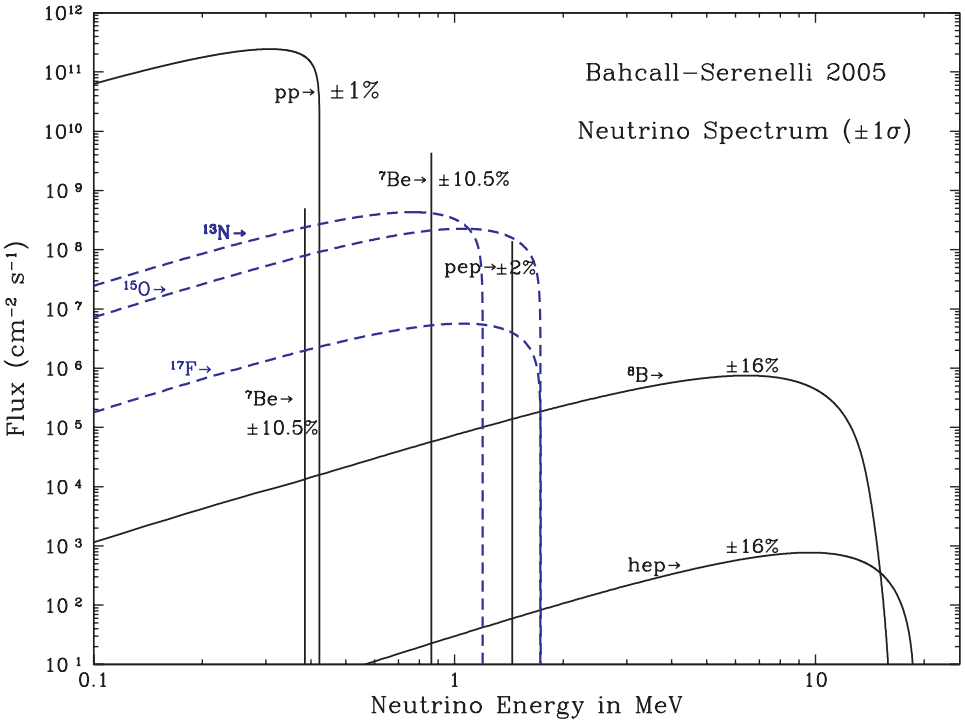

Figure 1.5: *Solar neutrino fluxes according to the Standard Solar Model [23]. Continue lines are the neutrino coming from the pp-chain while the dotted ones are the spectra from the CNO cycle. The three vertical lines correspond to processes with a final two body state and therefore the emitted neutrino is almost monochromatic.*

neutrino spectrum can reach almost 20 MeV, according to the standard solar model, see Figure 1.5.

In the 70's, the first dedicated experiments were using inverse β^+ decay on chloride or gallium nuclei in order to detect solar neutrinos. They all detected a deficit with respect to what predicted by the standard solar model, but at that time it was thought the problem was in the solar model [24]. This deficit was also confirmed by the KAMIOKANDE experiment [25], a water Cherenkov detector, which also provided neutrino direction information using the electron elastic scattering reaction $\nu_e + e^- \to \nu_e + e^-$.

The puzzle was solved by the SNO experiment [26] which was a water Cherenkov detector where normal water was replaced by heavy water. SNO was able to detect three different types of neutrino interactions:

CC interactions through the reaction $\nu_e + d \to e^- + p + p$;

NC interactions through deuterium dissociation $\nu + d \to \nu + n + p$, which is reconstructed using neutron capture by deuterium, producing tritium and a photon of about 6 MeV;

Elastic Scattering of neutrino on electron through the reaction $\nu + e^- \rightarrow \nu + e^-$, where the scattering amplitude depends on the incoming neutrino flavour.

These three reactions combined together were able to identify a single region of the $(\Delta m^2_{21}, \theta_{12})$ parameters space [27].

Nowadays, the challenge is the detection of the low energy components of solar neutrino spectrum. To achieve such a result it is important to build high purity detectors in order to reduce backgrounds. So far, the best results was obtained by the Borexino experiment [28] which is a liquid scintillator experiment designed to look for neutrino elastic scattering on electrons. Recently, this experiment published the first observation of neutrinos coming from the pp chain [29].

1.3.3 Neutrino beam experiments

Neutrino beam experiments studies neutrinos coming from pion or kaon decay. The mesons are produced from a primary proton beam which hits a target. Before their decay, these charged particles are collected and focused by magnetic lenses and let decay in a vacuum pipe so that an actual neutrino beam is produced. Due to mesons branching ratios, the beams are mostly composed of muon neutrinos or anti-neutrinos, depending on the meson charge selection: positive for neutrinos and negative for anti-neutrinos. Still, contaminations of electron neutrinos and anti-neutrinos remain at the percent level.

The energy spectrum of a neutrino beam depends on the energy of the primary proton beam and on the magnetic lenses position with respect to the target. In general, the neutrino energy is between few hundred MeV to few hundred GeV. The energy distribution is usually broad and one or more peaks can be present in the spectrum. Thanks to this energy range, on a neutrino beam both disappearance and appearance experiments can be performed. Note that the possibility to carry on appearance experiments means having the possibility to measure the CP phase of the lepton sector, although this is not trivial.

The detectors used in this kind of beam are extremely different and depend on the type of measurement which has to be performed. In general, detectors have the capability to distinguish electrons, muons and hadrons and they are often able to perform momentum measurements, at least for muons.

These experiments were firstly designed to confirm the atmospheric neutrino oscillation in a more controlled environment. Atmospheric neutrinos are coming from mesons decay produced in cosmic rays interaction with the atoms of the high atmosphere. At tens of GeV energies, these neutrinos could benefit of very long baselines, about the Earth diameter, providing a very

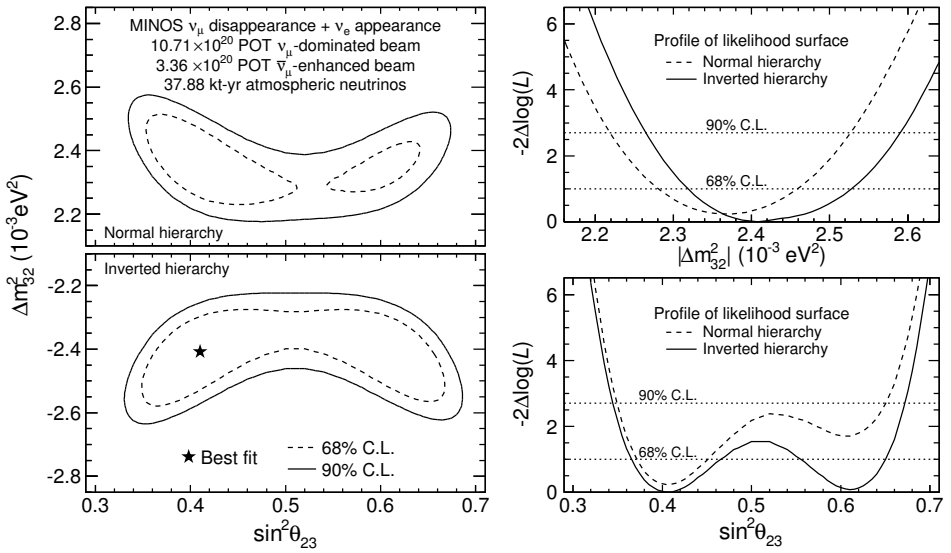

Figure 1.6: *Minos results. The left panels show the* 68% *and* 90% *confidence limits (C.L.) on* Δm^2_{32} *and* $\sin^2\theta_{23}$ *for the normal hierarchy (top) and inverted hierarchy (bottom). At each point in this parameter space, the likelihood function is maximized with respect to* $\sin^2\theta_{23}$, δ_{CP} *and all of the systematic parameters. The* $-2\Delta\log(L)$ *surface is calculated relative to the overall best fit, which is indicated by the star. The right panels show the* $1D$ *likelihood profiles as a function of* Δm^2_{32} *and* $\sin^2\theta_{23}$ *for each hierarchy. The horizontal dotted lines indicate the* 68% *and* 90% *C.L.*

strong oscillation signal. This disappearance signal can be observed looking at the ratio between muon neutrinos coming from the top and the bottom of the detector, corresponding to short and long baselines, respectively. This was done in experiments like SuperKamiokande [30] or MACRO [31].

Beam disappearance experiments managed to obtain the best measurements of the mixing parameters responsible for the atmospheric neutrino oscillation but they were not able to solve the hierarchy problem. The present best results have been reported by the MINOS experiment [32]; the contour plots for $\sin^2\theta_{23}$ and Δm^2_{32} are presented in Figure 1.6.

Future experiments aim to measure hierarchy and CP phase. To do so, very long baseline experiments are required while the detection technology will be based on liquid argon detectors in order to achieve an accurate topological reconstruction.

1.3.4 Neutrino mass experiments

Information about neutrino masses can be obtained from oscillation experiments, though only squared mass differences can be retrieved i.e. no absolute

information can come from this kind of experiments.

Fro what concerns absolute mass values, the current experiments are all dedicated to the precise measurement of the β decay spectrum endpoint from different nuclei, the best nucleus being the tritium. In this scenario, the most promising set-up is the KATRIN experiment [33]. So far, no experiments have been able to determine a mass value and only upper limits have been reported. These limits are given on the effective electron neutrino mass and the best limit available is [34]

$$m_{\nu_e} \equiv \sqrt{\sum_i |U_{ei}|^2 m_i^2} < 2\,\text{eV} \tag{1.43}$$

Neutrinoless double β decay experiments are also able to put limits on the neutrino masses. In fact, the observation of this process depends on the $m_{\beta\beta}$ mass:

$$m_{\beta\beta} \equiv \left| \sum_j m_j |U_{ej}|^2 e^{i\alpha_j} \right| \tag{1.44}$$

anyway, no evidence for such a process has been obtained. Thus, only upper limits are available, which unfortunately strongly depend on the nuclear matrix elements which are extremely difficult to evaluate.

Cosmology is also able to constraint neutrinos masses since massive neutrinos affect the cosmic microwave background and the large scale structure of the universe [35]. Cosmology structures are sensitive to the total sum of neutrino masses, namely

$$\Sigma \equiv \sum_{i=1}^{3} m_i \tag{1.45}$$

but all of these results are extremely model dependent.

1.3.5 Other experiments

Neutrino experiments are not only related to oscillation studies. Of course, there are other experiments dedicated to the observation of other neutrino sources.

Recent interesting results were presented by neutrino telescopes dedicated to the detection of very high energies neutrinos coming from outer space. The most famous is probably IceCube [36] which is an ice Cherenkov detector located at the South Pole. Having instrumented a cubic kilometre of ice, it can measure neutrino energies up to the PeV region, exploring the extremely high energy region of cosmic neutrinos.

1.3.6 Light Sterile Neutrinos

Neutrino oscillation experiments apparently support the possibility of the presence of light sterile neutrinos. The experimental hints are coming from three different signatures.

Electron anti-neutrino anomaly from reactor experiments. These experiments reported deficits with a statistical significance of about 3σ around 4 MeV and baselines within the 10 to 100 meters range [37].

Gallium anomaly form calibration source. Gallium experiments look for electron neutrino disappearance and they often use strong β^+ sources for calibration. These experiments claimed a deficit of electron neutrinos coming from these sources at energies around 1 MeV and baselines of about 1 m [38].

LSND anomaly from short baseline oscillation experiments. The experiment LSND[5] exposed to a muon anti-neutrino beam reported an excess of electron anti-neutrino with a significance of about 4σ. This happens at energies of about 50 MeV and a baseline around 30 m [39].

These anomalies can be interpreted as a new oscillation phenomenon. If so, the fitted parameters lead to the presence of a light sterile neutrino with mass around 1 eV. Anyway, these global fits show some tensions which do not allow to reach any strong conclusion. So far, no experiment has been conclusive in solving this issue.

1.4 Heavy particles in neutrino experiments

Heavy particles such as tau or charm, even bottom, could be produced in neutrino interactions, according to the incoming neutrino energy and flavour. Their study is very interesting, also for quark physics, and to the one performed in collider experiments.

1.4.1 Tau neutrino measurements

The experiments described in section 1.3 were not related to tau neutrinos detection. As a matter of fact, it is indeed a difficult task: to identify a tau neutrino means being able to detect a tau particle, which has a lifetime of $(290.3 \pm 0.5) \times 10^{-15}$ s. This can be done only with a tracker detector with a spatial resolution at the micrometer level. This resolution has to be available in the large volumes typical of neutrino experiments, with masses in the kilotons range.

[5]Liquid Scintillator Neutrino Detector

The tau neutrino was observed for the first time by DONuT[6] experiment at the Tevatron [40], using a dedicated beam obtained from the decay of D_s^+ mesons. These mesons decay in τ^+ and ν_τ with a branching ratio of about 5%. The core detector was made of *Emulsion Cloud Chambers*: these were an assembly of elementary mechanical units, made of nuclear emulsion sheets interleaved with iron layers. The final sample of tau neutrino interactions was made of 9 candidates.

The first attempt to measure tau neutrino oscillation was made by CHORUS[7] experiment [41, 42]. The goal was the detection of tau neutrinos appearance from a muon neutrino beam with a short baseline, about 850 m. The experiment was sensitive to high mass differences, $\Delta m^2 \gtrsim 10$ eV^2, due to its short baseline. Therefore CHORUS was not able to observe tau neutrinos.

Nowadays, from disappearance experiments, it is known that, in order to observe such a process, very long baselines are required since the transition happens at $\Delta m^2 \sim 2.4 \times 10^{-3}$ eV^2. That's why a long baseline experiment, like OPERA, is necessary.

Despite the fact that nuclear emulsion experiments are the most obvious choice for ν_τ studies, they are not the only possibility. In fact, a ν_τ CC interaction looks almost like a NC interaction in usual muon detectors, therefore tau neutrinos can be detected as an excess of NC interactions. This was done by Super-Kamiokande using atmospheric neutrinos, excluding the no-tau-appearance hypothesis at the $3.8\,\sigma$ level [43].

1.4.2 Charm searches in neutrino experiments

High energy neutrino interactions produce charmed hadrons at the level of a few percent and therefore they represent a tool to study charm physics. Charmed hadron production was studied basically in two ways: dilepton studies with both calorimeter and bubble chamber techniques, and nuclear emulsion experiments with the visual observation of charmed hadron decays.

So far only two experiments, E531[44] and CHORUS[41], searched for inclusive charm-production through the direct identification of charm decays in emulsions. The main advantage of these experiments is that, being the charmed particle clearly identified through its decay, very loose kinematic cuts are applied. Even with a loose selection, for these experiments the background is very low. It is made of pions and kaons decays in flight or hadron interactions without any visible nuclear break-up. The background contribution of these processes is of the order of 10^{-4} per CC interaction.

The above experiments had a hybrid design. Emulsions were used as active targets having the appropriate position resolution (less than 1 μm) and granularity to detect short-lived particles through the visual observation of their decays. Electronic detectors predicted the emulsion region where the

[6] Direct Observation of Nu Tau

[7] CERN Hybrid Oscillation Research apparatUS

neutrino interaction occurred and contributed to the reconstruction of the event kinematics.

Using emulsions, studies of inclusive charm production in neutrino interactions were done, including Λ_c^+, D^{*+}, quasi-elastic charm production and J/Ψ. CHORUS was also able to identify a spectacular event of diffractive D_s^+ production, reported in Figure 1.7.

Such events selections allowed very interesting charm properties measurements like charm production fractions, semi-muonic branching ratios as well as other variables describing charm hadronization, e.g. m_c. These data were also interesting for the measurements of CKM matrix elements, in particular V_{cd} and V_{cs}. Also, charm production in neutrino interactions is a powerful tool to investigate the strange quark content of the nucleon. Indeed, given also the CKM couplings, about 50 % of the charmed hadrons in neutrino interactions come from strange to charm transition. In anti-neutrino interactions this fraction is even larger, about 90 %, given also the need for anti-quarks, hence sea quarks, in the transition.

A complete review of charm measurements in neutrino interactions can be found in [46, 47].

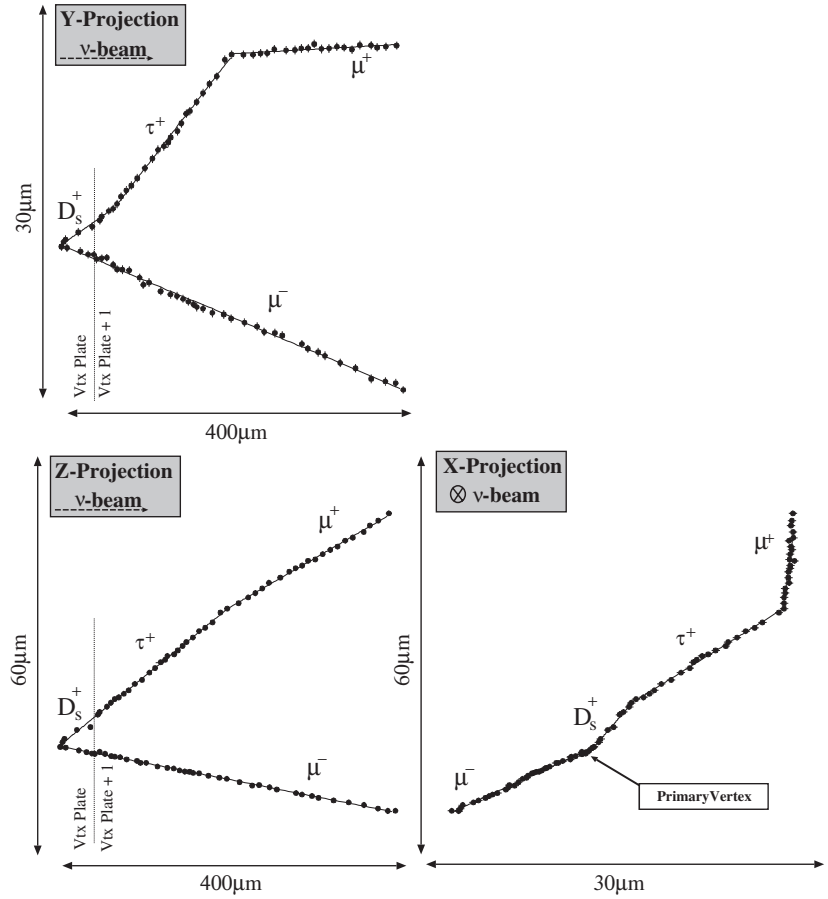

Figure 1.7: *Double-kink event, observed in the CHORUS experiment, with two tracks leaving from a single grain without nuclear beak-up at the primary vertex [45]. The points are the measured position of each emulsion grain with its error. Also indicated is the borderline between two consecutive plates. The event's most probable interpretation is a ν_μ CC interaction with D_s^+ production. The D_s^+ meson is identified through its decay into a τ^+ which then decays into a μ^+.*

Chapter 2

The OPERA experiment

OPERA[1] [48] is a long baseline neutrino oscillation experiment. It was designed for the direct observation of ν_τ appearance in the CNGS[2] ν_μ beam produced at CERN. The mechanism for ν_τ production is the $\nu_\mu \rightarrow \nu_\tau$ oscillation process.

The detector is located at the Gran Sasso Laboratory (LNGS), Italy. It is based on a massive lead/nuclear emulsion target. It aims to detect tau produced in ν_τ CC interactions, which are directly observed through their decay. Electronic detectors locate the emulsion containing the event. Magnetized iron spectrometers measure charge and momentum of muons.

The discovery potential of OPERA originates from the observation of a ν_τ signal with very low background level. Recently OPERA claimed the discovery of the ν_τ appearance, having detected 5 events over a background of 0.25 events. This corresponds to a significance of $5\,\sigma$ [49].

2.1 CNGS

The CNGS neutrino beam is generated by a 400 GeV proton beam extracted from the SPS accelerator impinging into a carbon target producing kaons and pions, see Figure 2.1. The positively charged particles are focused and pointed to the Gran Sasso direction by two magnetic lenses: the *Horn* and the *Reflector*. Pions and kaons decay to ν_μ and μ^+ in a 1000 m long vacuum pipe. At the end of the decay pipe there is an hadron stop which absorbs all not decayed hadrons. Muons are monitored by two μ detector stations. This allows intensity and profile measurement of the neutrino beam. At the end of the decay line muons are absorbed in the rock.

The resulting neutrino beam is a high energy ν_μ beam ($\langle E_\nu \rangle \sim 20$ GeV [50]) optimized to maximize the number of detectable ν_τ CC interaction at the LNGS site, see Figure 2.2. The beam contains small contaminations of

[1] Oscillation Project with Emulsion-tRacking Apparatus
[2] CERN Neutrino beam to Gran Sasso

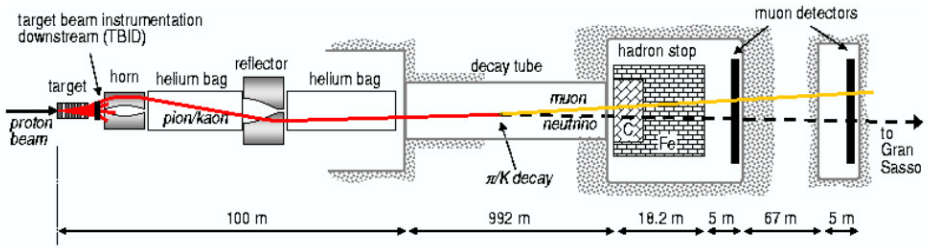

Figure 2.1: *Scheme of the CNGS beam production.*

$\overline{\nu}_\mu$ and electron neutrinos while the number of prompt ν_τ is negligible. In particular, the expected $\overline{\nu}_\mu$ interactions are 2.1% of the total, while the ν_e and $\overline{\nu}_e$ contaminations are lower than 1% [50]. The expected spectra of the CNGS beam can be seen in Figure 2.3. With the design luminosity, OPERA expected about 5000 ν_μ interactions per year and 20 ν_τ CC events per year produced in the detector.

The standard OPERA high intensity beam has a time structure composed of two 10.5 μs wide proton extractions with an almost flat intensity distribution. This is constantly measured in order to check the expected luminosity of the experiment. The time information of the proton extraction is saved and it is used to select only events on-time with the CNGS beam, in order to reduce backgrounds.

2.2 OPERA detector

OPERA has a modular detector [51] made of two identical Super Modules (SMs), see Figure 2.4. Every SM is composed of a target section and a muon spectrometer. Target sections are the volumes containing the emulsions dedicated to ν_τ searches. The spectrometers are mostly designed to identify muons coming from the ν_μ CC interactions. Before the first SM two layers of glass RPC are used to tag events occurring upstream of the OPERA Detector.

The total length of the detector is about 20 m and the transverse dimensions are about 10 m $\times$ 10 m. The OPERA reference frame has the z axis parallel to the longest dimension of the detector, oriented along the beam direction. The y axis is the vertical axis, pointing to the vault of the gallery. The x axis is parallel to the floor such that $\hat{x} \times \hat{y} = \hat{z}$.

2.2.1 Target

The basic unit of the Target is the *brick*, which contains the nuclear emulsions. The total number of bricks inside the detector is about 150 thousands. The target is made of *walls*, each of them contains about 2920 bricks. Each wall

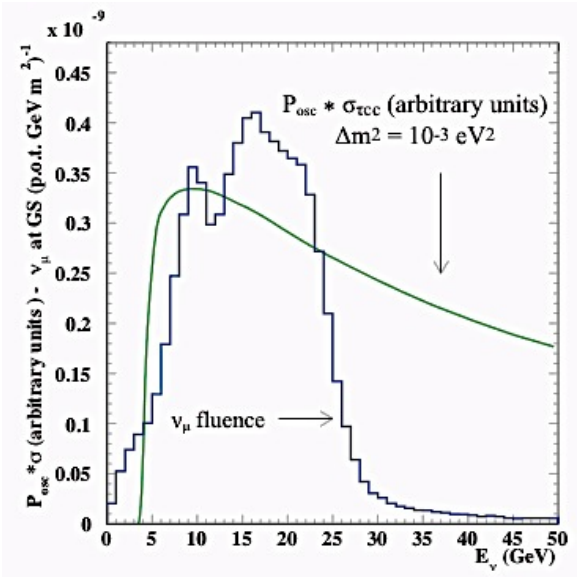

Figure 2.2: *Muon neutrino energy spectrum (blue histogram) compared to the tau appearance probability (green curve). In particular the curve is the $\nu_\mu \to \nu_\tau$ oscillation probability multiplied by the ν_τ CC cross section.*

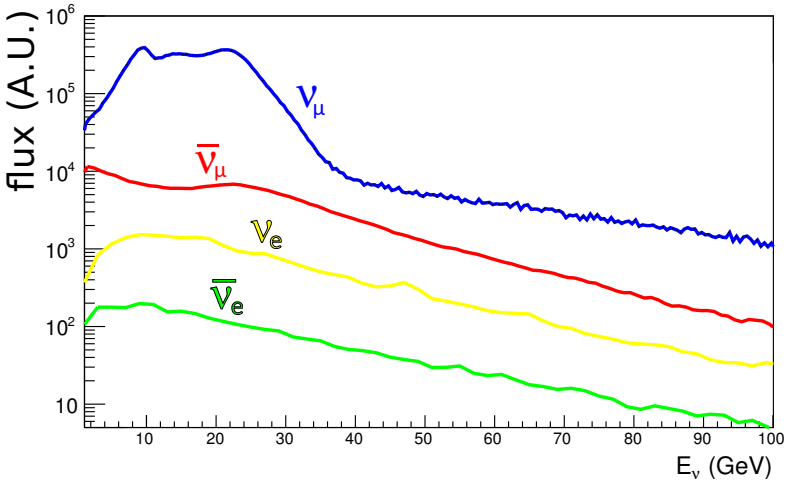

Figure 2.3: *Energy distribution of each flavour component of the CNGS beam [50].*

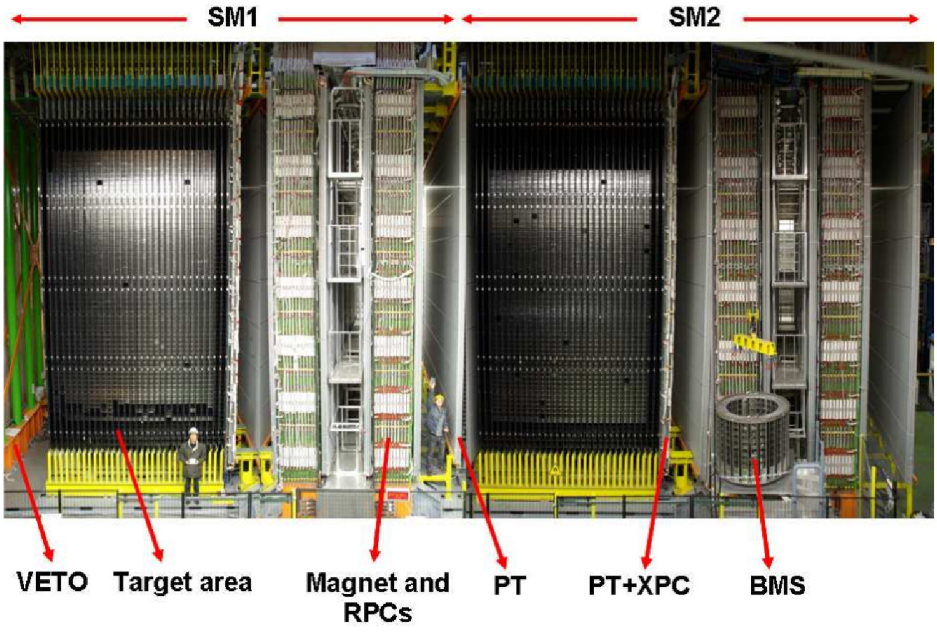

Figure 2.4: *Side view of the OPERA detector. The neutrino beam goes from the left to the right.*

is made of ultra-light stainless-steel structures, in order to support the weight of the bricks.

Walls are separated by a pair of orthogonal scintillator strip arrays, so called Target Trackers (TT). TT primary goal is the localization of the brick containing the neutrino interaction. The strips have an effective granularity of $2.6\,\text{cm} \times 2.6\,\text{cm}$ and a surface of $6.7\,\text{m} \times 6.7\,\text{m}$ transverse to the beam direction. Scintillator strips are designed with an embedded wavelength-shifting (WLS) fibre in the centre of the strip, see Figure 2.5. The fibers are readout at both ends by multi-anode photomultiplier tubes [52], Figure 2.6a. This system can provide x and y position of a charged particle crossing the wall.

The total masses of the lead-emulsion bricks and scintillator strips are about 1.25 and 0.08 kton, respectively.

2.2.2 Spectrometers

The muon spectrometers at the end of each SM are used to identify muons and to measure their momentum and charge. The transverse size of the magnets are 8.75 m and 8 m in the horizontal and vertical directions, respectively. This provides an adequate geometrical acceptance also for muons originating in the upstream target volume. Each arm is made of 12 iron plates 5 cm thick. The iron is magnetized by a current of about 1200 A circulating in the top and bottom copper coils. The measured magnetic field strength is about 1.52 T.

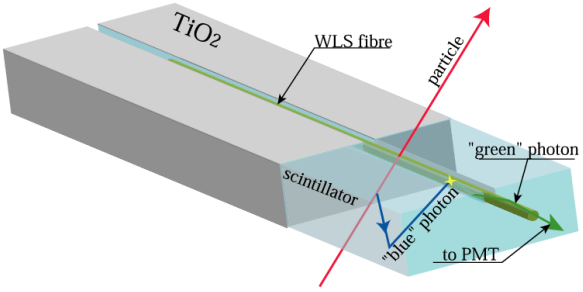

Figure 2.5: *Target Tracker scintillator strips design.*

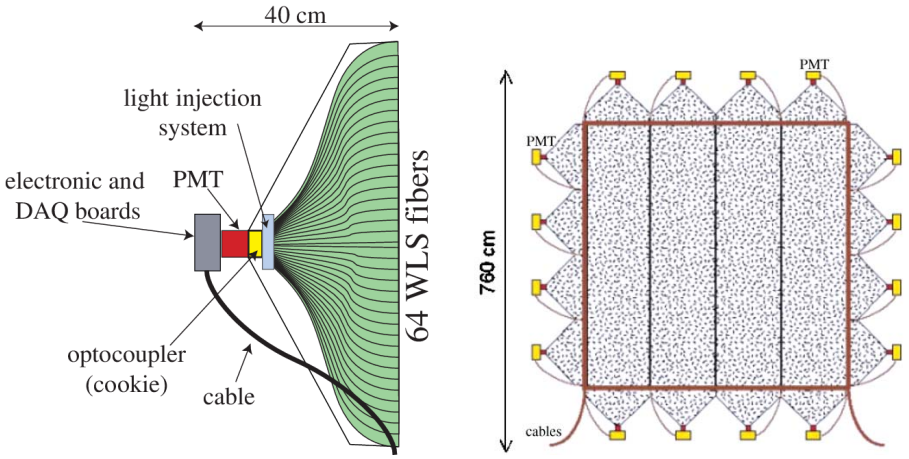

(a) *Fibers to PMT connection* ***(b)*** *Wall instrumentation*

Figure 2.6: *Target tracker electronic schemes [52]. (a) shows the WLS fibers to PMT connection, each PTM collect 64 fibers. (b) is the scheme of the electronics instrumentation of a target wallpaper.*

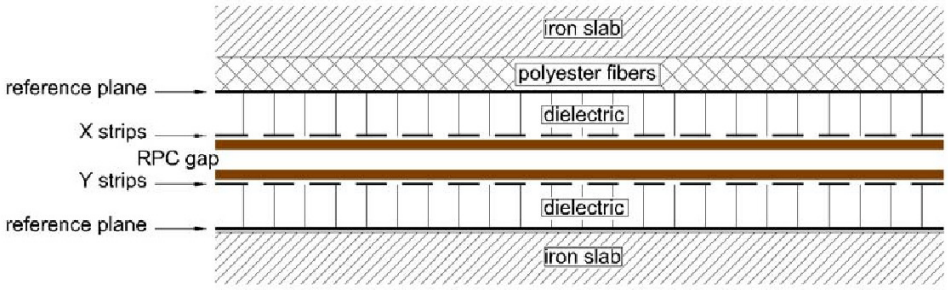

Figure 2.7: *Section of a magnet gap with RPC and pickup strips.*

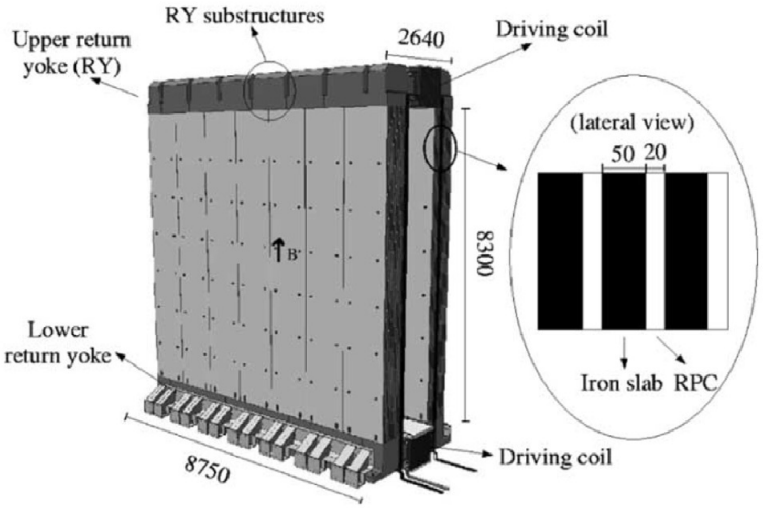

Figure 2.8: *Details of the OPERA magnets. Quotes are expressed in millimeters.*

The vertical field lines have opposite directions in the two magnet walls. The gaps between the iron plates are instrumented with Bakelite RPC[3] planes, whose size is 8.7 m × 7.9 m, transverse to the beam direction. The scheme of the OPERA RPC can be seen in Figure 2.7. On each face of the RPC planes, the induced pulses are collected by 3 cm wide readout copper strips in the horizontal direction and by 2.6 cm wide ones in the vertical direction. These detectors provides a coarse tracking inside the magnet, allowing muon identification. RPCs can also be useful to measure the tail of the hadronic energy leaking from the target. The scheme of the magnets can be seen in Figure 2.8.

The two spectrometers arms are interleaved with six vertical drift-tube

[3]Resistive Plate Chamber

stations, the Precision Trackers (PTs), for a precise measurement of the bending of the muon tracks. The intrinsic resolution of the PTs is 0.3 mm in the bending direction. The two tracker planes located upstream and downstream each magnet arms provide an angular measurement of the track with a 100 cm lever arm. This design leads to a muon momentum resolution better than 30% for momenta up to 25 GeV.

RPC with the readout strips tilted by $\pm 42.6^\circ$ with respect to the horizontal, called XPC, are combined with the PT to provide unambiguous track reconstruction in space.

2.3 OPERA nuclear emulsions

The OPERA emulsion/lead assembly is called Emulsion Cloud Chamber (ECC). ECC allows high spatial resolution over a large scale detector, which is the requirement for tau identification. The single unit which acts like a standalone detector is the *brick* [53].

2.3.1 Nuclear emulsion

Nuclear emulsions consist of silver bromide (AgBr) crystals dispersed in a gelatin bender. The size of the grains is about 0.2 μm. The energy released by a charge particle transit frees silver atoms creating metallic silver on the surface of a bromide crystal: this is the so called latent image, which is made of a few silver atoms on crystals made of billions of atoms. Photographic developer is a chemical amplifier acting on the latent image, with a gain factor up to several billion. The final silver grains have diameters of about 0.6 μm, thus they become visible with an optical microscope. However, in order to act as an effective latent image center, at least four silver atoms are necessary.

The OPERA design needs a very large amount of emulsion, more than 10^5 m^2, which is more than any previous experiment based on nuclear emulsion. This required a dedicated industrial production and an R&D program in collaboration with Fuji Film Company.

2.3.2 OPERA emulsion layer

An OPERA film has two emulsion layers (each about 50 μm thick) on both sides of a transparent cellulose tri-acetate base (about 200 μm thick); the total thickness is 293 ± 5 μm. The intrinsic position resolution of the gelatin treated with the normal OPERA developer is about 50 nm, which corresponds to a 0.25 mrad intrinsic angular resolution. The density of the emulsion gel is 2.7 g/cm^3 and its radiation length X_0 is 5.0 cm. The sensitivity of OPERA emulsion films is measured to be about 28 grains/(100 μm) for Minimum Ionizing Particles (MIPs).

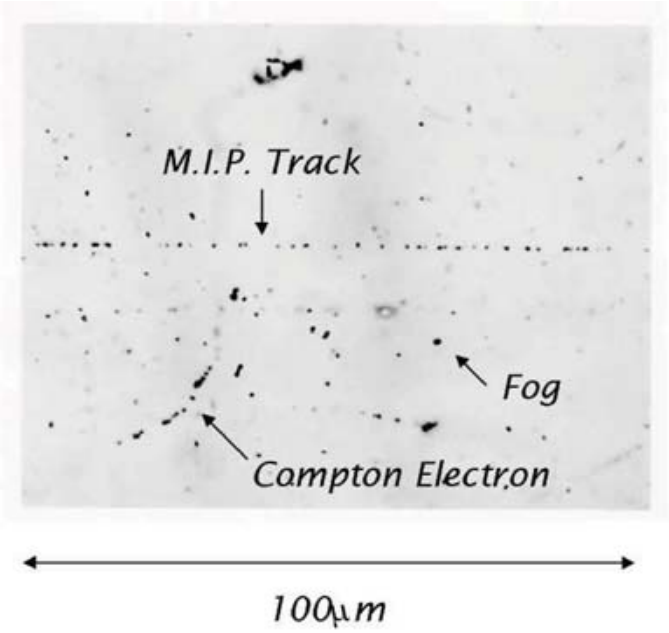

Figure 2.9: *Examples of signal tracks (MIP) and background (Compton electron and fog) formation in nuclear emulsions.*

Nuclear emulsions integrate all tracks from their production to their development, including cosmic rays and environmental radiations. During the production process at the Fuji Film industrial plant in Japan, each films integrates about 3000 tracks/cm^2, a value much larger than the maximum density allowed for an unambiguous interaction reconstruction, which is about 100 tracks/cm^2. In order to reduce this background, a new procedure called refreshing was set up. It consists in keeping the emulsion films at high relative humidity (RH) and high temperature. To process the about ten millions films needed for the experiment, a refresh facility was constructed in Tono mine in Gifu, Japan. The facility operates at 27 °C with a cycle lasting five days: one day of open air humidification (90% RH), three days of closed air humidification (98% RH) and one day of dry mode (40% RH). This process reduces the integrated number of tracks from about 3000 to less than 100 tracks/cm^2, without affecting the emulsion sensitivity to tracks detected later on.

The randomly distributed grains (fog) induced by thermal excitation constitute a background for track reconstruction. The fog density is slightly increased by refreshing: measurements show a fog density of 3 and 6 grains per 1000 μm^3 of emulsion before and after the refreshing, respectively. Example of fog compared to MIP in emulsion can be seen in Figure 2.9.

The films treated in Tono mine were then transported to Italy by boat; during the travel, the films were placed vertically to minimize the integrated

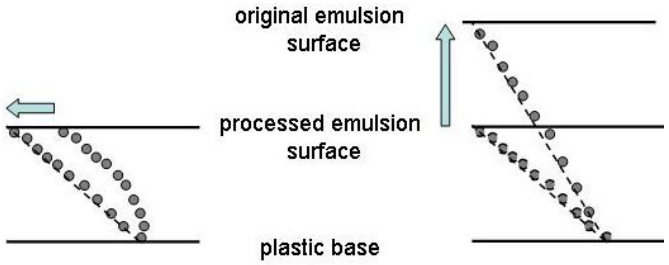

Figure 2.10: *Track distortion (left) and shrinkage (right) corrections.*

cosmic ray flux. Nevertheless, a cosmic ray density of about 1000 tracks/cm^2 was accumulated. To suppress this background, the films were vacuum packed without any spacer before the shipment. Each pack is used for one brick so that, once films are interleaved with lead plates (see section 2.3.3), the tracks accumulated during transportation will be seen with a different alignment. Then, they can be eliminated at the analysis level.

In order to achieve a high resolution, two effects have to be taken into account: distortions and shrinkage, see Figure 2.10. Distortion is a phenomenon which shifts the position of the recorded trajectories in the emulsion because of stresses accumulated in the gelatin layer. The simplest form of distortion is a uniform shear: straight tracks remain straight but their direction and length change by an amount which depends on the magnitude and direction of the shear. A more serious source of error is due to differential shear of the emulsion in which both the magnitude and direction of the shear change with depth. Such distortion changes straight tracks from energetic particles into curved paths.

The shrinkage effect is due to a reduction (or increase) of the emulsion thickness after the development process. The shrinkage factor is defined as the ratio between the values of the thickness of the emulsion before and after the development. This factor is taken into account by the tracking algorithm: the measured track slopes must be multiplied by this factor to obtain the real value.

2.3.3 OPERA brick

The brick is a sandwich-like structure composed of lead plates (1 mm thick) and emulsion films [55]. The transverse size of the brick is 12.5 cm $\times$ 10.2 cm. The total amount of lead layers in a brick is 56, while there are 57 emulsion films, see Figure 2.11. The total weight of each brick is 8.3 kg.

The brick thickness is about ten radiation lengths which is large enough to allow electrons identification through their electromagnetic shower. This also allow track momentum estimation by measuring their multiple coulomb scattering consecutive emulsion-lead cells. The plate material is a lead alloy

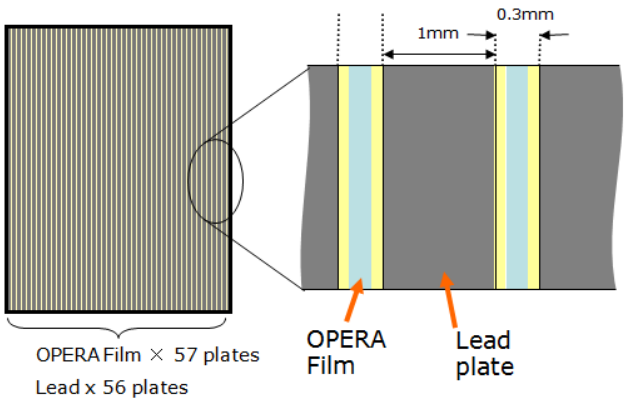

Figure 2.11: *Brick scheme.*

with a small calcium content to improve its mechanical properties; the choice of PbCa with respect to other compounds was motivated also by its low α activity, which was extensively studied [56]. A total number of 150036 bricks were assembled by a dedicated Brick Assembly Machine composed by anthropomorphous robots, ensuring a high precision in the piling up.

An automated system called Brick Manipulator System (BMS) takes care of the target filling and extraction. Two BMS robots are placed on each side of the detector and can load and unload bricks using a small vehicle equipped with a suction grip.

Changeable Sheet

A Changeable Sheet (CS) is an emulsion tracking detector attached to the downstream face of the brick [57]. It can be removed without opening the brick, acting as interface between the electronic detectors and the brick itself, see Figure 2.12. Its principal task is to confirm that the brick predicted by the electronic detector actually contains the neutrino interaction vertex, thus acting as an off-line trigger for the event reconstruction. The CS concept was successfully applied to all past hybrid experiments, like CHORUS and DONUT.

In order to accomplish the tasks for which it was designed, the CS detector is required to have an extremely low background level. For this reason it was assembled in a dedicated facility at the LNGS underground laboratory. It consists of two emulsion films called "CS Doublet" (CSD) that are packed in a light-tight envelope made of aluminum-laminated paper and then inserted in a plastic box. The films are the same as the ones used for ECC bricks, but an additional refreshing process was applied in the facility to further reduce the background, using the same conditions as in the Tono refresh facility.

If tracks related to neutrino interaction are observed in the CSD, the

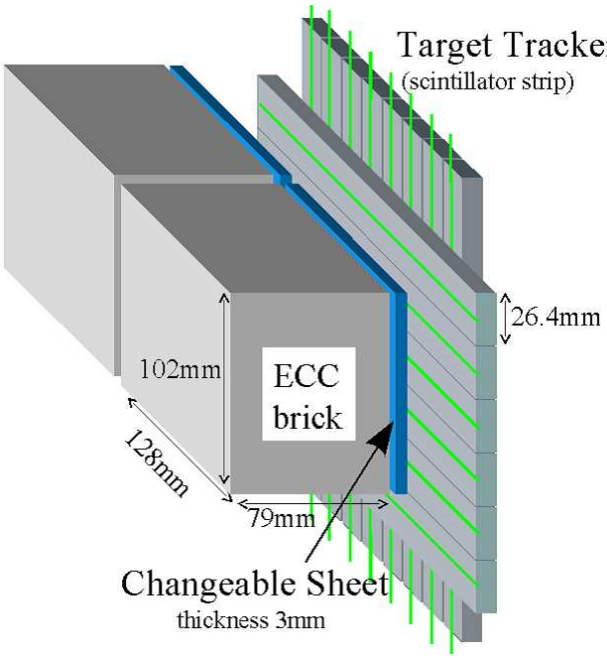

Figure 2.12: *Final configuration of brick, CS and scintillators.*

brick is dismantled, developed and analyzed. If no signal is found another CSD is attached to the brick, which is reinserted into the detector. This allows to reduce the emulsion scanning load and to save the detector target mass. CSD make possible the jump from TT resolution, of the order of 1 cm, to the 1 μm spatial resolution of nuclear emulsions. Without the help of CS and given the accuracy of the target tracker, the search of event tracks in the brick would be quite difficult.

The physical background, coming from cosmic ray tracks and Compton electrons from environmental radioactivity, is 100 tracks/cm^2/film. Requiring tracks aligned in the two emulsion films (4 emulsion layers) further reduces this background to about 10^{-4} tracks/cm^2 , which motivated the choice of two films rather than only one. In order to save the needed high purity, CSD cannot be exposed to alignment cosmic rays as it is done for bricks. That's why the alignment between films is achieved by "printing" four X-ray circular spots with a radius of 150 μm on the CSD just after the brick extraction, i.e. when the CSD is still attached to the brick. The X-rays penetrate the two CS films and the most downstream film of the brick, allowing in this way also to perform the CS-to-brick connection.

The complete flow of the OPERA emulsion can be seen in Figure 2.13.

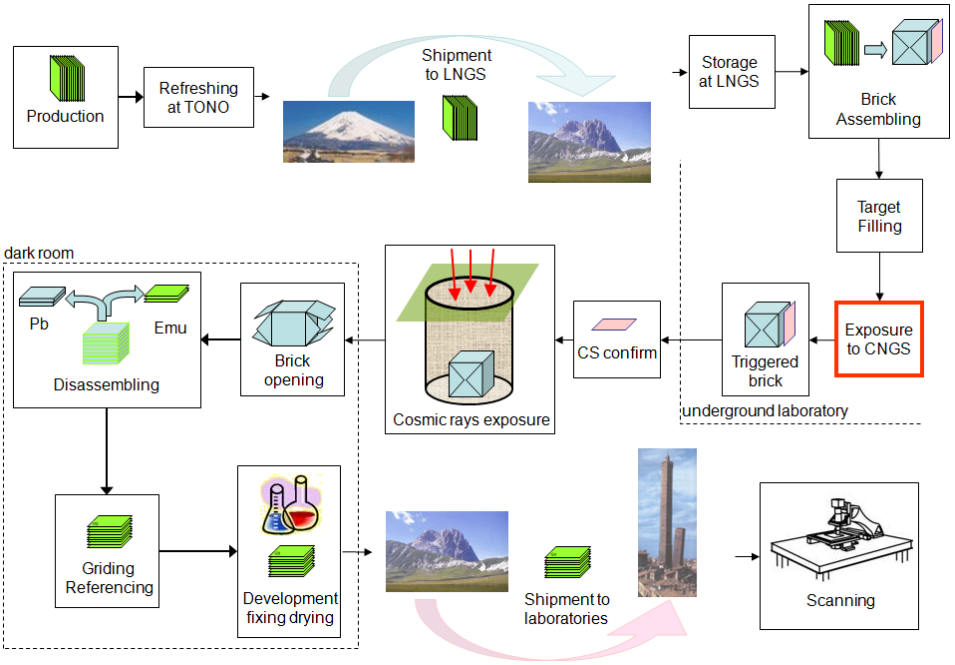

Figure 2.13: *Flow of the emulsion brick: from the production to the analysis.*

2.3.4 The European Scanning System

In the OPERA scanning laboratories the emulsion measurements are performed by an automatic scanning system, due to the large amount of emulsion to be analyzed. Two different approaches was followed by Japanese and European groups, leading to scanning systems with similar time performances and tracking efficiencies: the so called Super-UTS in Japan and the European Scanning System (ESS) in Europe. With respect to the Japanese technology, the ESS is more based on commercial hardware [58]. An example of an ESS can be found in Figure 2.14.

During the scanning, the emulsion is hold by a glass plate and its flatness is guaranteed by a vacuum system. Moving continuously the focal plane of the objective through the emulsion thickness, a sequence of 16 tomographic images of each field of view is obtained [59], where the images are taken at equally spaced depth levels. The acquired images are then converted into a gray scale of 256 levels, sent to a vision processor board, hosted in the control workstation, and analyzed to search sequences of aligned grains such as clusters of dark pixels of given shape and size. During the scanning of the bottom layer of the emulsion, the whole plastic base and the top emulsion layer lay between the objective front lens and the focal plane, for a total thickness of about 0.3 mm, while for the scanning of the top emulsion layer there is no intermediate medium. This variation of the thickness of

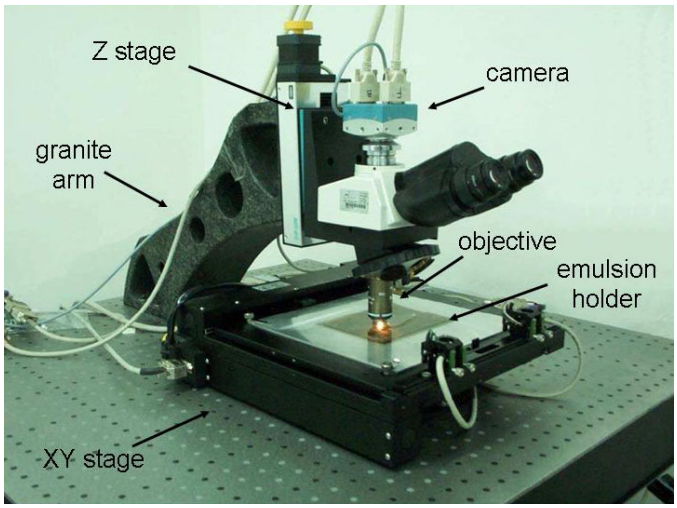

Figure 2.14: *Example of European Scanning System.*

intermediate medium could lead to distortions of the acquired images. These effects are well corrected by using an immersion oil objective. In fact oil, emulsion and plastic base have almost the same refractive index, about 1.5, and the optical path is almost homogeneous.

Some of this grains belongs to tracks, others, most of them, are accidentally developed single grain (fog, see Section 2.3.1). Therefore, the first step of the event reconstruction consists in search of micro-tracks. A micro-track is defined as a three-dimensional sequence of grains, on a single emulsion layer, which is reconstructed by combining clusters belonging to images at different levels and searching for geometrical alignments. Micro-tracks on the top and bottom emulsion layers are then connected across the plastic base to form the basetracks [60], see Figure 2.15. Basetracks and micro-tracks are measured within an angular acceptance of $\tan\theta < 0.6$, where θ is the angle between the track and the direction orthogonal to the plate. Track position and slope is determined by a linear fit to these tracks. The vision processor is able to grab and process images at rates greater than 350 frames per second, leading to a scan speed of about $20\,\mathrm{cm}^2/\mathrm{h}$ per side [61]. The scanning output is a collection of raw data files which are saved into a data base.

2.4 Event Reconstruction

Once a neutrino interaction has occurred in the OPERA detector, a software algorithm evaluates if the interaction happened inside the target area [62]. If a muon is reconstructed by the electronic detectors, the event is classified as Charged Current (CC), otherwise it is classified as Neutral Current (NC). An example of CC interaction can be seen in Figure 2.16 while a NC example can

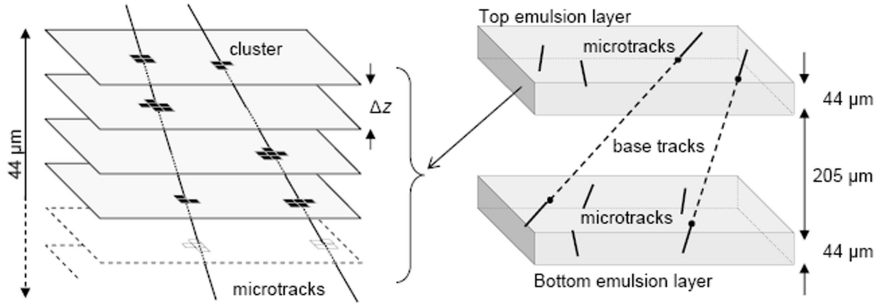

Figure 2.15: *Micro-tracks and basetracks definitions.*

be see in Figure 3.1a. The muon reconstruction efficiency by the electronic detectors is greater than 95% [63].

In case an interaction occurs in the target, a brick probability map is build in order to identify the brick containing the interaction vertex. Moreover, for CC events, a prediction for the slope of the muon and its impact on the CS is also given, while, for NC events, the averaged center of the TT hits provides the impact point of the "hadron shower" in the CS.

The brick with the highest probability is extracted from the target area by the BMS and exposed to X-rays for CS-to-brick alignment (see Section 2.3.3). Then, the CSD is detached from the brick and developed underground.

2.4.1 CS analysis and CS-brick connection

The CS films coming from a brick extraction are firstly developed at LNGS and then analyzed to validate the selected brick. In the meantime, the brick is temporary stored underground in a shielded area, in order to reduce the integration of cosmic rays. The CS scanning is done in two scanning stations: one at LNGS, equipped with eight European Scanning System, and the other in Japan. Each scanning station analyses half of the CSD collected by OPERA.

In order to validate a brick, the CS analysis result has to present one of the following signatures:

- a pattern of at least two converging tracks;
- a track candidate matching a muon reconstructed by the electronic detectors, if present;
- a track compatible with an isolated track well reconstructed by the electronic detectors.

Figure 2.17 shows the residuals between muon tracks measured in the CSD and their predictions provided by the electronic detectors.

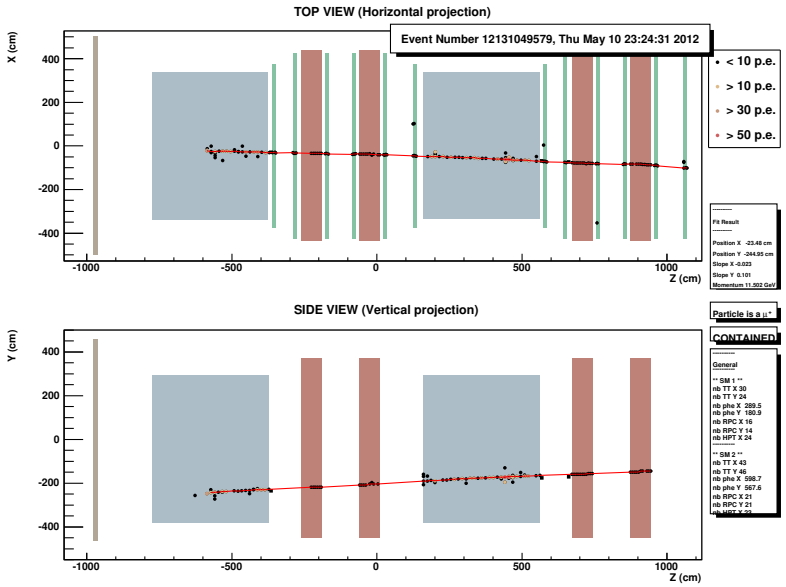

Figure 2.16: *Example of CC interaction in the target area of the first SM. The red curves represent the linear fit performed to the hits belonging to the reconstructed muon.*

After validation, the brick is brought to surface to be exposed to high-energy cosmic rays, which are needed in order to perform a precise film-to-film alignment. It is done placing the brick emulsion planes perpendicular to cosmic rays, under a shielding structure (the cosmic pit) made of iron and plastic slabs used to absorb soft radiation [65]. The exposure lasts 12 hours, corresponding to about one penetrating track per mm^2 in the angular acceptance relevant for the scanning. The brick emulsion films are then developed with an automatic system in parallel processing chains and then dispatched to the scanning laboratories.

The next step consists in connecting the CS candidates with the basetracks in the last emulsion of the brick. This represents a very crucial phase due to the fact that the CSD is 4500 μm far from the brick. All CS tracks positions are projected to the most downstream sheet of the brick and an area of about 1 mm^2 is scanned around each prediction. Using a position tolerance of 300 μm and an angular acceptance of 60 mrad, candidates tracks are selected, so-called connected. The residuals between CSD predictions and connected basetracks can be seen in Figure 2.18. All connected tracks are selected to be the input of the scanback procedure.

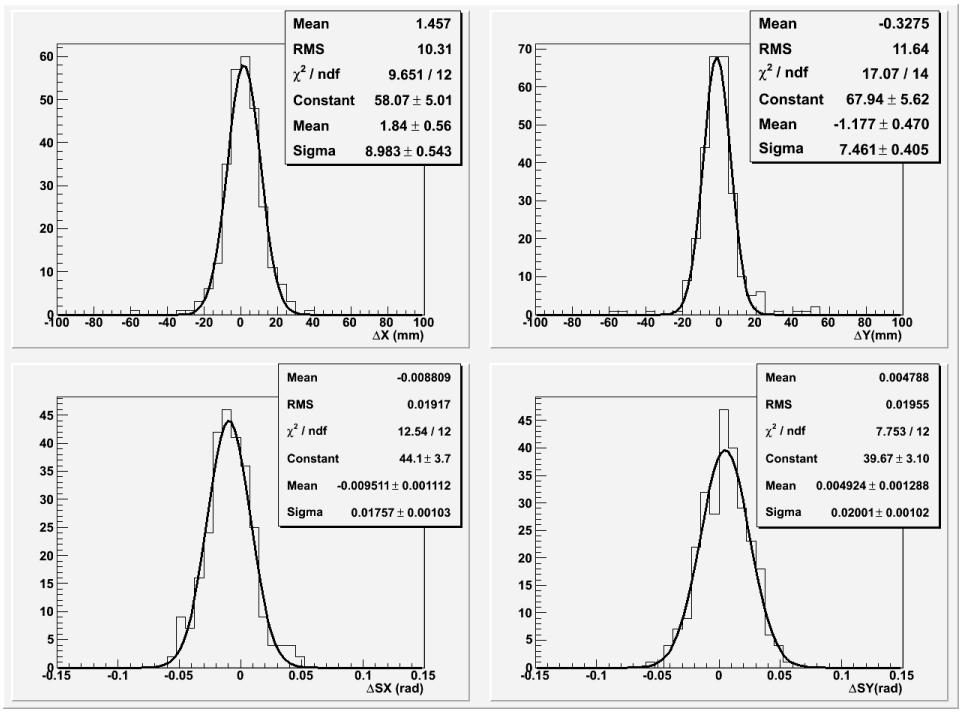

Figure 2.17: *Residuals between tracks tagged as muons in the CSD and the corresponding electronic detectors reconstructed tracks for CC interactions [64]. On top there are the position residuals in x (left) and y (right) directions; on the bottom part the slope residuals in x (left) and y (right) directions are displayed.*

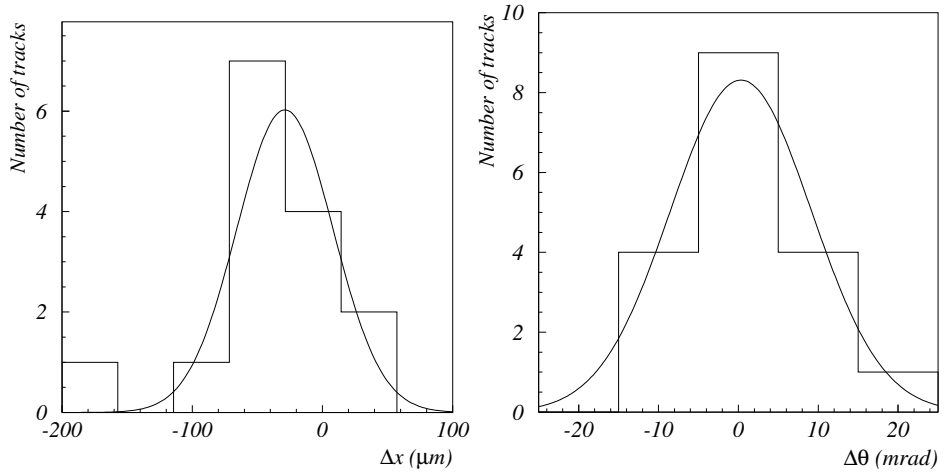

(a) *Position residuals* **(b)** *Angular residuals*

Figure 2.18: *Distributions of position and angular residuals of high energy cosmic-ray tracks measured in the CSD and in the most downstream emulsion film of the ECC brick [57]. Fitted Gaussians have averages and variances equal to* $-29\,\mu$m *and* $37\,\mu$m *(position) and* $0.3\,$rad *and* $9\,$rad *(angle).*

2.4.2 Scanback procedure

The scanback is the procedure used to localize the neutrino interaction point inside the brick. The scanback starts from track positions and slopes in the most downstream sheet and then the track coordinates in the next upstream plates are predicted. An automatic system searches for basetracks compatible with the predictions by scanning a single microscope view centered at the expected position. This process is iterated until no segments are found in at least five consecutive plates or the track exits the brick.

In the first case, the last plate where the track is reconstructed is called stopping point. Further manual checks are performed on the scanback stopping point in order to check the goodness of the track reconstruction. The plates upstream with respect to the stopping point are also manually checked to confirm the stopping point.

If the track exits the brick, the neutrino interaction did not take place in the brick under examination. If the track exits from the most upstream plate, the primary vertex can be in the upstream brick and the track is called "passing-through". Otherwise, if the track exits through an edge, the primary vertex will be searched in an adjacent brick, and this track will be called "edge-out". When one of these cases occur, the brick suggested by the previous measurements is extracted, its CS doublet is also scanned, in order to search for more tracks related to the event. The scanback procedure is repeated as explained for the first brick. Some neutrino interactions occurs in

the target frame, or in the target tracker detector, which are considered dead materials. Such a kind of events can not be used for the neutrino oscillation search, because the vertex region cannot undergo the topological analysis.

2.4.3 Vertex reconstruction

Whenever a scanback stopping point is found, a procedure called total scan is applied in order to confirm or disprove the interaction and study its topology. This procedure consists in a volume scan performed over a $1\,\text{cm} \times 1\,\text{cm}$ area in 5 upstream and 10 downstream films with respect to the stopping point. The Total scan volume is aligned maximizing the number of almost perpendicular tracks (cosmic rays) passing through the 15 plates. The alignment is done applying solid rotations to the emulsion plane and evaluating shrinkage corrections to all the scanned foils. Volume tracks are reconstructed in the aligned volume using basetracks measured in the single emulsion layers; this procedure is called tracking. The interaction vertex is reconstructed evaluating all the possible intersections between the reconstructed tracks at the stopping plate. Its position is defined by maximizing the number of tracks attached to the vertex and by minimizing their impact parameters. This step is called vertexing.

For vertexing, the usage of track information in the film immediately downstream of the neutrino interaction point (hereafter referred to as vertex film) is crucial in order to improve the resolution in the determination of its position. Track segments in the vertex film could be missing in the reconstruction because of tracking inefficiency. So, a manual check is performed in order to look for missing tracks. If found, they can be used to re-compute the vertex position. Moreover, electron-positron pairs coming from the conversion of photons produced in π^0 decays and pointing to the vertex can downgrade the vertex reconstruction accuracy. Anyway, electron-positron pairs can be identified as couples of very-close converging segments and can be thus tagged and removed in the determination of the vertex position. Once these pairs are discarded, the vertex point is re-evaluated.

Reconstruction of tracks and vertices is accomplished by an automatic software. The tracks used for scanback are searched among all the reconstructed tracks. There can be three possible results for this matching procedure.

- The reconstructed scanback track belongs to a vertex with an upstream track (parent track). In this case the vertex is assumed to be an hadronic interaction and the scanback procedure continue with the parent track.
- The reconstructed scanback track belongs to a vertex without a parent track. In this case the vertex is the neutrino interaction vertex candidate.
- The reconstructed scanback track doesn't belongs to any vertex. This could happen if no other track in the volume is associated to the event.

In this case the neutrino interaction point can not be estimated and the stopping points of all scan-back tracks have to be re-checked.

In the last two cases further checks are performed to confirm that the candidate vertex is the neutrino interaction one and if it is worth to study the topology and search for secondary vertices.

2.4.4 Decay Search

If a reconstructed vertex is found following the procedure described in Section 2.4.3, a procedure is applied in order to better define the neutrino interaction point.

Once a vertex point is defined, any track with an anomalous impact parameter (IP $> 10\,\mu$m) that can not be explained in terms of scattering has to be carefully investigated. In fact, these tracks are hints for the presence of a possible short decay, occurring in the same lead plate as the neutrino interaction. The decay of a short-lived particle can be also detected by searching for possible daughter tracks, hereafter called extra-tracks, among those reconstructed in the measured volume and stopping therein. The selection of the extra-tracks is done according to the following criteria:

- the longitudinal distance between the vertex and the most upstream segment of the track (Δz) is required to be smaller than 3.6 mm;
- the impact parameter with respect to the vertex has to be smaller than $300\,\mu$m if $\Delta z < 1$ mm, or smaller than $500\,\mu$m otherwise;
- the track must have at least three segments in the reconstruction.

Additional criteria are required for NC-like events, where an ambiguity could exist on the primary vertex definition. For example, a multi-prong vertex with multiplicity three could be the secondary vertex generated by a $\tau \rightarrow 3h$ decay, unlike for events with a reconstructed μ^-, where the neutrino interaction point is clearly identified through the muon track. If the multiplicity is lower than three, extra-tracks satisfying the following criteria are selected as well:

- the most upstream segment has to be in any of the two emulsion film upstream of the vertex;
- the impact parameter with respect to the reconstructed vertex must be smaller than $500\,\mu$m.

Extra-tracks are then inspected to filter out electron pairs from conversion, particles not originating in the measured volume (typically, low momentum particles reconstructed as shorter tracks due to multiple Coulomb scattering) and fake tracks due to the failure of the reconstruction program. The latter

is relevant especially for bricks characterized by a high density fog. Surviving extra-tracks originating in the vertex film are analyzed to check if they are low momentum tracks using the multiple scattering methods described in Section 2.4.5.

A dedicated parent search procedure is applied to the extra-tracks starting downstream of the vertex film to detect long decays. It consists in searching for a track connecting the selected extra-track to the reconstructed vertex with an impact parameter with respect to the vertex smaller than $10\,\mu$m. In addition the minimum distance between the considered basetrack and the daughter track has to be smaller than $20\,\mu$m. Any candidate parent track selected according to these criteria is validated by visual inspection. The same procedure applies to extra-tracks originating upstream of the vertex for NC-like events.

The presence of possible heavy ionizing particles produced at the secondary vertex provides discrimination between hadronic interactions and particle decays. Such tracks have an higher grain density and they look like dark black tracks.

The automatic scanning procedure could not reconstruct small kinks along the tracks during previous procedures. Therefore, a further search for small kinks is performed for all the primary tracks in the four nearest plates to the reconstructed vertex [53].

2.4.5 Momentum measurement

Emulsions are a very powerful trackers, but this is not enough for a complete event reconstruction: the momenta of the reconstructed tracks are also necessary. For MIP like muons or pions coming from neutrino interactions the momentum is estimated measuring the Multiple Coulomb Scattering (MCS) of the track in lead [66]. The selected approach uses the angle differences measured in pairs of emulsion films separated by lead.

In the following, the *cell* is defined as one lead plate and one film. Being θ_i the angle of a given base-track in the i-th emulsion film in the xz or yz projection plane, it is possible to define $\theta_{ik} \equiv \theta_{i+k} - \theta_i$ as the scattering angle after crossing k cells, see Figure 2.19. Its distribution is peaked at zero and has a shape that can be approximated by a Gaussian with a standard deviation given by

$$\theta_0 = \frac{13.6\,\mathrm{MeV}}{pc\beta}\sqrt{\frac{x}{X_0}}\left[1 + 0.038\ln\left(\frac{x}{X_0}\right)\right] \tag{2.1}$$

where p and $c\beta$ are the particle momentum and velocity, x is the distance traveled in the material and X_0 is the interaction length of the material. The accuracy of this approximation of Moliere's theory of scattering is better than 11 % in any material, with $0.001 < x/X_0 < 100$ for single charged particles with $\beta \sim 1$ [67].

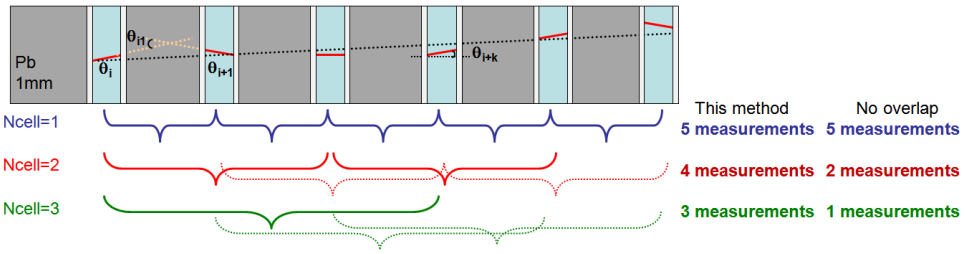

Figure 2.19: *Representation of the number of possible measurements available when applying the multiple Coulomb scattering method up to* $N_{cell} = 3$.

In the OPERA case, the scattering is dominated by lead since the radiation length in the emulsion layers and the plastic base is larger by more than one order of magnitude. For this reason, the lead value $X_0 = 5.6$ mm is assumed in the analysis and a thickness of 1 mm is used for each cell, neglecting the emulsion films. So, Equation 2.1, as a function of the cell size, N_{cell}, has the form

$$\theta_0\left(N_{cell}\right) = \frac{13.6\,\mathrm{MeV}}{pc\beta}\sqrt{\frac{N_{cell}}{5.6}}\left[1 + 0.038\ln\left(\frac{N_{cell}}{5.6}\right)\right] \tag{2.2}$$

The variance of the scattering angle distribution for a given cell depth $N_{cell} = k$ is given by

$$\theta^2_{meas}\left(k\right) = \sum_i \frac{(\theta_{ik})^2}{N_{meas}(k)} = \theta_0^2(k) + \delta\theta^2 \tag{2.3}$$

$$\text{and} \quad N_{meas}\left(N_{cell}\right) = \sum_{i=1}^{N_{cell}} int\left[\frac{N_{pl} - i + 1}{N_{cell}}\right] \tag{2.4}$$

where N_{meas} is the number of scattering angle measurements and $\delta\theta$ is an additional term corresponding to the base-track angular resolution. The current experimental value of $\delta\theta$ is about 2.1 mrad.

In order to determine the momentum up to a few GeV/c, a fit of the dependence of θ_{meas} on the number of crossed cells is performed, treating p as a free parameter and fixing the angular resolution $\delta\theta$. Fit examples can be seen in Figure 2.20, for Monte Carlo samples. With increasing p, multiple Coulomb scattering starts dominating over $\delta\theta$ at larger values of N_{cell}, where the number of available measurements decreases, thus increasing the statistical error. So, in order to improve the sensitivity to high-momentum tracks, it is important to reduce the statistical uncertainty at large crossed thicknesses. Clearly, the method performances depend on the momentum and on the number of planes crossed by the particle (N_{pl}): see Figure 2.21.

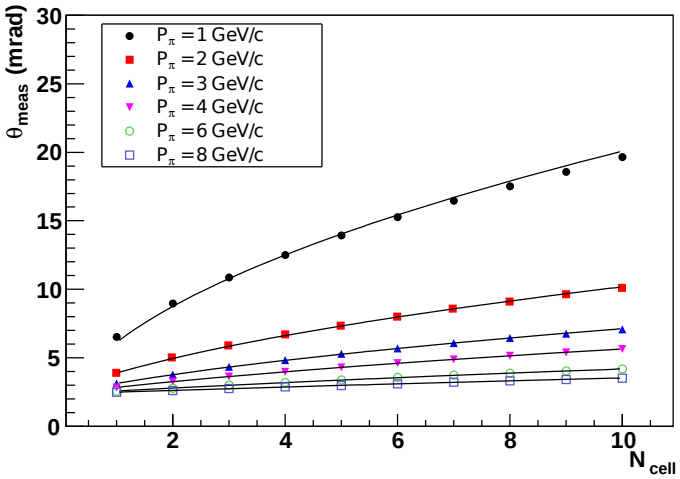

Figure 2.20: *The θ_{meas} dependence on N_{cell} for Monte Carlo pions of different energies, where $\delta\theta$ has been simulated at a value of $\delta\theta = 1.67$ mrad. The solid curves correspond to the fitted expectations.*

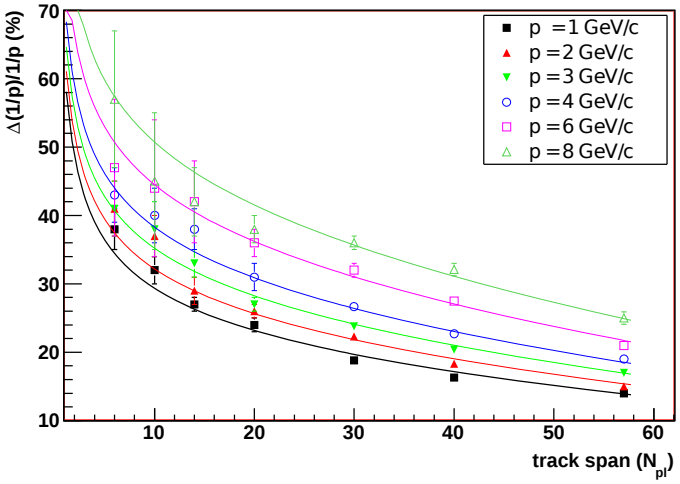

Figure 2.21: *Momentum resolution dependence for MCS evaluation method. The resolution is presented as a function of crossed layers (N_{pl}) for Monte Carlo pions with simulated $\delta\theta = 1.67$ mrad*

Table 2.1: *Tau decay branching ratios [34] and tau detection efficiencies [68]. Each decay channel includes also possible neutral daughters, such as π^0 or photons. The efficiencies are evaluated for three different decay topologies.*

Channel	BR (%)	Detection efficiency (%)		
		Long DIS	Short DIS	Long QE
$\tau \to e^-$	19.6	10.6 ± 0.5	7.5 ± 0.5	0.3 ± 0.1
$\tau \to \mu^-$	17.8	18.6 ± 0.8	$7.7\pm$ 0.8	8.6 ± 0.2
$\tau \to h^-$	47.4	8.9 ± 0.8	5.5 ± 0.8	1.2 ± 0.2
$\tau \to 3h^-$	15.2	10.1 ± 0.6	7.5 ± 0.5	0.3 ± 0.1

2.5 Tau Physics

The procedure described in Section 2.4 is applied to recorded events in order to search for tau decays. This search aims for short decays with no muon attached at the primary vertex. The searched decay products, according to the τ branching ratios are

- an electron
- a muon
- one hadron
- three hadrons

The efficiency depends on the interaction type, DIS or QE, on the position of the primary vertex inside the lead layer and on the τ flight length. In particular, if the tau crosses at least one emulsion layer, the decay is called "long", otherwise it is "short". The only interaction type which allows the reconstruction of a short tau decay is the DIS one. In this case, the other particles coming out from the primary vertex are used to obtain its position and the tracks impact parameters can be evaluated. Otherwise, the position of the vertex is unknown and no impact parameters can be retrieved from the measurements. Table 2.1 shows the detection efficiencies for each decay channel and interaction types.

For this search, there are two main background sources. The first one is due to charm produced in ν_μ CC interactions. Charmed mesons have a mass similar to the tau one and they all decay through weak interaction (W exchange). Thus tau and charm have a similar lifetime and similar decay products. If the muon coming from the primary vertex is not identified, the charm topology can mimic the tau decay. The second background source is the re-interaction of an hadron coming from the primary vertex in the brick lead. This was studied using dedicated OPERA bricks exposed to pions

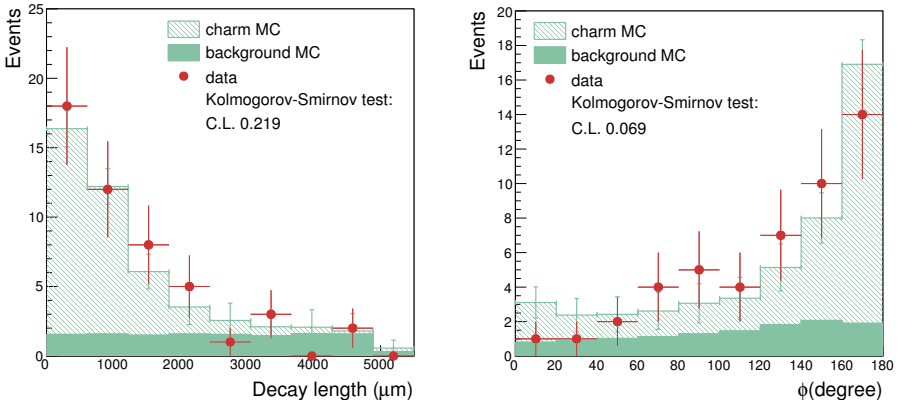

Figure 2.22: *Shape comparison between observed ν_μ CC interactions with candidate charm decays and MC expectations. (a) distribution of the decay length of the candidate charmed particles. (b) distribution of the angle between the candidate charmed particle and the primary muon in the ν transverse plane. The expected background contribution is also shown (stacked histogram).*

beams. Hadronic re-interaction affects mostly the hadronic decay channels. A minor background source is the large angle Coulomb scattering of muons inside the lead. This is a source of background just for the $\tau \to \mu$ decay channel.

The whole analysis procedure can be tested using the ν_μ CC interactions with Charm production [69]. This test has been carried on a sub-sample of the OPERA data set, lead to the expectations of 40 ± 3 charm event over a background of 14 ± 3 events coming from hadron re-interactions and strange particle decays. The observed candidates were 50 and good agreement was observed between data the corresponding MC distributions, see Figure 2.22.

2.5.1 Selection criteria

In order to remove backgrounds, the requirements to select tau candidates are not merely topological: there are strong kinematic constraints depending on the decay channel, see Table 2.2. The selection criteria have been kept fix since the very beginning of the experiment. This selection is very strict, in order to minimize background events, and the selection efficiency is not large.

The tau selection is based on several variables evaluated from the event.

Decay z (z_{dec}) is the z position of the secondary vertex with respect to the primary vertex plate.

Table 2.2: *Selection criteria for tau candidates. The value denoted by * is used when a reconstructed EM shower is connected to the kink.*

variable	$\tau \to h$	$\tau \to 3h$	$\tau \to \mu$	$\tau \to e$
lepton-tag	No μ or e at the primary vertex			
z_{dec} (μm)	$[44; 2600]$	< 2600	$[44; 2600]$	< 2600
p_T^{miss} (GeV/c)	< 1	< 1	–	–
ϕ_{lH} (rad)	$> \pi/2$	$> \pi/2$	–	–
p_T^{2ry} (GeV/c)	$> 0.6\,(0.3)^*$	–	> 0.25	> 0.1
p^{2ry} (GeV/c)	> 2	> 3	> 1	> 1
θ_{kink} (mrad)	> 20	< 500	> 20	> 20
m, m_{min} (GeV/c^2)	–	> 0.5 and < 2	–	–

Missing transverse momentum (p_T^{miss}) is the module of the missing transverse momentum at the primary vertex.

Lepton-hadron transverse angle (ϕ_{lH}) is the angle in the transverse plane between and the parent track and the hadron shower direction. ϕ_{lH} can only be used if there is at least one fully measured track besides the candidate tau parent at the primary vertex.

Momentum at secondary vertex (p^{2ry}) is the total momentum of the visible tracks coming out from the secondary vertex.

Transverse momentum at secondary vertex (p_T^{2ry}) is the transverse component of p^{2ry} with respect to the parent direction.

Kink angle (θ_{kink}) is the kink between secondary vertex parent and daughters. The lower cut was assigned taking into account the angular resolution of the OPERA emulsions. For the three prong case, there is an upper cut for each of the three daughters: this is motivated by considerations related to the scanning efficiency of the automatic microscopes.

Invariant mass (m) is a variable used for the three hadrons decay channel. Together with the invariant mass, also the minimum invariant mass (m_{min}) is required [70]. This is a quantity that takes into account neutrino which can be produced in the decay process. Both of them have to be within 0.5 and 2 GeV/c^2.

The total efficiency is summarized in Table 2.1 and it comprehends all the steps of the analysis, from the electronic detector reconstruction to the decay search. The expected events for signal and background according to each tau decay channel are presented in Table 2.3.

Table 2.3: *Expected signal and background events for the analyzed OPERA data sample [49].*

Channel	Background	Tau
$\tau \to h$	0.04 ± 0.01	0.52 ± 0.10
$\tau \to 3h$	0.17 ± 0.03	0.73 ± 0.14
$\tau \to \mu$	0.004 ± 0.001	0.61 ± 0.12
$\tau \to e$	0.03 ± 0.01	0.78 ± 0.16
Total	$\mathbf{0.25 \pm 0.05}$	$\mathbf{2.64 \pm 0.53}$

2.5.2 Status of the OPERA experiment

The OPERA data taking period lasted from 2008 to 2012. The total proton amount delivered on the graphite target at CERN was lower than the proposal, by about the 20%. Nearly 17000 events were recorded in the target volume and, for almost each of them, at least one brick was extracted from the detector. The number of event fully analyzed, with a completed decay search is about 6500, see Figure 2.23.

Out of the decay searched sample, 5 events were reported fulfilling the topology and kinematic requirements for being tau candidates. The observed decay channels are $\tau \to h$ (3 events) [71, 72, 49], $\tau \to \mu$ (1 event) [73] and $\tau \to 3h$ (1 events) [74]. The significance of this observation, with respect to the background only hypothesis, is $5.1\,\sigma$ [49]. First and third candidates event displays can be seen in Figure 2.24 and 2.25, respectively.

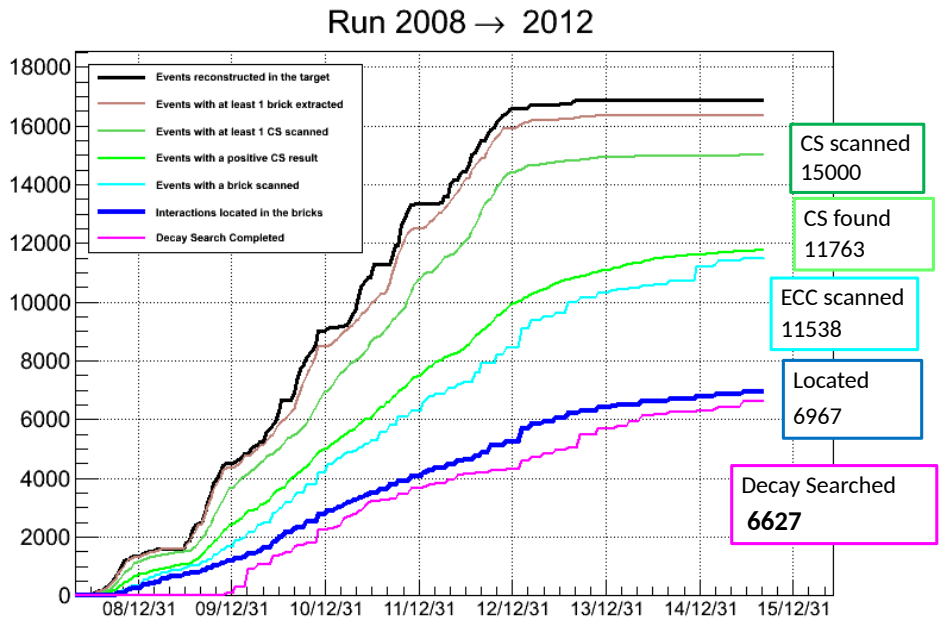

Figure 2.23: *Status of the OPERA experiment updated at 06/09/2015. The curves are, from top to bottom: events reconstructed in the target, events with at least one brick extracted, events with at least one CS scanned, events with a positive CS result, events with a brick scanned, interactions located in the brick and decay search completed.*

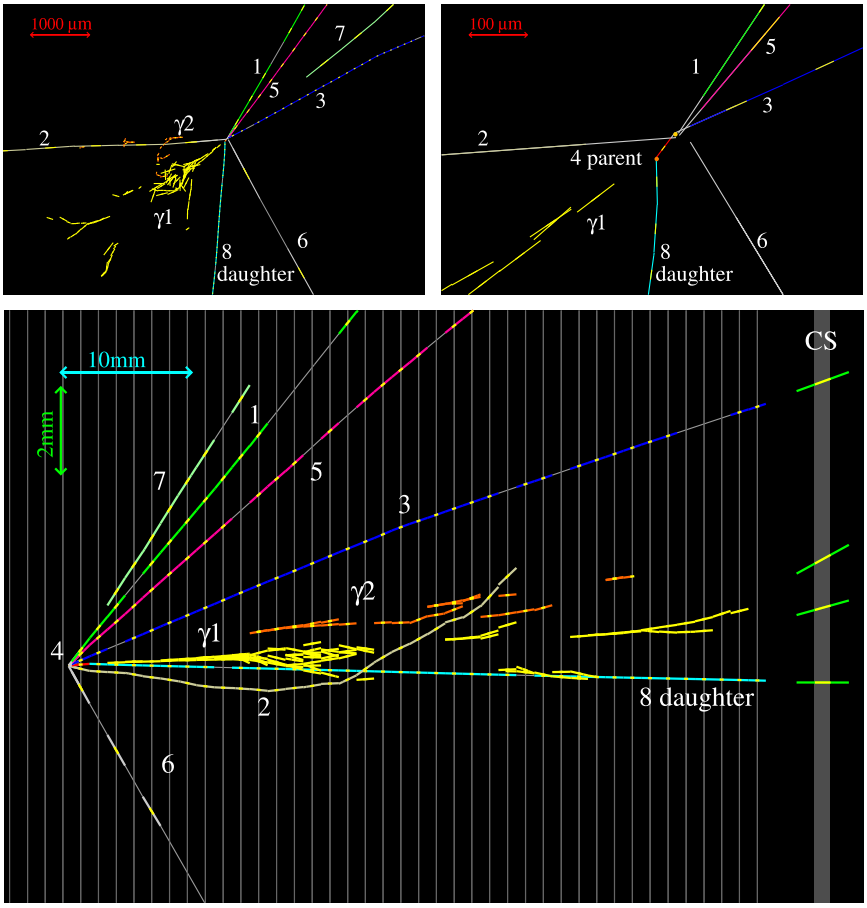

Figure 2.24: *Display of the first ν_τ candidate event [71]. Top left: view transverse to the neutrino direction. Top right: same view zoomed on the vertices. Bottom: longitudinal view.*

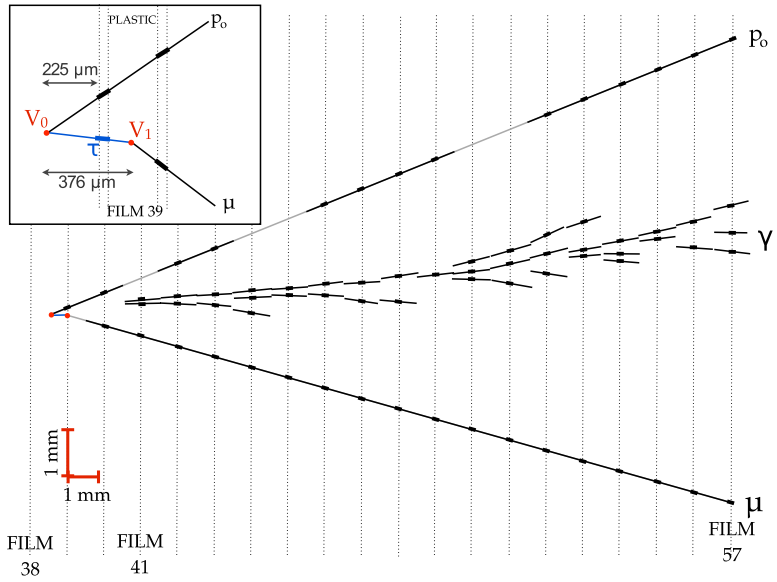

(a) *Emulsion*

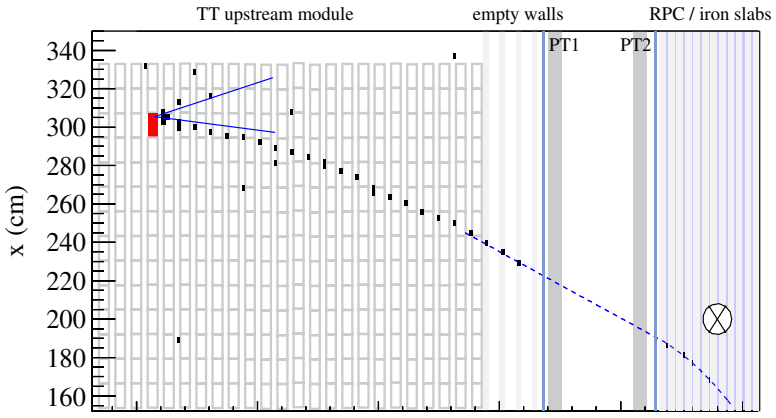

(b) *Electronic detectors*

Figure 2.25: *Display of the third ν_τ candidate event [73]. Emulsion plots show in the xz projections. Tracks τ and p_0 come from the primary vertex; the τ candidate decays in the plastic base of film 39, and track d_1 is the τ decay daughter identified as a muon. The starting point of the shower generated from the photon is visible in film 41. The electronic detector display shows also the xy view. The blue solid lines represent the linear extrapolation of tracks measured in the emulsion films of the vertex brick. The dashed blue lines show the fit of the most downstream hits.*

Chapter 3

Event with two secondary vertices

On May 23rd 2011 a new interesting event was recorded. After the standard OPERA analysis procedure, the primary vertex was located in the first analyzed brick. The decay search procedure identified a peculiar topology: instead of one, there are two secondary vertices. One of them is very close to the primary, in the same lead layer, while the second was found in the downstream plate. This topology is extremely rare and no event of this kind was expected to be found. Therefore, a dedicated analysis was set-up in order to identify the underlying process.

This chapter is the very introduction of this dedicated analysis: it aims to describe the event and its possible interpretations. The analysis strategy is also discussed.

3.1 Event Reconstruction

As described in Chapter 2, OPERA analyses are based on combined information from both electronic detectors and emulsions, each of them being able to retrieve different data on the occurred events. Both of them are important in order to describe and understand this interesting event.

3.1.1 Electronic detector

The event 11143018505 occurred in the first SM, close to the detector rock side, Figure 3.1. The event activity is contained inside the apparatus and the number of walls crossed by the event is 9. No muon track was reconstructed by standard OPERA algorithms, therefore the event is classified as Neutral Current (NC). Any failure of the track reconstruction algorithm is also excluded due to the absence of any tail of hits. The total energy collected by the TT is about 530 MeV, which corresponds to about 20 GeV of hadronic

Table 3.1: *Most upstream basetracks for each of the event tracks. The z coordinate is referred to plate 57 and its quoted values are the track's positions on the uppermost surface of the emulsion's top layer.*

Track ID	x (μm)	y (μm)	z (μm)	plate ID	θ_x (rad)	θ_y (rad)
1	14973.5	59018.3	-32500	32	-0.230	-0.275
2	15145.0	59075.7	-32500	32	0.121	-0.144
3	15251.2	59133.3	-32500	32	0.349	-0.036
4	15073.8	59211.3	-32500	32	-0.003	0.088
5	15073.5	59141.4	-32500	32	-0.003	-0.025
6	15034.9	59333.4	-31200	33	-0.096	0.079

energy released in the detector, according to the algorithm for the hadronic energy estimation [63]. Brick number 1077152 is the first brick suggested for the extraction; it was located in wall 12, row 23 and column 10. No other brick was extracted since the primary vertex was found in the first one.

3.1.2 Topology the primary vertex

The CSD was analyzed and 27 candidates tracks were identified, then the brick was developed. Eleven of these were found in the brick, presenting a converging pattern, confirming the hint for the neutrino interaction presence, see Figure 3.2. The standard scanback procedure was applied and a stopping point was found in plate 32.

In plate 32, five basetracks were reconstructed, their details can be seen in Table 3.1: these are the base-tracks used to define the primary vertex position. According to these measurements, it was not possible to attach all five tracks to a single vertex having all Impact Parameters (IP) lower than 10 μm, see Table 3.2. Also, IPs with respect to a single vertex are surprisingly high for a vertex reconstructed so close to an emulsion layer. The most probable configuration is obtained when two vertices are reconstructed. The primary vertex, labeled as I in Figure 3.3, is 581.8 μm upstream with respect to the top emulsion of plate 32, while the secondary vertex (II) is just 102.6 μm downstream with respect to the primary one, see Table 3.3. Vertex I is the one connected to tracks 4 and 5, while vertex II is the origin of tracks 1 and 3. Figure 3.3 presents the transverse projection (xy plane) of the event showing the measured grains and micro-tracks belonging to each track at plate 32: the necessity for the multiple vertices topology can be clearly seen.

Two different configurations can be obtained by attaching track 2 to the primary or to the secondary vertex II. In both cases the track impact parameter with respect to any of the vertices is below the threshold value required by the decay search procedure, set to 10 μm. Also, in any of these two configurations, the vertices positions remain almost constant. By maximizing the so called the vertex topological probability – a quantity that weights each

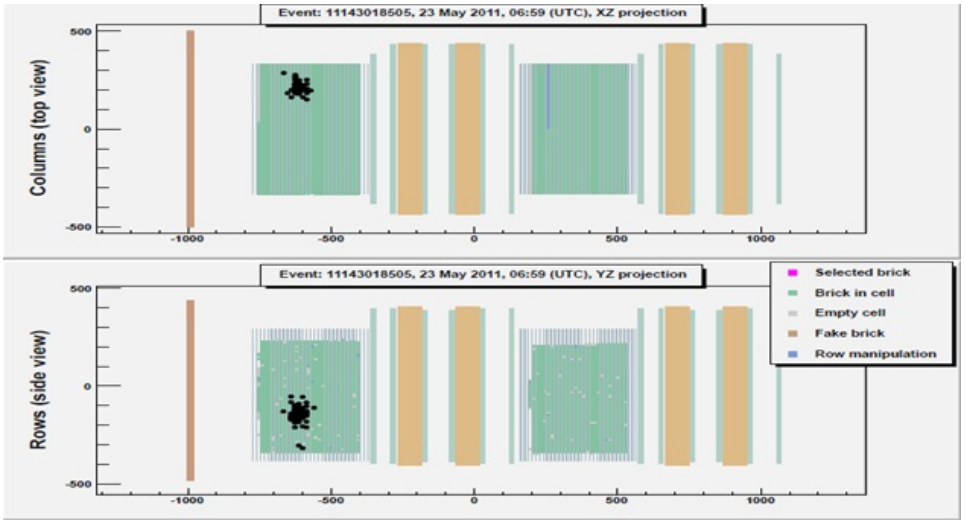

(a) Whole detector

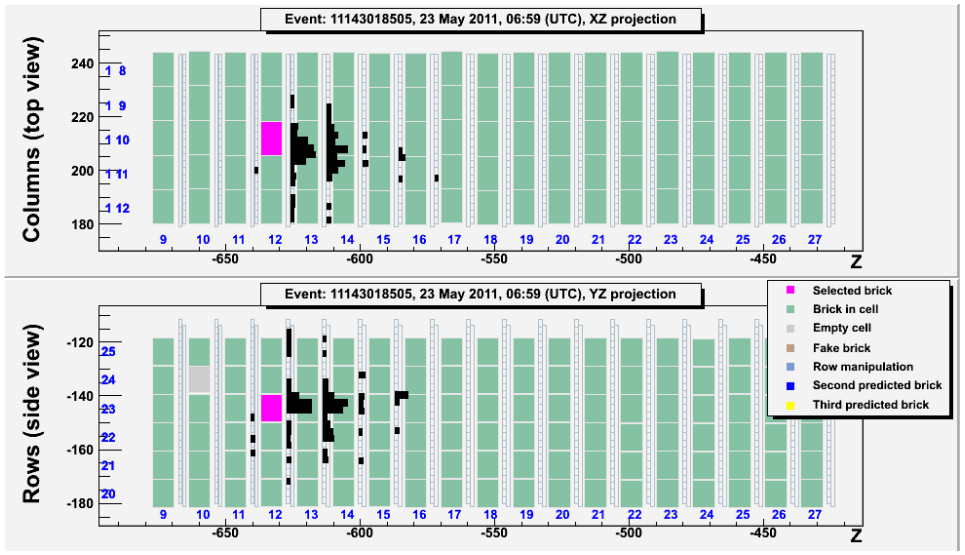

(b) Closer view

Figure 3.1: *Electronic detector views of the event in the xz projection (top), and yz projection (bottom). (a) shows the entire detector activity, while (b) is a closer view which contains only the digits on-time with the event, excluding cross-talk.*

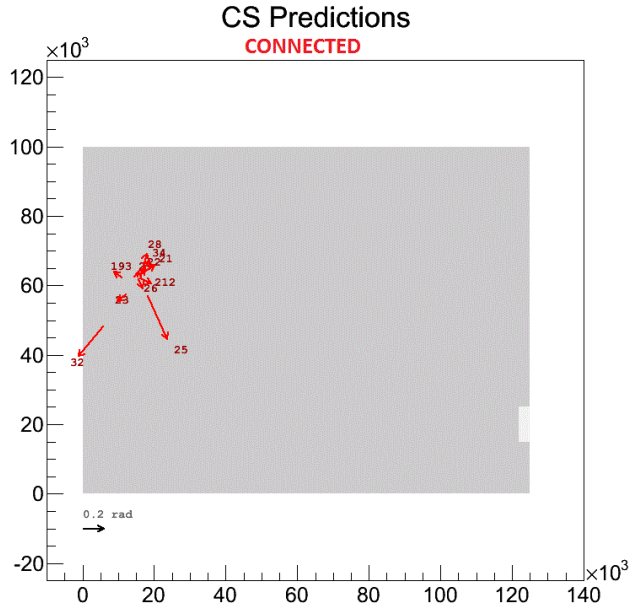

Figure 3.2: *CS candidates connected to basetracks at plate 57. As can be seen, the base-tracks show a converging pattern.*

Table 3.2: *Primary vertex impact parameters evaluated assuming a single vertex hypothesis and a two vertices hypothesis. The single vertex, V_0 has coordinates $x = 15083.4\,\mu$m, $y = 59151.5\,\mu$m and $z = -32999.0\,\mu$m. Vertices V_I and V_{II} are defined in Table 3.3*

	Single Vertex IP (μm)	**Two vertices IP** (μm)	
Track ID	w.r.t. V_0	w.r.t. V_I	w.r.t. V_{II}
1	8.3	36.2	0.1
2	8.8	1.0	6.5
3	4.8	25.9	0.1
4	13.0	1.5	20.4
5	5.1	2.2	9.6

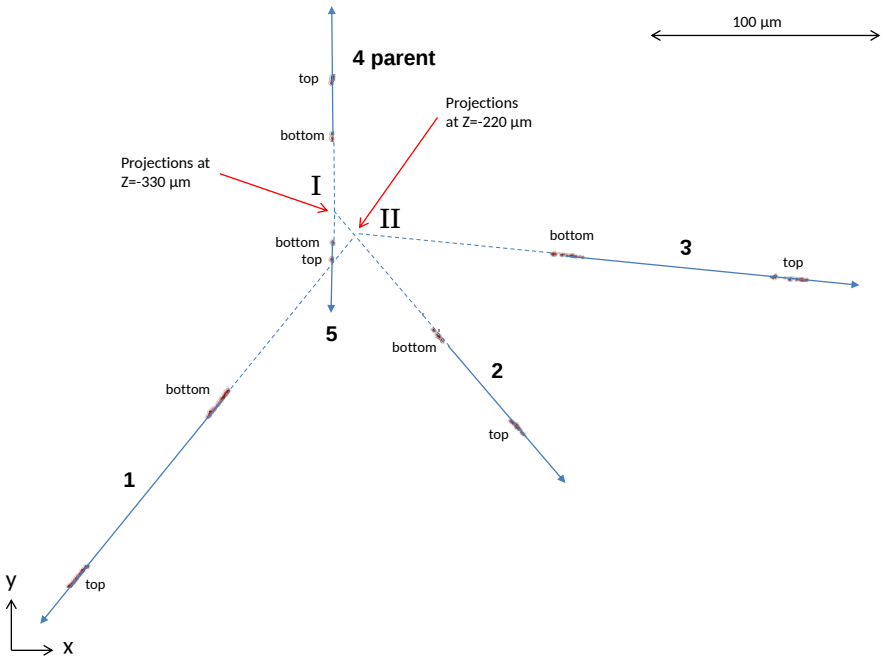

Figure 3.3: *Projection on the xy plane of the micro-tracks recorded in the stopping plate, number 32. Directions are indicated with solid lines and projections are represented with segmented lines. The two vertices topology is clearly visible.*

Table 3.3: *Position inside the brick of the reconstructed vertices. The z coordinate is evaluated with respect to the top of the last brick emulsion, plate 57.*

Vertex ID	Attached tracks	x (μm)	y (μm)	z (μm)
I (primary)	2, 4, 5	15077.0	59157.9	-33081.8
II (secondary)	1, 3	15085.9	59149.9	-32979.2
III (kink)	4, 6	15073.9	59262.4	-31926.4

track by its momentum when the vertex is defined – track 2 is attached to the primary vertex. Therefore, the most probable configuration consists of a primary vertex I whose daughters are tracks 2, 4 and 5; while tracks 1 and 3 are coming from secondary vertex II.

3.1.3 Tracks scanforth

The tracks reconstructed at plate 32 were followed down in the brick in order to estimate their momenta and to double confirm that they belong to the event by checking their presence in the CS.

Track number 4 performs a 90 mrad kink 574 μm downstream to plate 32 and, after this kink, the track proceeds very straight starting from plate 33 up to the last brick plate, looking like an high energy track. Because of the high momentum, this kink can not be explained by multiple Coulomb scattering and, also, the kink is greater than the 20 mrad tolerance, therefore a new vertex (III) and a new track (labeled as 6) are defined. Figure 3.4 shows position and direction residuals of each basetrack measured for track 6 and clearly supports the necessity of a new vertex defined between plates 32 and 33. The minimum distance between track 4 (from now on called parent) and track 6 (denoted as daughter) is $0.9 \pm 2.9\,\mu$m. The meaning of such a small number is that tracks 4 and 6 clearly point to each other even if their directions are different. The parent flight length is 1160 μm. The reconstructed positions for the three vertices are listed in Table 3.3.

Track 2 stops at plate 34, meaning that it is formed by just three basetracks. Several additional scans and manual checks were performed looking for a re-interactions of this track with negative results. Track 3 performs a re-interaction kink at plate 53 and this is interpreted as an hadron re-interaction, while track 1 goes straight to the last plate.

With the standard decay search procedure two electromagnetic (EM) shower seeds (electron - positron pair) were identified at plates 35 (labeled EM shower 1) and 41 (EM shower 2). In order to reconstruct all of them, a dedicated procedure was applied to the brick. An extensive scan, within an area of 2 cm $\times$ 2 cm, was performed to all the plates downstream with respect to plate 34. Two EM showers were indeed reconstructed and their main features are listed in Table 3.4. In order to evaluate the origin vertex of

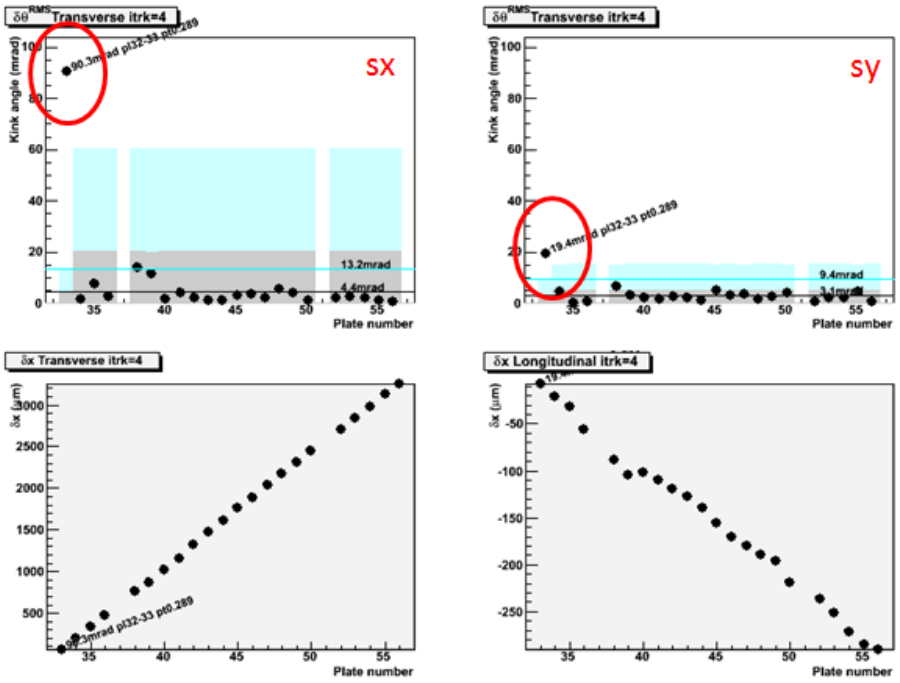

Figure 3.4: *Residual plots for track 6. Each figure shows the differences of angles (top) and positions (bottom) both in x (left) and y (right) views of each base-track with respect to the one found in the previous plate. The first plate points have deviations larger than any other belonging to the track and it clearly suggests the occurrence of a vertex. The black and cyan lines show the slopes residual variances, excluding or including the first point respectively. For x slopes, the variances are* 4.4 mrad *without the first point and* 13.2 mrad *including the first point. For y slopes, the variances are* 3.1 mrad *without the first point and* 9.4 mrad *including the first point. The colored bands are the* $5\,\sigma$ *regions considering the first point (cyan) or not (grey). As can be seen, the first point is always outside the cyan* $5\,\sigma$ *region while all the other points are always included in the grey* $5\,\sigma$ *bands.*

Table 3.4: *Parameters of the electromagnetic showers of the event.*

Shower ID	γ_1	γ_2
Starting plate	35	41
x (μm)	15271.0	14906.6
y (μm)	59647.0	60183.2
θ_x (rad)	0.050	-0.011
θ_y (rad)	0.122	0.085
$\mathrm{IP}_{\mathrm{III}}$ (μm)	8 ± 8	40 ± 11
IP_{I} (μm)	30 ± 22	40 ± 23
Opening angle (rad)	0.027	0.029

these two photons, the so-called gamma pointing accuracies were evaluated. This procedure estimates the errors associated to the IP using the mean direction of the shower first electron-positron pair with respect to the vertices. The results showed that EM shower 1 points to the kink point (vertex III), while EM shower 2 could come from any of the vertices (I, II or III). These two high energy photons can be explained by the presence of one or two π^0. The two π^0 hypothesis is highly disfavored because it would mean that two other high energy photons are not reconstructed. Then, the single π^0 case is assumed to be the most probable hypothesis and both photons are assumed to come from vertex III.

An extensive search for nuclear fragments was performed using the LASSO scanning system [75], which is able to detect fragments with $\tan\theta < 3$: no fragments have been detected at any of the three vertices.

The event has been cross-checked from scratch by a Japanese team, using the Japanese scanning system: the topology is fully confirmed.

3.2 Kinematic

The event topology is not the only information that can be retrieved from these measurements. Momenta of the reconstructed particles have also been studied.

3.2.1 Particle momentum

For tracks 1, 3, 5, and 6 the momentum was estimated using the multiple Coulomb scattering method. The method relies on the experimental angular resolution: this was evaluated, together with the position resolution, using a sub-dataset of penetrating tracks found in the event volume, including both event tracks and cosmic rays passing trough the brick. The resulting parameters are $3.4/\sqrt{2}$ mrad (angular resolution) and $0.8/\sqrt{2}\,\mu$m (position resolution). Furthermore, the basetracks used for the momentum evaluation

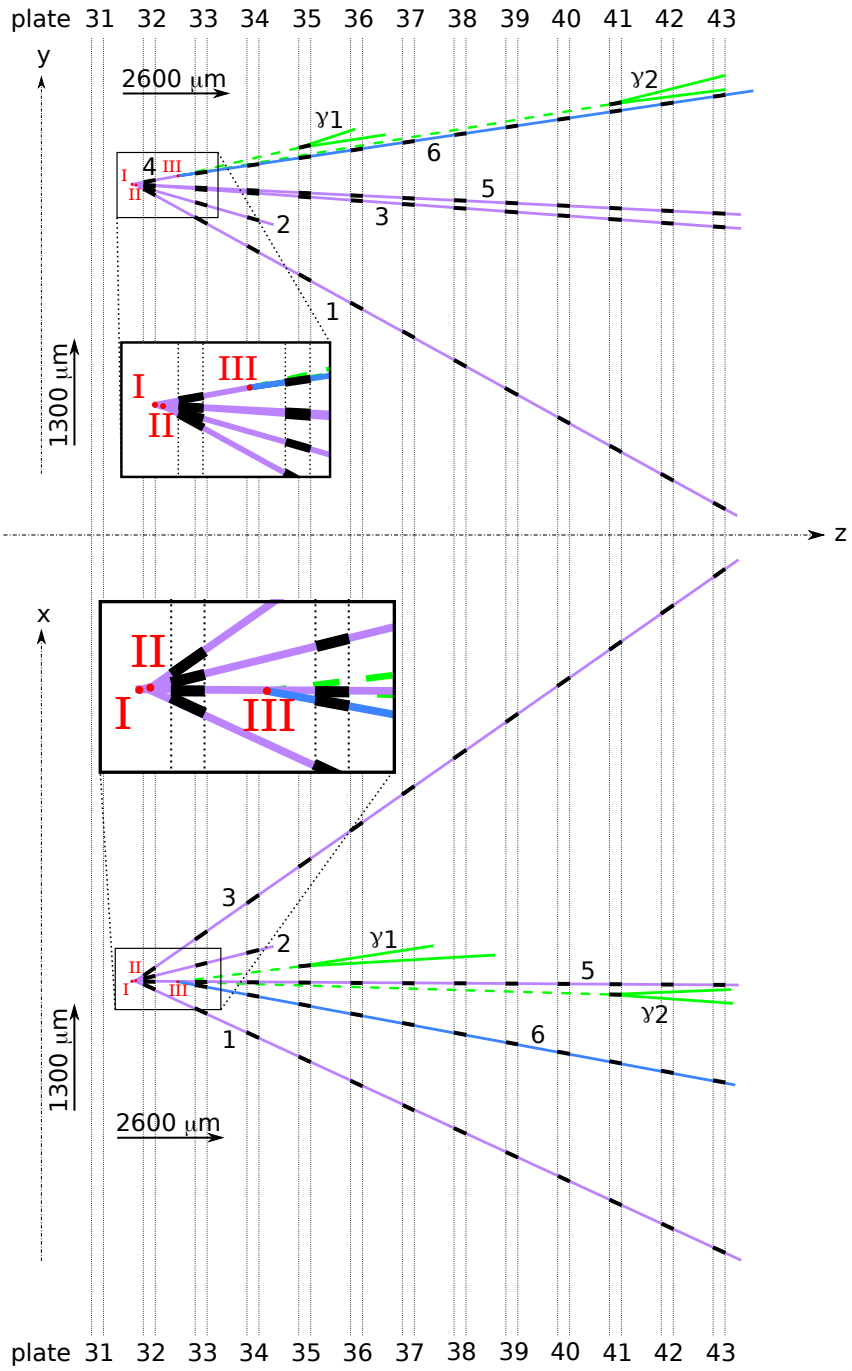

Figure 3.5: *Projection of the event in yz (up) and xz (down) planes. Base-tracks are represented in black, while reconstructed tracks are represented in purple lines, or blue for the daughter particle. In the xz view, the parent (track 4) is not visible since it is behind track 5. For photons, only the first base-tracks is reported.*

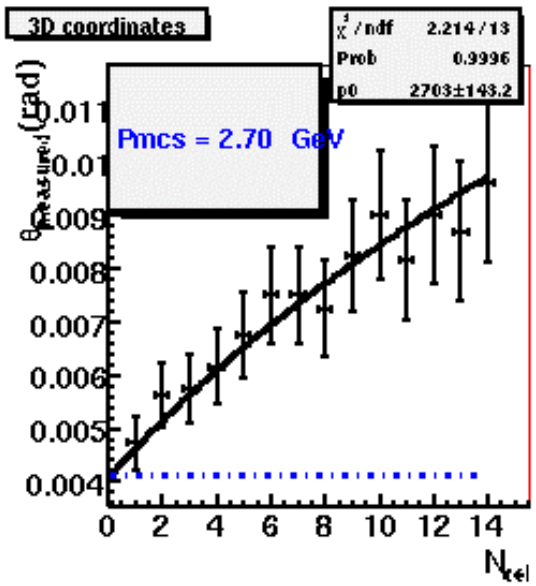

Figure 3.6: *Momentum fit for track 6, as described in Section 2.4.5. The fitted values are the θ variances as a function of cell size, N_{cell}, as in Figure 2.20.*

were corrected according this refined alignment. The momenta evaluated using this method are summarized in Table 3.5. The fit of the angular variances used for the momentum evaluation of track 6 can be seen in Figure 3.6.

Due to the small amount of base-tracks related to track 2, just three of them, its momentum had to be estimated using other methods. A rough estimation could be obtained by means of the stopping range in lead, as provided by the NIST [76]. This preliminary evaluation results in a momentum too low, which corresponds to $\beta < 0.5$, whatever is the assumed mass for particle 2. Values in that range do not match the energy deposit estimated by grain counting of the recorded base-tracks: such low β values would have implied a much higher energy deposit, namely a higher number of grains. A better approach could be achieved considering absorption processes. In particular, pions present a resonance at a kinetic energy of about 200 MeV, for every material [77]. The absorption increases with A and energy, though the energy dependence is suppressed at high atomic A [78]. In this region, especially for high A nuclei, the absorption cross section is up to ~ 40 % of the total cross section. From these arguments, the momentum estimation for track 2 is 0.31 ± 0.08 GeV/c. This is the initial momentum of a pion which is absorbed after crossing 2 mm of lead and that has kinetic energy of about 200 MeV when it is absorbed. The uncertainty is evaluated assuming a uniform kinetic energy distribution: the minimum the minimum is the kinetic energy such that that $\beta > 0.7$; while the maximum is 300 MeV, which is the

Table 3.5: *Particles momenta reconstructed by the multiple Coulomb scattering method.*

Track ID	p best fit (GeV/c)	68 % p range (GeV/c)
1	2.1	[1.6 ; 3.1]
3	4.3	[3.1 ; 7.1]
5	0.54	[0.45 ; 0.68]
6 (daughter)	2.7	[2.1 ; 3.7]

endpoint of the absorption peak.

3.2.2 Electromagnetic showers

In principle, using the emulsions, the energy of an EM shower could be reconstructed by counting the electrons produced by the shower. Anyway, such a measurement is not trivial, because it is difficult to distinguish between electrons coming from the shower and fog. Also, these two showers overlap, making the association of electrons to any of the showers very difficult.

Anyhow, attempts were made using alternatives strategies. The first energy estimation was done using the relation between the shower energy and the opening angles of the first e^+e^- pair. It suggested the showers are coming from high energy photons, both of them with energy greater than 1 GeV. Finally, a new method was developed for this estimation, based on the evaluation of the micro-tracks multiplicity inside the shower volume [79]. The results provided by this methods for these EM showers are: $E_1 = 7.2 \pm 1.7$ GeV and $E_2 = 6.0 \pm 2.0$ GeV, for γ_1 and γ_2 respectively.

3.3 Event interpretation

This interesting event was studied in detail and a complete topological and kinematic description was obtained. Both topology and kinematics were confirmed by independent measurements using the Japanese scanning system. Except for the ambiguity on the origin vertex of track 2, the topology is clear: this neutrino interaction contains two secondary vertices. One of them (III) is surely created by a primary charged particle (track 4). The other one (II) can be a 2-prong or a 3-prong vertex with a slightly preference for 2-prong. Indeed, it is clear that all the secondary vertices daughters are relatively high energy particle. The invariant masses of the reconstructed daughters for each of the two vertices can be seen in Table 3.6. As can be seen, the minimum invariant masses are significantly higher than invariant masses. That is an indication of the presence of other neutral particles that could be produced at both secondary vertexes.

The OPERA proposal considered negligible the observation probability of

Table 3.6: *Secondary vertices invariant masses and minimum invariant masses. Reported errors come from propagation of momenta errors. The differences are evaluated too, $\Delta \equiv M_{min} - M$. Due to the correlation between the two distributions, the errors are relatively small.*

Vertex ID	Invariant Mass M (GeV/c^2)	Minimum Invariant Mass M_{min} (GeV/c^2)	Difference Δ (GeV/c^2)
II	1.8 ± 0.5	2.5 ± 0.8	0.7 ± 0.4
III (kink)	1.3 ± 0.2	1.8 ± 0.4	0.5 ± 0.2

such a topology and no identification procedure was designed for this kind of event. At the same time, none of the primary vertex tracks can be classified as a tau according to the standard OPERA classification criteria. In fact, the kink matches all the selection criteria except for one, the daughter transverse momentum. In particular, since there are photons connected to the kink, the OPERA criteria require that the minimum daughter transverse momentum should be 300 MeV but the best fit value is just 242 MeV. The value is lower then the threshold, but if the errors are considered the measurement will be definitely compatible with the cut value. This interpretation is quite unsatisfactory, especially considering the relatively high energy of the daughters and the peculiar topology observed for this event.

3.3.1 Possible sources of two secondary vertices topology

In OPERA kinematic conditions, the prompt processes able to produce two very short decays ($\sim$ 1 mm) are just two: ν_τ CC interaction with associated charm production and ν NC interaction with $c\bar{c}$ pair production. The first one has never been observed, while the CHORUS experiment [80] observed three charm pairs produced in NC interactions. Figure 3.7 presents the leading Feynman diagrams for these two prompt processes.

Other possibilities to obtain such a signature require a re-interaction of a final state particle with the lead, or a short decay of a semi-stable particle (π, K) within few millimeters from the primary vertex. In this context, hadron re-interaction includes all the processes that are able to simulate a secondary vertex, hence large angle Coulomb scattering is also taken into account. The contributions coming from ν_μ CC interactions is reduced because the final state muon has to be misidentified or not reconstructed in order to mimic a neutral current like event. Finally, the interactions which can fake a two secondary vertices topology are:

- ν_τ CC interaction with one hadron re-interaction in which the produced τ is successfully reconstructed;
- ν NC interaction with two hadron re-interactions;

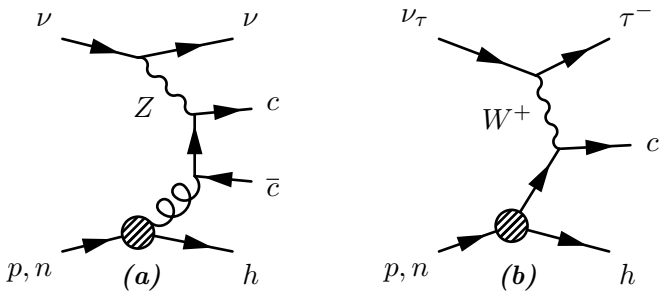

Figure 3.7: *Leading Feynman diagrams for the production of two prompt short decaying particles: (a) is the charm pair production in NC interaction and (b) is the tau charm production in CC interaction.*

- ν_μ CC interaction with single charm production, one hadron re-interaction and mis-identified muon;
- ν_μ CC interaction with two hadron re-interactions and mis-identified muon.

It has to be noticed that in the ν_μ CC contributions the re-interaction could be due to a mis-identified muon. In this case, an actual muon large angle Coulomb scattering is reconstructed as an hadron kink.

3.3.2 Analysis strategy

The analysis which was developed to identify the nature of this event is not based on the standard OPERA procedure. The main reason is that OPERA Monte Carlo is not able to simulated all the processes described in section 3.3.1. In fact, OPERA simulates only ν_τ CC interactions and ν_μ CC events with charm production. Also, the event selection is completely different and so are the variables used for the signal-background discrimination.

The main goal of the analysis is to assign the occurrence probability of the event as any of the processes listed in section 3.3.1. To do so, a very large number of events were simulated using different event generators. These events were propagated through a dedicated simulation for a few millimeters in an OPERA brick: this simulation selects events considering the OPERA emulsion's scanning acceptance and efficiency. The hadron re-interaction contribution is also evaluated by means of this dedicated simulation. Then, a search for this interesting topology is performed over all generated events and some distinctive variables are evaluated.

These MC events are used to train some refined classifying algorithms in order to distinguish interesting topologies from less intriguing hadron re-interactions. Once properly trained, the classifier's output variable is designed to be used to set a decision boundary: as the output increases, the more the event looks like a *signal*, whatever are the signal and the background

used used for the training. These output variable distributions, different for each source, can be used to evaluate the probability for the event of being each of all possible sources. This procedure was done blindly with respect to the value of the output variables for our interesting event in order to maximize the discrimination between the different possibilities and not the signal probability itself.

Chapter 4

Test beam analysis

Hadron re-interaction is a background source for the standard OPERA analysis. In order to control the hadron re-interaction estimation, some bricks were exposed to hadron beams and the hadron re-interactions were studied using the OPERA emulsions. These data were used to evaluated the hadron re-interaction probability and to estimated the background expected in the OPERA selection.

These data are very useful also for the interesting events analysis. In fact, the processes which can mimic a two short decaying particles event always involve at least one hadron re-interaction. Hence, this test beam was used to develop a reliable simulation based on GEANT4. The developed algorithms will be used to evaluate the hadron re-interaction contribution to events with two secondary vertexes.

This chapter presents the test beam setup and its dedicated simulation. The physics processes tested with this simulation are the same used for the simulations of the two secondary vertices event. A full description of the test beam can be found in [81].

4.1 Test beam description

The hadron interactions were studied in an ECC brick exposed to 2, 4, and 10 GeV/c hadron beams. The brick was exposed at the CERN PS-T7 beam line in May 2001. The brick was composed of 29 emulsion films (44 μm thick emulsion layers on both sides of a 205 μm thick plastic base) interleaved with 28 lead plates, 1 mm thick. The brick was 12.8 cm wide, 10.2 cm high, and 3.7 cm thick. It was put on a turntable and tilted in the horizontal plane by an angle with respect to the beam of $\pm$50 mrad as shown in Figure 4.1. Since the beam was exposed to both positive and negative beams, the tilt angle was used to distinguish between positive (+50 mrad) and negative (−50 mrad) charge.

The beams momentum spread, $\frac{\Delta p}{p}$, was 1 %. The negatively charged

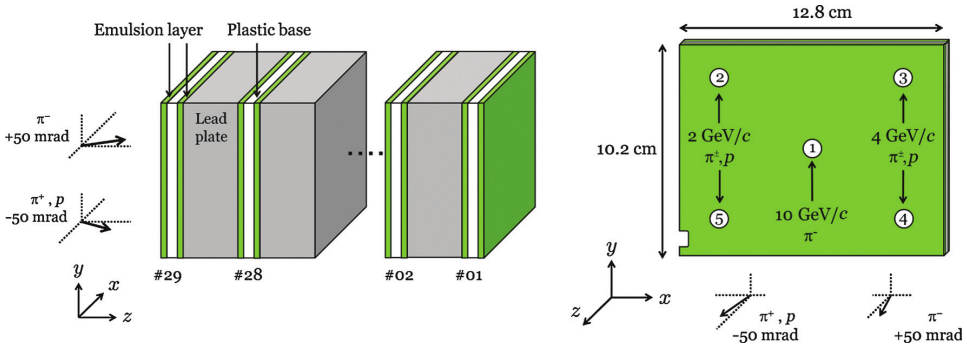

Figure 4.1: *Test beam ECC brick. Left: scheme of the ECC brick structure. Right beam spot positions on the ECC transverse plane.*

beams are mainly composed of pions with small contamination from electrons, while the positively charged beams contained both pions and protons with a small contamination of positrons.

In the original paper [81] a Monte Carlo simulation based on FLUKA3 [82, 83] was employed for comparison with data. In total, 30'000 negatively charged single pions MC events were generated for momentum values of 2, 4, and 10 GeV/c.

4.1.1 Scan system

After the brick development, the brick was analyzed using the Japanese scanning system, in particular the Super-UTS (S-UTS) [84]. This system allows the collection of large samples of beam particles tracks. These are followed down for a long distance and their interactions are measured too. In addition, a new type of automated emulsion scanning system [85] was developed in order to detect nuclear fragments emitted in a wide angular range.

4.1.2 Scanning procedure

The emulsion films has been scanned by using the S-UTS. Firstly, track segments, so called micro-tracks, were detected on each layer of every emulsion film. The positions (x, y) and slopes ($\tan\theta_x$, $\tan\theta_y$) of the micro-tracks were measured. The base tracks were reconstructed by connecting two corresponding micro-tracks across the plastic base. The S-UTS slope acceptance is $|\tan\theta| < 0.6$, where θ is the track angle with respect to the perpendicular of the emulsion film (the z axis). The track-finding efficiency, which is the probability of finding a base track in a film, was also measured. It was evaluated to be $94.8 \pm 0.2\%$, by examining whether a base track exists or not in the middle of five consecutive films.

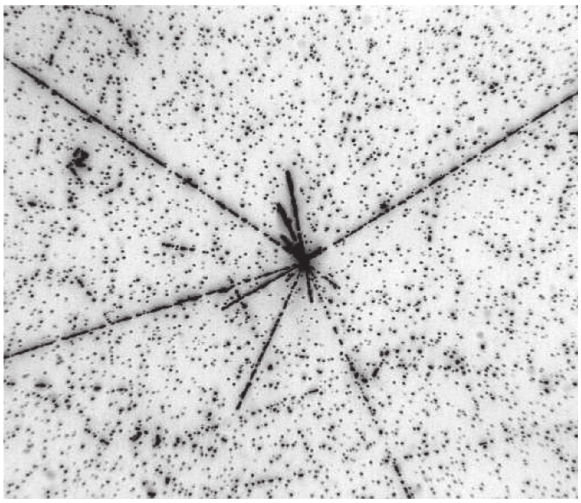

Figure 4.2: *Hadron interaction in an emulsion layer. Nuclear fragments are observed as black or gray tracks. Association of such highly ionizing particles is evidence of a hadron interaction.*

If a secondary particle has a value of $\beta < 0.7$, the particle will be observed as a heavily ionizing track and interpreted as nuclear fragment, as shown in Figure 4.2. Nuclear fragments emitted from hadron interactions were looked for by a newly developed automatic scanning system which has slopes acceptance is higher than the S-UTS, up to $|\tan\theta| < 3.0$. Since nuclear fragments are emitted almost isotropically, the new scanning system is suitable to detect them with good efficiency. The system has a large field of view, $352\,\mu\text{m} \times 282\,\mu\text{m}$, and has a track-finding efficiency of practically 100 % for nuclear fragments.

Each beam spot had a different number of emulsion plates scanned by the system. Namely, the hadron interaction were searched through a different thickness depending on the pion energy: 12 plates for 2 GeV pions, 11 plates for 4 GeV and 14 plates for 10 GeV.

4.2 Dedicated simulation

The simulation for the test beam presented in this work is a GEANT4 simulation [86, 87]. It is designed to fulfill the same criteria of the analysis for the event presented in Chapter 3: to be able to propagate every kind of particle through a portion of the OPERA brick. The physics processes implemented in the test beam simulation are the same which will be applied in the event simulation described in chapter 5. So, the conclusion obtained with this data comparison are valid also for the simulation about the two secondary vertex topology analysis.

The simulated volume has a transverse area of 10 cm × 10 cm. Along the longitudinal direction, the volume presents the same sandwich structure of the ECC brick, see Figure 4.1. The number of simulated plates varies according to the pion energy as described in section 4.1.2.

For each of the three possible pion energies, 30'000 π^- were generated and propagated along the brick one by one. This implies that the tracks overlap between events is impossible. Momenta are generated according to Gaussian distributions with $\frac{\sigma_p}{p} = 1\,\%$, thought this is ineffective from the point of view of the interaction probability.

4.2.1 Simulation engine

During particle propagation, several processes can occurs. In this energy regime, they are mostly electromagnetic processes which produce ionization electrons. These electrons are not useful from the point of view of the simulation, so their propagation is suppressed. Sometimes an hadronic process can occur. In this case, the particles coming from the interaction vertex are preliminary saved and propagated through the brick.

The emulsions are considered active materials. Whenever a charged particle crosses an emulsion, a selection is applied in order to determine whether the particle produces a detectable micro-track. This selection depends on the β of the crossing particle, as observed in previous sections. If the particle is in a relativistic regime ($\beta > 0.7$), the angular acceptance is $|\tan\theta| < 0.6$. The particle is also requested to have a momentum greater than 74 keV, which is the minimum required to cross two emulsion films. When such conditions are fulfilled, the track leaves a reconstructed basetrack. This reconstructed basetrack has the same position and slope if the crossing particle. If $\beta < 0.7$, the selection is different: the angular acceptance is $|\tan\theta| < 3$ while the minimum momentum is 14 MeV for an α particle. The momenta thresholds are scaled according to the Bethe-Block formula charge dependence, which has a dependence on Z^2.

Whenever a base-track is reconstructed, the tilt angle is compared to the one obtained from the previous emulsion layer, if available. If the tilt between the two is larger than 20 mrad and the track does not present any other tilt larger than the threshold in the following emulsions, a new track will be defined. A the same time, a new vertex is defined in the middle point of the minimum distance between the two base-tracks.

4.2.2 Results

The comparison between data and the GEANT4 simulation was performed on four different observables: interaction length, number of forward tracks, kink angle of 1 prong interactions and number of associated nuclear fragments.

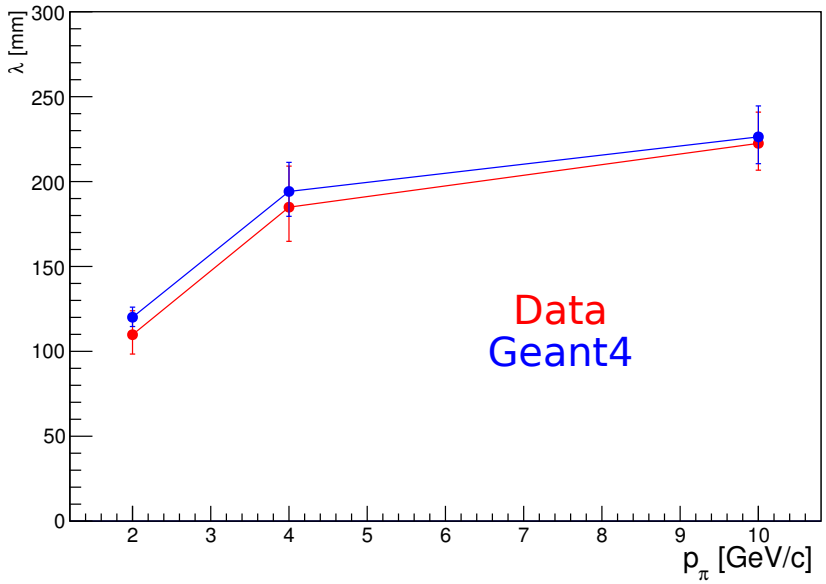

Figure 4.3: *Comparison between the interaction length evaluated from data and GEANT4 simulation. The reported errors are purely statistical.*

The interaction length, λ, is the quantity used to quantify the interaction probability of an hadron in a medium. In this specific case it is evaluated as

$$\lambda = -\frac{L}{\ln\left(1 - \frac{N}{N_0}\right)} \tag{4.1}$$

where N_0 is the number of tracks which was followed up, N is the number of located interactions out of the N_0 tracks and L is the length of the volume in which the interactions were counted. Usually, this quantity is almost constant with respect to the hadron energy. However, in this case, a Coulomb scattering angle bigger than 20 mrad is considered an interaction, therefore λ has a strong energy dependence, especially at low energies. As can be seen in Figure 4.3, data and MC are in very good agreement. The λ statistical error is evaluated assuming N to behave like a binomial distribution and propagating the variance through equation 4.1.

The number of forward track is the number of MIP ($\beta > 0.7$) associated to an interaction vertex which are emitted forward, namely $\cos\theta > 0$; the results can be seen in Figure 4.4. For 1-prong vertices, also the kink angle is evaluated, see Figure 4.5. The number of nuclear fragments is the number of black tracks ($\beta < 0.7$) associated to a 1-prong or 3-prong vertex, Figure 4.6.

For each of the latter three distributions, data are compared to both the GEANT4 and the original FLUKA simulations. The GEANT4 MC results are presented with both absolute and relative normalization. In absolute normalization, the expected spectra are normalized to the number of track

followed in the brick, N_0. In this case, also the error due to the statistics of the simulation is included. In relative normalization, the MC histogram area is normalized to data area in the same histogram. FLUKA simulation results are always presented with relative normalization as in the original study [81].

Table 4.1 presents data and MC comparison for some interaction topologies. Whenever the statics is high enough ($n > 10$) also a deviation is evaluated as

$$\delta_{sys} \equiv \frac{N_{obs} - N_{MC}}{N_{MC}} \tag{4.2}$$

In the original paper, using slightly different topological categories, the authors conclude that data are always within 30 % of the FLUKA MC predictions. The same argument can be applied to this simulation. GEANT4 results were found to be compatible with FLUKA expectations and, with respect to data, its δ_{sys} is lower than 30 %. Hence, a 30 % uncertainty is assumed for the GEANT4 hadron re-interactions results.

Table 4.1: *Data and Monte Carlos topology comparison for pions re-interactions. The reported GEANT4 errors depend on the statistic of the simulation.*

(a) *2 GeV*

	Data	GEANT4	δ_{sys}	FLUKA	δ_{sys}
N_0	584	30000	-	11301	-
λ (mm)	110^{+14}_{-11}	120^{+6}_{-5}	$-8\,\%$	124 ± 3	$-11\,\%$
Interactions	77	71 ± 3	$+8\,\%$	68	$+12\,\%$
1-prong event	33	46 ± 3	$-28\,\%$	41	$-19\,\%$
3-prong event	0	0.25 ± 0.20	-	0.13	-

(b) *4 GeV*

	Data	GEANT4	δ_{sys}	FLUKA	δ_{sys}
N_0	913	30000	-	9260	-
λ (mm)	185^{+24}_{-20}	194^{+17}_{-14}	$-5\,\%$	209^{+8}_{-7}	$-11\,\%$
Interactions	68	65 ± 5	$+5\,\%$	60	$+13\,\%$
1-prong event	29	32 ± 4	$-9\,\%$	29	$< 1\,\%$
3-prong event	2	3 ± 1	-	2.5	-

(c) *10 GeV*

	Data	GEANT4	δ_{sys}	FLUKA	δ_{sys}
N_0	2205	30000	-	13746	-
λ (mm)	223^{+18}_{-16}	226^{+18}_{-16}	$-1.3\,\%$	231 ± 7	$-3.5\,\%$
Interactions	173	170 ± 12	$+1.7\,\%$	166	$+4.2\,\%$
1-prong event	26	30 ± 5	$-13\,\%$	34.6	$-25\,\%$
3-prong event	44	39 ± 6	$+13\,\%$	39.5	$+11\,\%$

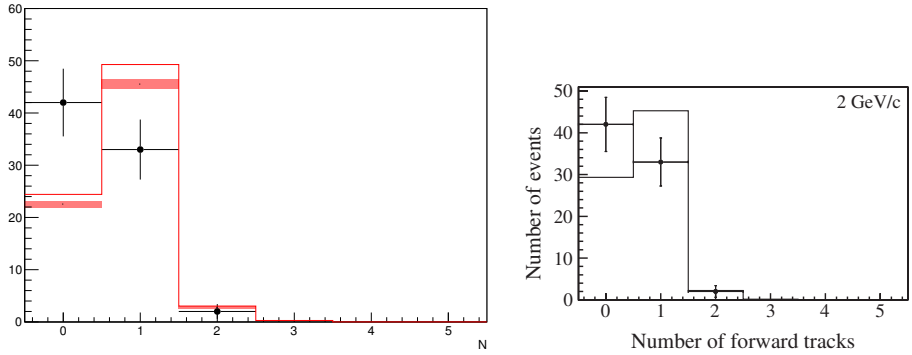

(a) *2 GeV*

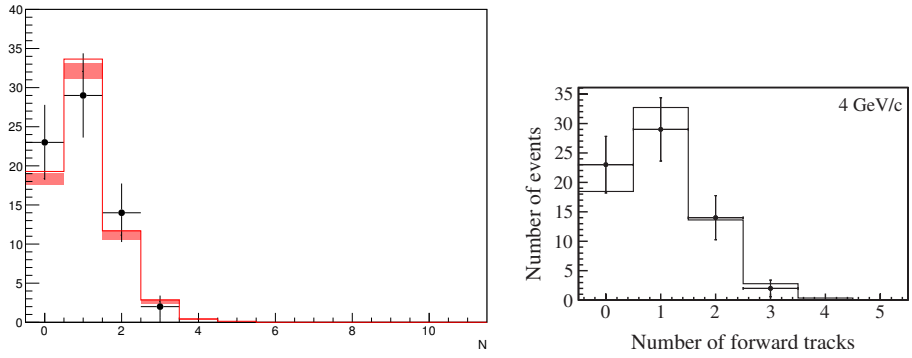

(b) *4 GeV*

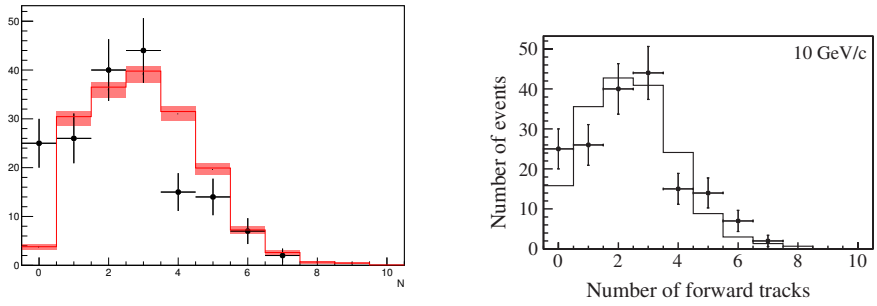

(c) *10 GeV*

Figure 4.4: *Number of reconstructed MIP from an interaction vertex. Left: data (black) GEANT4 - absolute normalization (red rectangles) and GEANT4 - relative normalization (red line). Right: data (black crosses) and FLUKA simulation (black line). The results are reported for different initial pion energies.*

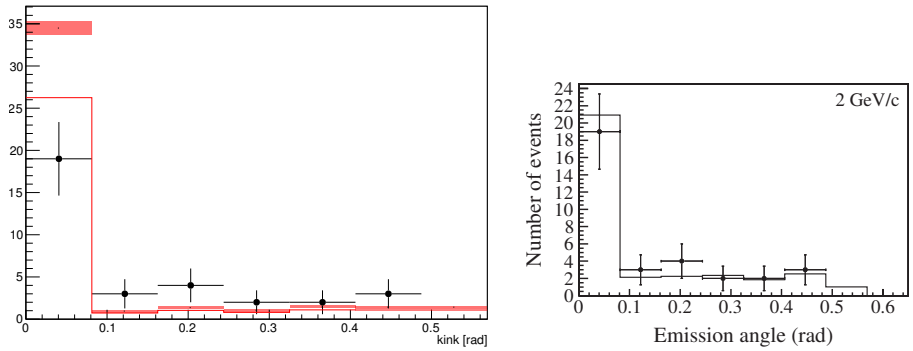

(a) 2 GeV

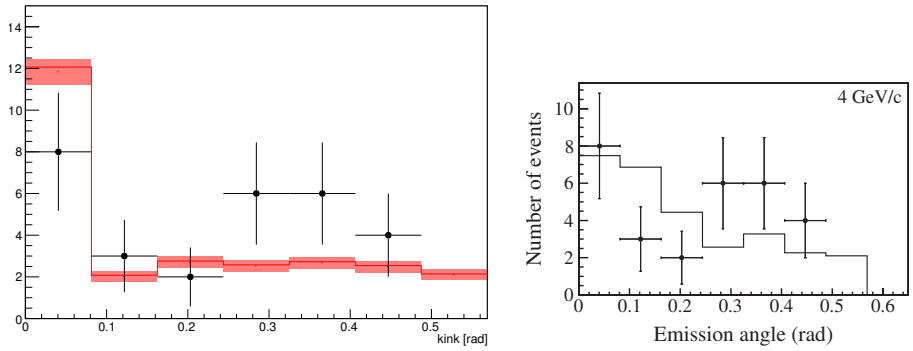

(b) 4 GeV

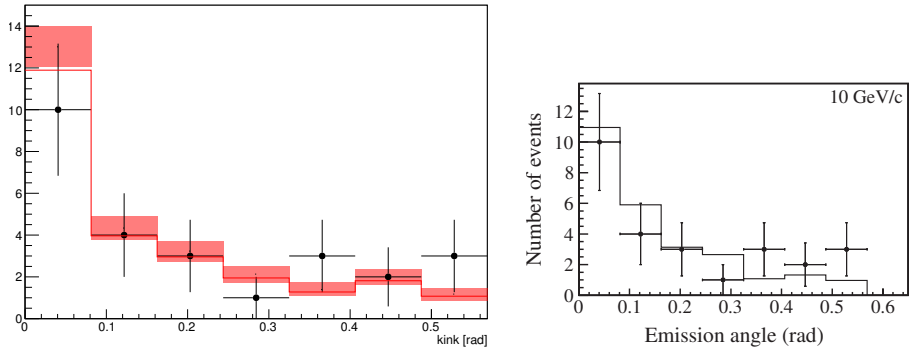

(c)

Figure 4.5: *Kink angle for one prong interaction vertices; nuclear fragments are not taken into account. Left: data (black), GEANT4 - absolute normalization (red rectangles) and GEANT4 - relative normalization (red line). Right: data (black crosses) and FLUKA simulation (black line). The results are reported for different initial pion energies.*

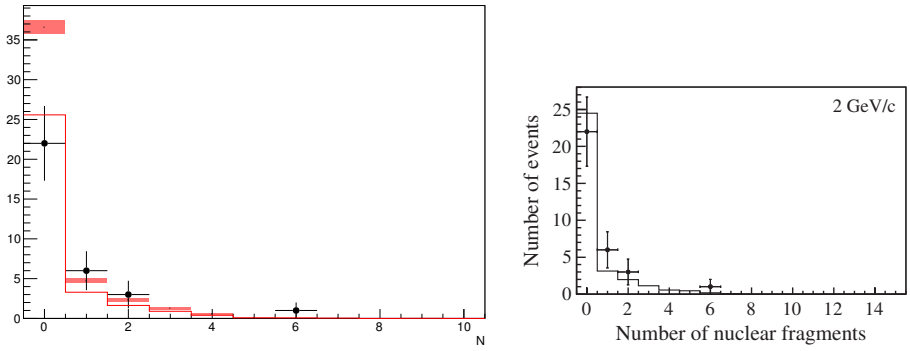

***(a)** 2 GeV*

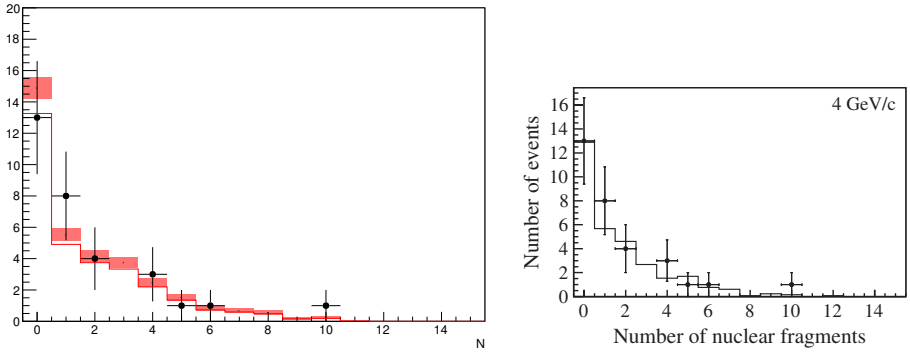

***(b)** 4 GeV*

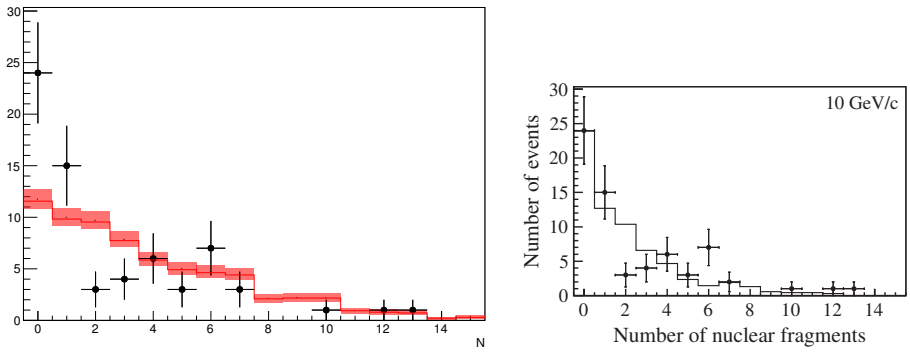

***(c)** 10 GeV*

Figure 4.6: *Number of observed nuclear fragments coming from an interaction. Left: data (black) GEANT4 - absolute normalization (red rectangles) and GEANT4 - relative normalization (red line). Right: data (black crosses) and FLUKA simulation (black line). The results are reported for different initial pion energies.*

Chapter 5

Dedicated Monte Carlo production

In order to evaluate the nature of the observed event, a dedicated Monte Carlo (MC) simulation was required. Its goal is a quantitative description of the events which can be observed in the OPERA experiment with a topology similar to the one described in chapter 3. This topology allows the definition of several kinematic variables which characterize the events. These variable will be used as a starting point for a multivariate analysis in order to identify the event's nature.

This chapter describes procedures and tools used to obtain the MC sample and define some discrimination variables which characterize events with the topology described in chapter 3.

5.1 Production overview

As discussed in section 3.3.1, the processes to be considered are

- ν_μ CC DIS interaction;
- ν_μ CC DIS interaction with charm production;
- ν NC DIS interaction;
- ν NC DIS interaction with charm pair production;
- ν_τ CC DIS interaction;
- ν_τ CC DIS interaction with charm production.

For each of them the simulation chain is the same. First of all, Monte Carlo (MC) generators are used to produce particles at the primary vertex in lead. After this stage, the output consists of several ASCII files in the HEPEVT

format [88]. These also have special headers which summarize simulation details, e.g. cross section.

Not all MC generators can generate events according to a given neutrino flux, hence the events are simulated at fixed energies:

- up to 45 GeV in 1 GeV steps, with a lower bound which depends on the process threshold;
- from 48 GeV up to 153 GeV in 5 GeV steps.

For each energy there can be several sub-processes, for example some generators distinguish between neutrino interaction on proton or neutron.

The second step is the propagation of particles coming from the primary vertex through a dedicated simulation of a portion of an OPERA brick. The simulation is used to select tracks within the acceptance of OPERA emulsions and to evaluate their subsequent re-interaction probability. In the end, only events with at least one reconstructed decay or interaction are preserved. The output is once again a set of HEPEVT formatted files with similar headers.

The propagated files are converted into ROOT [89] files, encoded into a suitable data model format. Then, the files are analyzed in order to select events with two secondary vertices. At the same time, effects due to detector reconstruction are applied.

5.1.1 Neutrino fluxes

Only the ν_μ flux is considered since all other flavours are totally negligible for this analysis, see Figure 2.3. This spectrum is non oscillated, so it is used for the NC processes and it is called $\phi(\nu, E)$. Oscillations are taken into account and the oscillation probability is evaluated with effective formulas [90]. Then the used fluxes are:

$$\begin{aligned} \phi(\nu_\tau; E) &= \phi(\nu; E)\, \mathscr{P}_{\mu\to\tau}(E, L) \\ &= \phi(\nu; E) \cos^4\theta_{13} \sin^2(2\theta_{23}) \sin^2\left(\frac{\Delta m^2_{31} L}{4E}\right) \qquad (5.1) \\ \phi(\nu_\mu; E) &= \phi(\nu; E)\,(1 - \mathscr{P}_{\mu\to\tau}(E, L)) \qquad (5.2) \end{aligned}$$

where θ_{13}, θ_{23} and Δm_{31} are taken from the PDG [34]. Due to generation at fixed energies, the fluxes are integrated:

$$\Phi(i, \varepsilon) \equiv \int_{\varepsilon-\frac{\Delta}{2}}^{\varepsilon+\frac{\Delta}{2}} dE\, \phi(i; E)\,, \qquad (5.3)$$

where the bin width, Δ, is 1 or 5 GeV, depending on the energy, as described in section 5.1. Figure 5.1 shows the $\Phi(i, \varepsilon)$.

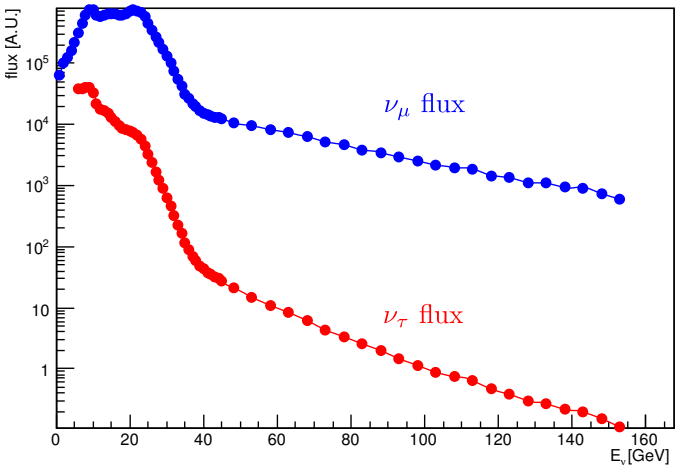

Figure 5.1: *Neutrino fluxes used for the analysis, as defined in equation 5.3. ν_μ oscillated flux is very close to ν one and they can not be distinguished in this scale.*

5.1.2 MC events weights

Starting from neutrino fluxes and cross sections, a weight is assigned to each event at the generator level. These are used to evaluated the number of expected events from each process.

The number of expected events with a certain final state, f, can be written as

$$N(f) \equiv k \sum_i \int dE\, \phi(i;E)\, \sigma(i \to f;E) \tag{5.4}$$

$$\simeq k \sum_i \sum_{\varepsilon \in E(i)} \Phi(i,\varepsilon)\, \sigma(i \to f;\varepsilon) \tag{5.5}$$

where k is a constant. k depends on the detector, the data taking period, the luminosity, but not on the final (nor initial) state. $\sigma(i \to f;\varepsilon)$ is the cross section of the process $i \to f$ evaluated at the fixed energy ε. All the fluxes are evaluated at LNGS.

The k value can be determined choosing a normalization process, labeled $i_N \to f_N$. Finally, the number of expected events from process $i \to f$ at a neutrino energy e is given by

$$N(i,f,e) = \frac{\Phi(i,e)\, \sigma(i \to f;e)}{\sum_\varepsilon \Phi(i_N,\varepsilon)\, \sigma(i_N \to f_N;\varepsilon)} N(f_N) \tag{5.6}$$

where $N(f_N)$ is the observed event number in the normalization channel.

The normalization is performed using ν_μ Charge Current (CC) interactions with neutrino energy higher than 10 GeV. In fact, their high momentum muons

are easy to reconstruct in the OPERA detector: the reconstruction efficiency is better than 95 % [63]. The total number of CC events reconstructed in the target volume is $N_C = 12352$. The fraction of events having neutrino energy greater than 10 GeV was extracted from the standard OPERA MC: $f_{10} = 0.900 \pm 0.003$. Finally, the number used for normalization is

$$N(f_N) = \int_{10\,GeV}^{+\infty} d\varepsilon\, N(i_N, f_N, \varepsilon) = N_C \cdot f_{10} = 11117 \pm 37 \tag{5.7}$$

Once the events number of the normalization sample is known, the expected events from all the processes can be evaluated, according to equation 5.6. The event weight associated to each event is then

$$w(i, f, e) \equiv \frac{N(i, f, e)}{n(i, f, e)} \tag{5.8}$$

where $n(i, f, e)$ is the number of simulated events for the process $i \to f$ at energy e.

5.1.3 Expected events in sub-samples

Once a sample, s, having certain properties is defined, the number of expected events with those properties is given by

$$N_s = \sum_{j \in s} w_j \tag{5.9}$$

$$= \sum_{i \in I} \sum_{f \in F(i)} \sum_{e \in E(i,f)} \sum_{j \in s(i,f,e)} w_j \tag{5.10}$$

Equation 5.10 shows the explicit form of the calculation on initial states (I), final states (F) and energies (E). The statistical uncertainty of the MC prediction is given by

$$\sigma^2_{N_s} = \sum_{j \in s} w_j^2 \tag{5.11}$$

5.2 Generators

Several events generators were considered for this analysis: Genie 2.8.0 [91], Herwig 6.521 [92] and Pythia 6.4 [93]. Genie is used as a benchmark due to its specificity for neutrino processes, anyway other solutions were studied. In fact, NC interactions with charm pair production are available only with Herwig. Furthermore, the usage of multiple generators is potentially interesting for systematic uncertainty studies, especially for rare processes such as the ν_τ CC interactions.

The ν_τ CC with charm production cross section as a function of the incoming neutrino energy can be seen in Figure 5.2 for all the generators.

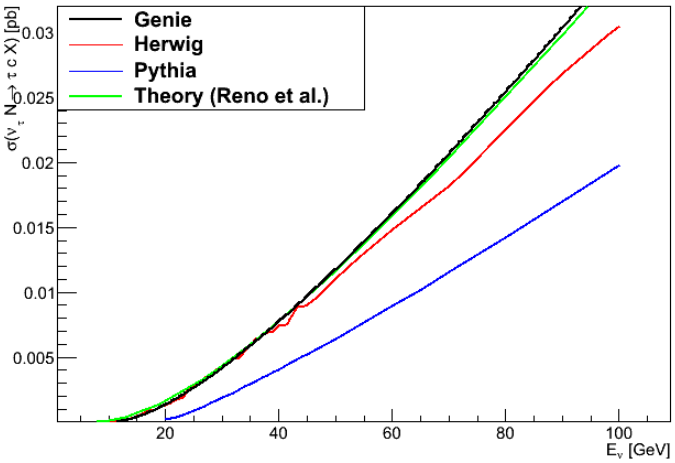

Figure 5.2: *Isoscalar cross sections for ν_τ CC DIS interaction with charm production as a function of the incident neutrino energy. The theory plot by Reno is obtained from [94].*

The Pythia generator sets the threshold for this process at rather high energies. Attempts to change some of the tuning parameters were made, without success. Therefore, Pythia was not trusted in this energy regime and was discarded.

Herwig predictions are also different from Genie's ones, anyway the discrepancies are in a region with a very small flux. Hence, their impact on the final results is small.

5.2.1 Genie

The Genie generator is able to produce all the processes interesting for the analysis, except the NC interaction with charm pair production. Also, Genie is able to generate events on nuclei, including final state interactions inside the nucleus. This effect turned out to be a 5 % effect on the cross sections, see Figure 5.3. For all Genie's productions, the events were generated on the lead isotopic composition described in Table 5.1.

Genie was used to produced all the processes listed in section 5.1 except for the ν NC DIS with charm pair production. The Genie ν_μ CC total cross section is the one used for the normalization channel.

5.2.2 Herwig

In principle, the Herwig generator should be able to simulate every neutrino interaction leading process. That's why it had been considered for the NC interaction with charm pair production and to cross check ν_τ CC interactions

Table 5.1: *Lead isotopic composition used for Genie's productions and cross section evaluation. The values are from [95].*

Isotope	Relative abundance
^{204}Pb	1.4 %
^{206}Pb	24.1 %
^{207}Pb	22.4 %
^{208}Pb	52.4 %

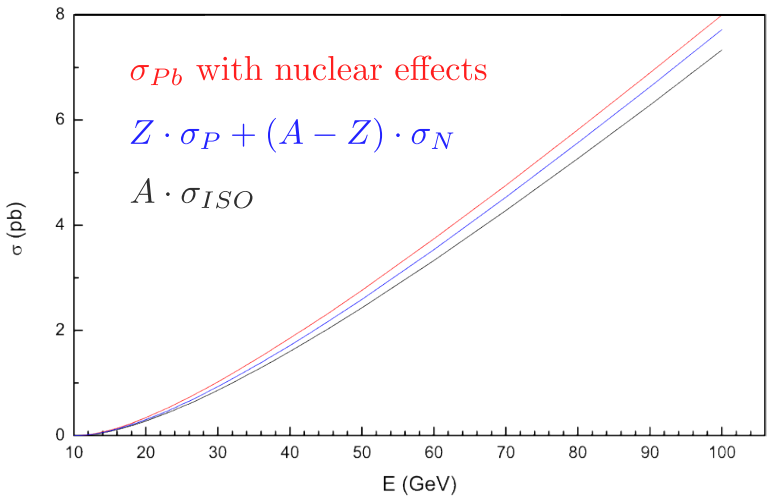

Figure 5.3: *Nuclear effect on ν_τ CC DIS cross section with charm production.*

Table 5.2: *Simulated events and expected produced events in the detector. The reported errors are purely statistical.*

process	total MC events	Expected events
ν_μ CC DIS	71 M	10 k
ν_μ CC DIS + charm	31 M	425 ± 1
ν NC DIS	113 M	3 k
ν NC DIS + $c\bar{c}$ pair	6.3 M	0.293 ± 0.001
ν_τ CC DIS	14 M	43.3 ± 0.1
ν_τ CC DIS + charm	3.2 M	1.067 ± 0.004

from Genie. Eventually, Herwig presented a huge discrepancy with respect to Genie and also Pythia. The difference was found in the transverse angle distribution between the outgoing tau and charmed meson: the two particles are emitted nearly always back to back, see Figure 5.4. The same peak was found also in ν_μ CC interactions with charm production, which is clearly in contrast with data, as can be seen in Figure 2.22b.

Herwig experts were contacted: they suggest to change the minimum transferred momentum Q^2_{min}, which is one the simulation parameters. Though Q^2_{min} was varied within an order of magnitude, the peak did not disappear and Herwig was not used for ν_τ CC the generation.

Eventually, Herwig was used only to provide the ν NC DIS with charm pair production on proton and neutron. The cross section on lead was obtained scaling the nucleon cross sections according to

$$\sigma_{Pb} = Z_{Pb} \cdot \sigma_p + (A_{Pb} - Z_{Pb}) \cdot \sigma_n \tag{5.12}$$

where σ_p and σ_n are the cross sections on proton and neutron, respectively.

5.2.3 MC samples

The simulated samples have different sizes, depending on the probability for each process to generate the topology described in Chapter 3. Processes like ν_τ CC do not require a huge amounts of events since they naturally produce at least one secondary vertex. On the contrary, events like ν_μ CC interactions are very unlikely to produce two secondary vertices within few millimeters from the primary one. But, at the same time, these are abundantly produced in the OPERA experiment, therefore very low probabilities have to be studied through an extensive MC production. Table 5.2 summarizes the produced samples.

Neutrino fluxes are peaked around 20 GeV, so the production is focused in the range between 10 and 40 GeV, see Figure 5.5. Events with neutrino energy below 10 GeV are difficult to locate inside the detector and are also suppressed by cross sections. The higher part of the spectrum is important

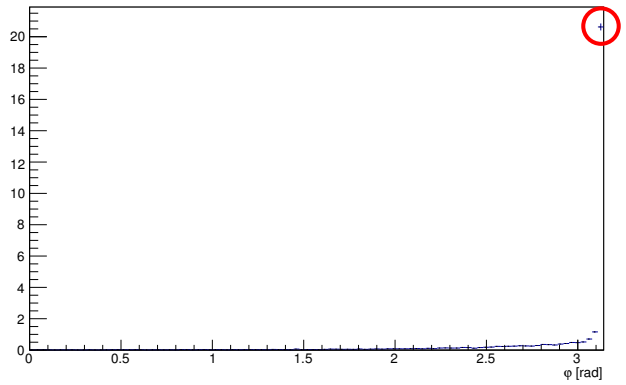

(a) *Herwig*

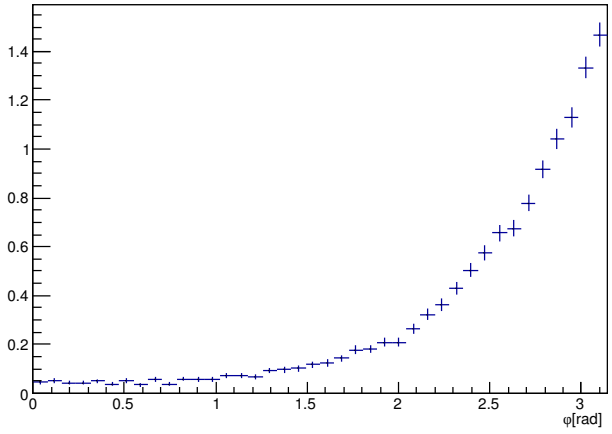

(b) *Genie*

Figure 5.4: *Transverse angle between tau and charm generated from Herwig (a) and Genie (b) in ν_τ CC interactions. The red circle points out the events peak at $\varphi = \pi$. Both graphs were obtained starting from 20 GeV ν_τ.*

for NC interactions with charm pair production. In fact, due to the cross section rapid growth with energy, the product $\phi(\varepsilon) \cdot \sigma(\varepsilon)$ for such events increases up to about 90 GeV, see Figure 5.6. As a cross check, the high energy tail of the CNGS beam is considered in every process.

5.3 Particle propagation

At this step, the generated events are propagated in time in order to evaluate which particle can be seen through an emulsion layer and to simulate the hadrons re-interactions with brick media. The software is based on the analysis developed for the test brick presented in chapter 4. There are few changes due to the different physic case.

The simulated geometry changed a bit: 15 plates are simulated. The primary vertices are set to a specific point between plates 5 and 6: in this way there are 5 emulsion layer to detect back-scattered tracks and 10 to detect forward going tracks. This point is placed in the center of the volume, with respect to the x and y axes, while the depth in lead is the same as in our event: the vertex is 581.8 μm upstream with respect to the vertex plate, namely plate 6 in the simulated brick.

The propagation, as all the analysis, is performed in the beam reference frame. This was measured in the OPERA experiment using the muons emission angle distribution from ν_μ CC interactions. As measured in [96], the beam angles with respect to the z axis are:

$$\theta_x = -6.8 \pm 0.3 \text{ rad} \quad (5.13)$$

$$\theta_y = 58.1 \pm 0.3 \text{ rad} \quad (5.14)$$

The geometry is suitably rotated to reproduced this effect.

With respect to chapter 4, another adjustment was applied to the angular acceptance of the emulsion. In the OPERA experiment it is common practice to perform manual checks, which were not performed on the brick exposed to the test beam. Under this condition, the angular acceptance increases up to $|\tan\theta| < 1$.

The only particles which are not propagated through the volume are very short decaying particles, namely tau and charmed hadrons. These particles are decayed by the generator itself as if they propagated in vacuum. During the transport, only the daughters are evolved, starting from the position provided by the generator with respect to the primary vertex. This corresponds to neglecting the re-interaction probability of charmed particles and taus in the lead. In these cases, the parent is considered visible if its daughters are visible.

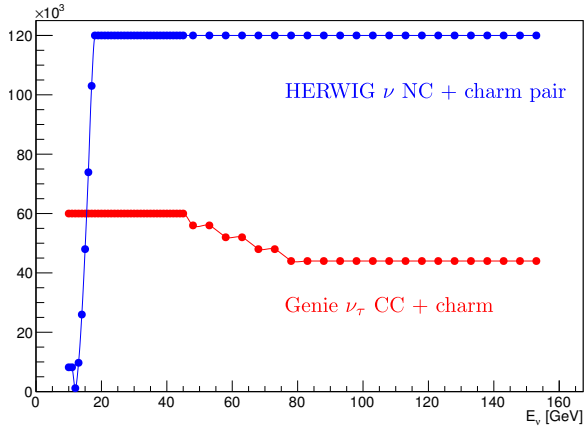

(a) Two prompt secondary vertices processes

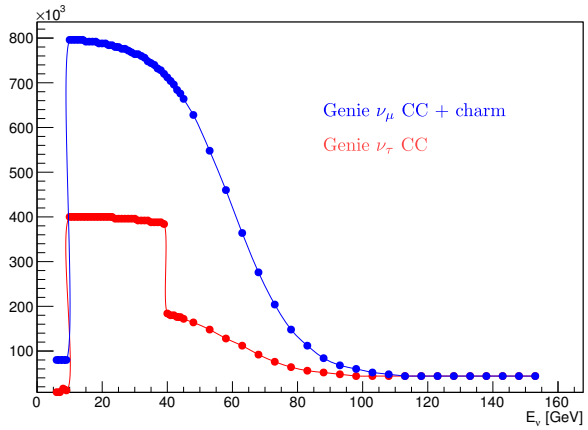

(b) One prompt secondary vertex processes

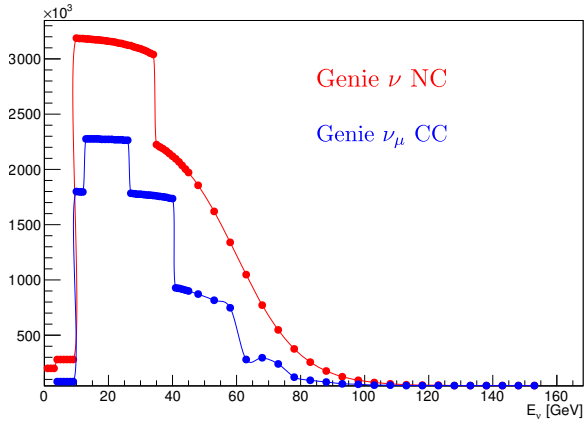

(c) No prompt secondary vertex processes

Figure 5.5: *Number of events produced at the generator stage for each process at different energies.*

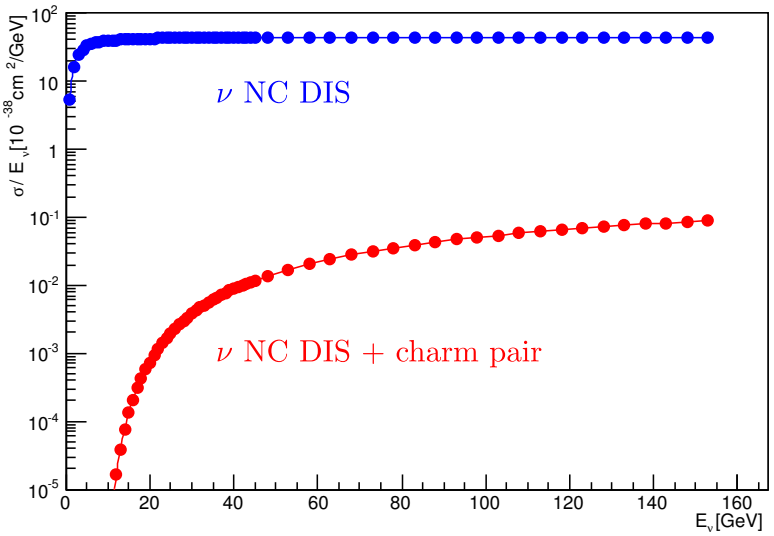

(a) $\sigma(E_\nu)/E_\nu$ *on lead*

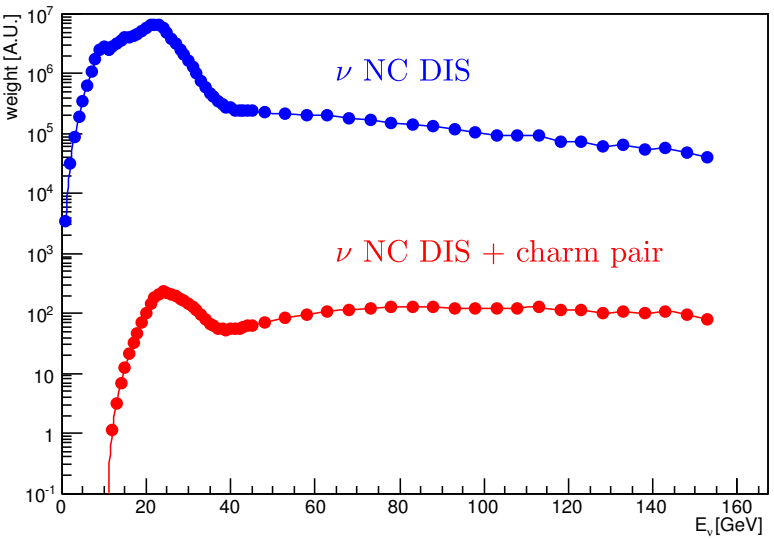

(b) $\phi(\nu, E_\nu) \cdot \sigma(E_\nu)$

Figure 5.6: *Comparison between NC productions properties as a function of the incoming neutrino energy.*

5.4 Detector effects

The simulation described in section 5.3 performs propagation through just few cubic centimeters, in order to evaluate the hadron re-interaction contribution. Anyway, the OPERA experiment is much more complex and a proper event reconstruction depends on the whole detector. These effects can be grouped in three categories: muon reconstruction, location efficiency and momentum resolution.

5.4.1 Muon reconstruction

In OPERA, electronic detector reconstructs muons using the event length, as in this energy regime muons look like very long tracks that cross the detector. In particular, an event is considered a CC event if the event activity crosses is present in at least 15 TT walls.

In order to include the muon reconstruction efficiency in the simulation, a muons sample was generated using the standard OPERA MC. All the muons were generated from the brick containing the event. The reconstruction efficiency was estimated starting from this sample, using a parameterization. Muons were generated varying energy and direction: the muon momentum varies between 0.2 GeV to 40 GeV with a linear decreasing distribution, while θ and ϕ distributions are uniform within $[0; \frac{\pi}{2}]$ and $[0; 2\pi]$, respectively.

The muon reconstruction efficiency ε_μ is the ratio between the number of muons actually classified as muons, N_μ and the total number of produced muons, n_μ. This was evaluated as a function of momentum and angular variables:

$$\varepsilon_\mu(p, \theta, \varphi) \equiv \frac{N_\mu(p, \theta, \varphi)}{n_\mu(p, \theta, \varphi)} \, , \tag{5.15}$$

see Figure 5.7.

The plots show clearly that the reconstruction efficiency has a momentum dependence: low energy muons have not sufficient boost to cross enough material, whatever is their direction. In the (θ, ϕ) plane, the efficiency behaves like a "cliff" due to the angular acceptance of the detector. Because of these observations, the muon reconstruction efficiency was assumed to behave as

$$\varepsilon_\mu(p, \theta, \varphi) = \varepsilon_p(p) \cdot \varepsilon_\Omega(\theta, \varphi) \tag{5.16}$$

where ε_p and ε_Ω can not be estimated from Figure 5.7. In fact, the momentum plateau value is about 60 % just because of the angular acceptance. In order to avoid these double counting effects, ε_p was estimated from muon produced with (θ, φ) contained in a box given by $\theta \in \left[0, \frac{\pi}{6}\right]$ and $\varphi \in \left[\frac{\pi}{2}, \frac{3}{2}\pi\right]$. At the same time, ε_Ω was estimated using only muon with momentum grater than 10 GeV. The results for ε_p and ε_Ω can be seen in Figure 5.8. The factor ε_p

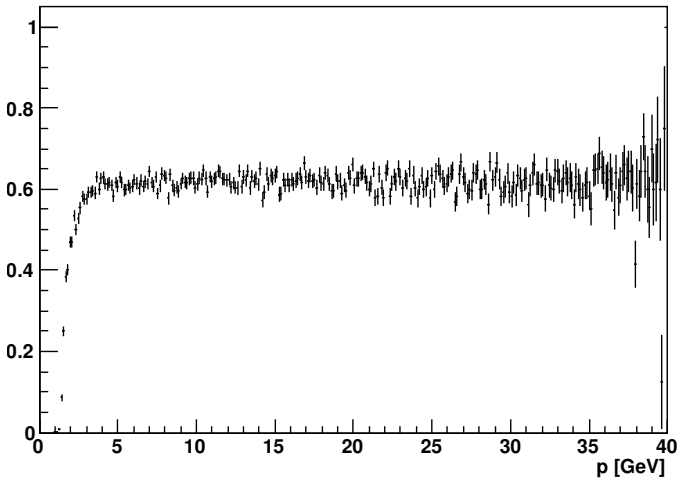

(a) Momentum dependency

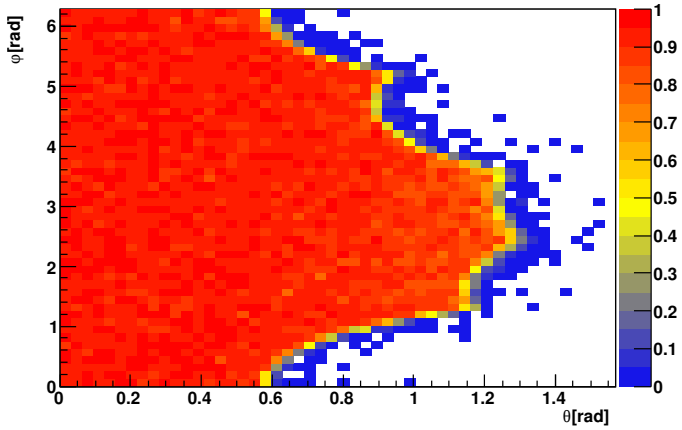

(b) Emission angle dependency

Figure 5.7: *Overall muon reconstruction efficiency as a function of muon momentum and emission angles.*

Table 5.3: *Fit results for ε_p function displayed in Figure 5.8a. Parameters are defined in equation 5.17.*

ε_0	1.00 (fixed)
p_0	1.47 ± 0.09 GeV/c
m	0.066 ± 0.038 GeV/c

was fitted with a step function, which has analytic form

$$\varepsilon_p(p) = \frac{\varepsilon_0}{1 + \exp\left(\frac{p_0 - p}{m}\right)} \,. \tag{5.17}$$

These results were applied to the event dedicated simulation. Whenever a muon was found in the simulation, the reconstruction efficiency was evaluated starting from its momentum, θ and φ. Then, a random number was generated with a uniform distribution in the $[0, 1]$ range. If the random number was greater than $\varepsilon_\mu(p, \theta, \varphi)$ the muon would be considered misidentified and treated as a pion in the event selection process.

5.4.2 Location efficiency

The location efficiency is the combination of two different steps: the correct identification of the brick containing the neutrino interaction and the actual localization of the primary vertex inside the brick. All these efficiencies were evaluated on data, namely on event with no secondary vertices. Their presence is not supposed to change the overall location efficiency since it depends on the tracks that exit the brick, not on the local topology.

Both contributions were parameterized starting from OPERA data set as a function of the hadronic energy released in the detector:

$$E_{had} = y \cdot E_\nu \tag{5.18}$$

where y is the Bjorken's variable and E_ν is the incoming neutrino energy. In data, the hadronic energy is evaluated using the algorithm presented in [63]. This computes the hadronic energy starting from the amount of energy recorded by the TT scintillators, labeled E_{TT}.

In the dedicated MC simulation, the TT is not even present, instead, the true hadronic energy is used with some corrections as in the following. For NC and ν_μ CC samples the computation is actually the true hadronic energy defined in equation 5.18. On ν_τ CC samples, the hadronic energy is evaluated as

$$E_{had} = E_\nu^{in} - E_\nu^{out} \tag{5.19}$$

where E_ν^{in} is the incoming neutrino energy and E_ν^{out} is the energy of the neutrino emitted by tau decay. This corresponds to assume that the hadronic energy in a ν_τ CC interaction is the total energy deposit in the detector. In

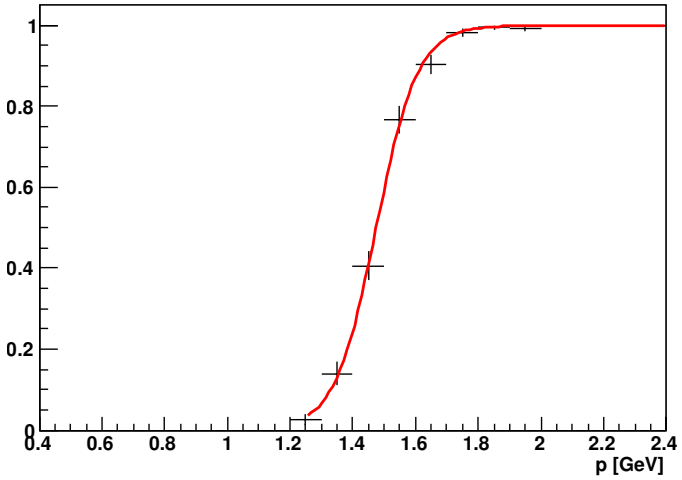

(a) *$\varepsilon_p(p)$ zoom around the step*

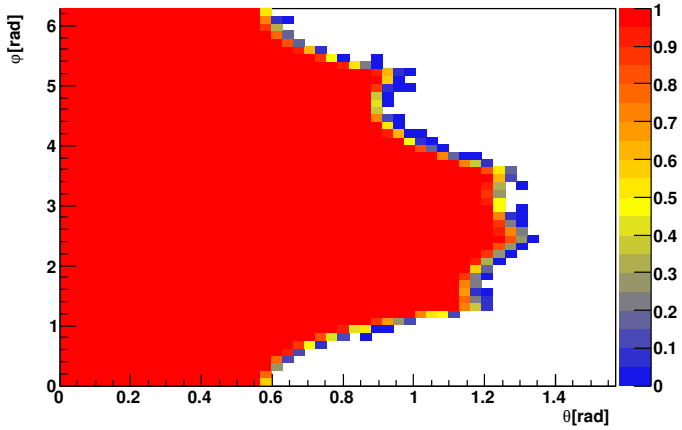

(b) *$\varepsilon_\Omega(\theta, \varphi)$*

Figure 5.8: *Muon reconstruction efficiency factors. The fitted function in (a) is defined in equation 5.17 and its fit results are summarized in Table 5.3.*

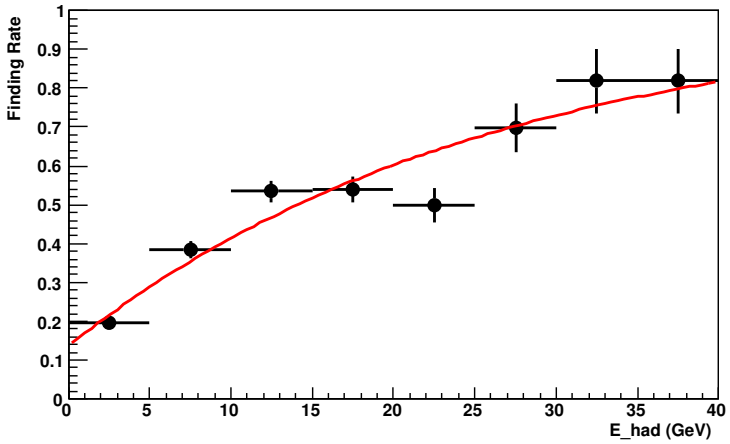

Figure 5.9: *Brick finding efficiency as a function of the hadronic energy. The fitted curve in is defined in equation 5.20 and the results are in Table 5.4.*

Table 5.4: *Brick finding efficiency best fit results. The parameters are defined in equation 5.20 and data comparison can be seen in Figure 5.9.*

ε_0	1
E_0	3.8 GeV
m	26 GeV

fact, tau decay products are mostly hadrons and so they behave in the detector. Hence, the OPERA reconstruction algorithm includes their contribution in the hadronic energy evaluation.

The data used for the brick finding efficiency evaluation are from the whole OPERA run and were provided by the CS scanning group of LNGS, see Figure 5.9.

The data used for the location efficiency were retrieved from the OPERA database. In this case the efficiency was evaluated on the 2010 – 2012 data sample, which has different selection criteria with respect to the 2008 – 2009 one. The efficiency is defined as the ratio between the events in which the decay search could be completed and the events with an hint in the CS doublet. As a cross check, the result is compared with the location efficiency published in [74], Figure 5.10a: as can be seen, the agreement is quite good. The same efficiency can be seen in Figure 5.10b, as a function of the hadronic energy.

The hadronic energy dependency of brick finding efficiency, ε_{BF}, and location efficiency, ε_{loc}, was fitted with saturating curves, whose analytic form is

$$\varepsilon(E_{had}) = \varepsilon_0 \left[1 - \exp\left(\frac{E_0 + E_{had}}{m}\right)\right] . \tag{5.20}$$

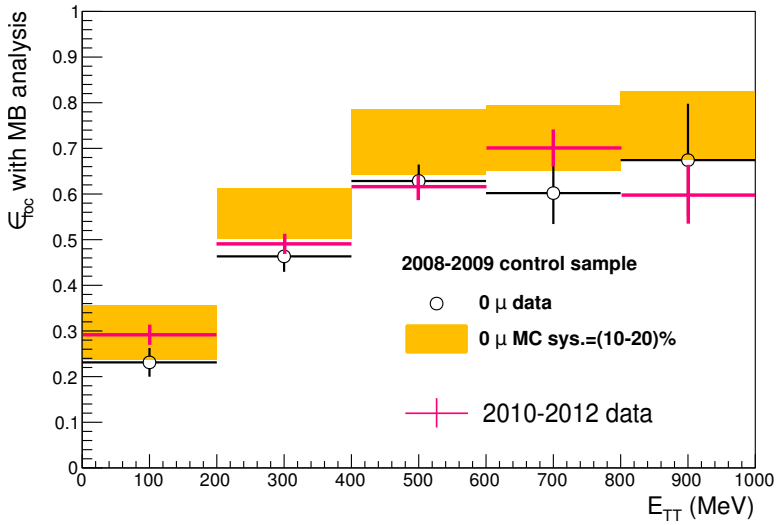

(a) Location efficiency vs TT energy

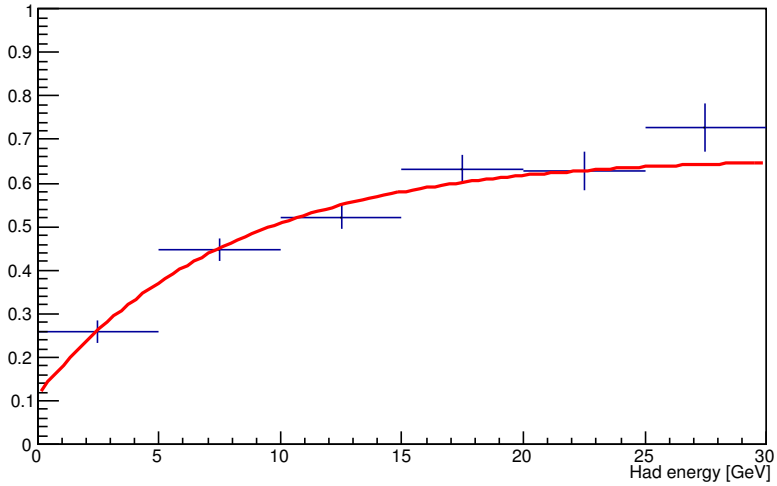

(b) Location efficiency vs hadronic energy

Figure 5.10: *Location efficiency as a function of E_{TT} and of the hadronic energy for 2010-2012 data sample. In (a) the efficiency is compared with the control sample published in [74]. The fitted curve in (b) is defined in equation 5.20 and the results are in Table 5.5.*

Table 5.5: *Location efficiency fit results. The parameters are defined in equation 5.20 and data comparison can be seen in Figure 5.10b.*

ε_0	0.66 ± 0.03
E_0	1.5 ± 0.9 GeV
m	8 ± 2 GeV

The fitted parameters can be seen in Tables 5.4 and 5.5, respectively.

In order to considered these effects into the simulation, each event weight obtained at the generator level – equation 5.8 – is multiplied by the product $\varepsilon_{BF} \cdot \varepsilon_{loc}$. The two functions are evaluated at the event hadronic energy as described in equations 5.18 and 5.19.

5.4.3 Momentum and energy reconstruction

In the OPERA experiment, the momentum reconstruction using the emulsion data is obtained from the Multiple Coulomb Scattering method, see Section 2.4.5. In order to avoid a complete brick simulation, it was taken into account using a parameterization. As stated in [66], the momentum resolution has different behaviors depending on the initial track tilt with respect to the brick z axis (θ), the number of emulsions crossed by the track (N_{pl}) and the momentum (p). For $\theta < 0.2$, the resolution is

$$\begin{aligned} \frac{\sigma_{1/p}}{1/p}(p, N_{pl}) &= \frac{0.397 + 0.019\,\mathrm{GeV}^{-1} \cdot p}{\sqrt{N_{pl}}} + (0.176 + 0.042\,\mathrm{GeV}^{-1} \cdot p) \\ &\quad + \sqrt{N_{pl}}(-0.014 - 0.003\,\mathrm{GeV}^{-1} \cdot p) \end{aligned} \tag{5.21}$$

while, for $\theta > 0.2$, it is slightly worse:

$$\begin{aligned} \frac{\sigma_{1/p}}{1/p}(p, N_{pl}) &= \frac{1.400 - 0.022\,\mathrm{GeV}^{-1} \cdot p}{\sqrt{N_{pl}}} + (-0.040 + 0.051\,\mathrm{GeV}^{-1} \cdot p) \\ &\quad + \sqrt{N_{pl}}(0.003 - 0.004\,\mathrm{GeV}^{-1} \cdot p) \end{aligned} \tag{5.22}$$

This smearing is applied on every charged track substituting its true momentum with a random value according to the distribution given by its resolution. A log-normal momentum distribution is assumed, with mean equal to the true momentum and variance given by equations 5.21 or 5.22. The reason why a log-normal distribution is preferred to a Gaussian distribution is that a positive momentum is required, but this is not guaranteed by a Gaussian, especially with high sigma values. The variance distribution is evaluated assuming

$$\frac{\sigma_p}{p}(p, N_{pl}) = \frac{\sigma_{1/p}}{1/p}(p, N_{pl}) \tag{5.23}$$

which is one the main ansatz of the momentum resolution analysis.

The resolution has a dependence on N_{pl}. This value was estimated using particle range in lead provided by the NIST database [76]. Due to the position of the vertex inside the brick, the maximum of N_{pl} is set to 26.

Having a maximum in N_{pl}, the ratio $\frac{\sigma_p}{p}$ could grow larger than 1, especially for tracks coming from high energy events. This is not likely to happen: usually, such a high momenta could be estimating using the MCS method in downstream bricks or by range in the detector material. So, the maximum $\frac{\sigma_p}{p}$ has been fixed at 50 %.

For the photons, the same procedure based on log-normal distribution is applied, although the energy resolution $\frac{\sigma_E}{E}$ is constant at 50 %.

5.5 Data selection

Out of the whole production, only events with the interesting topology were used in the next step of the analysis. The event topology that was searched for has the following features:

- no muon reconstructed at the primary vertex;
- a one prong-like secondary vertex (1pr-like);
- a two prong-like secondary vertex (2pr-like).

A 1pr-like secondary vertex is a kink, namely the number of MIP daughters is just one. The daughter has to be a charge track, which is not reconstructed as a muon; electrons or positrons were discarded as well. Also the parent is explicitly required to be charged, therefore a minimum z is required for the secondary vertex, in order to allow the parent to cross at least the first emulsion of the first emulsion film (plate 32) so that the track ca be seen. This minimum z is 0.3318 mm. The parent maximum flight length is requested to be at 4 mm.

Due to the association ambiguity of track 2 – see Section 3.1.2 – the 2pr-like secondary vertex can have two or three MIP daughters. None of them has to be reconstructed as a muon and electrons or positrons are discarded. For this vertex, there is no charge requirement so there is no minimum z. Still, the parent maximum flight length is 4 mm.

Nuclear fragments associated to a secondary vertex are not counted as daughters. At this stage, secondary vertices with associated fragments are still selected.

5.5.1 Very short decays

The propagation engine reconstructs a parent track whenever the parent crosses an emulsion or at least one of its daughters is reconstructed. This is a very good approximation especially for 1pr-like vertices selection, since

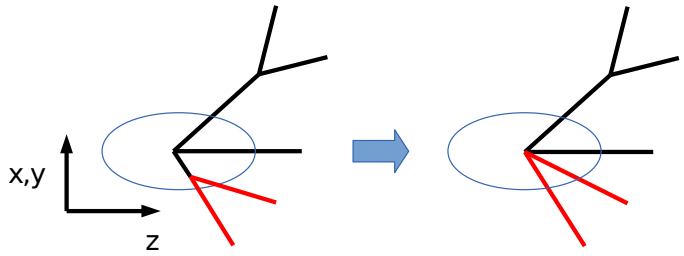

Figure 5.11: *Secondary vertices with too short parent are not reconstructed and their daughters are associated to the primary vertex.*

they always have visible parent. Anyway, secondary vertices very close to the primary cannot be reconstructed because this would require a much higher resolution. In order to take into account this effect, an ellipsoidal region around the primary vertex was defined: secondary vertices within this region were not reconstructed and their daughter tracks were associated to the primary vertex, see Figure 5.11. The ellipsoid axes are parallel to the brick reference frame and the semi-axes have length 40 μm along the z direction and 10 μm in the transverse plane.

5.5.2 Expected events

The number of expected events having the interesting topology is obviously very low. The selection efficiency depends mostly on the process: DIS ν_τ CC easily produces secondary vertices and, in case of charm production, the selection efficiency is around 14 %. While, for events from NC DIS interaction or ν_μ CC DIS, the efficiency is very small, down to 10^{-5}. Also, around these average values, these efficiencies have a dependence on the neutrino energy. The final expected sample consists of 0.1 events. Table 5.6 summarizes the expected events from every considered process. More details about the particles selected with these topology requirements are shown in Appendix A.

The table numbers are evaluated with a pure topological selection. This does not mean that the selected ν_τ CC events always include heavy particle tracks. For instance, not all the tracks with secondary vertex from the DIS ν_τ CC sample are taus or charmed particles, since there are auto-contaminations coming from other hadrons produced in the interaction. The same happens in the ν_τ CC sample without charm. This contribution is very small; Table 5.7 shows the expected events from contaminations within the ν_τ CC samples.

These auto-contamination sub-samples are expected to have different properties since they contain different particles, so they are treated separately in the next steps of the analysis. Interesting events, i.e. events with at least a tau selected by the topology cuts, will be labeled as *Signal* while not interesting events are considered *background*. In the following, the τ+non-

Table 5.6: *Expected events with the interesting topology described in Section 5.5.*

	Expected events (10^{-3})		
Sample	Only topology	With efficiency	No fragments
DIS ν_μ CC	342 ± 9	114 ± 3	4.0 ± 0.5
DIS ν_μ CC + charm	534 ± 4	188 ± 1	20.5 ± 0.5
DIS ν NC	273 ± 4	96 ± 2	3.8 ± 0.3
DIS ν NC + $c\bar{c}$ pair	27.5 ± 0.1	14.83 ± 0.03	12.59 ± 0.02
DIS ν_τ CC	104.7 ± 0.9	31.7 ± 0.2	9.0 ± 0.1
DIS ν_τ CC + charm	151.8 ± 0.6	51.3 ± 0.1	44.5 ± 0.1
Total	1433	496	94.4

Table 5.7: *Auto-contamination sub-samples from interesting samples.*

(a) *With fragments*

	Expected events (10^{-3})		
	τ + charm	τ + non-charm	no τ
DIS ν_μ CC + charm	49.9 ± 0.1	0.60 ± 0.01	0.80 ± 0.02
DIS ν_μ CC	0	31.2 ± 0.2	0.52 ± 0.03

(b) *Without fragments*

	Expected events (10^{-3})		
	τ + charm	τ + non-charm	no τ
DIS ν_μ CC + charm	44.0 ± 0.1	0.270 ± 0.009	0.230 ± 0.009
DIS ν_μ CC	0	9.0 ± 0.1	0.074 ± 0.010

charm sub-samples are treated as background since the presented analysis is design to the search for tau with a charmed particle. The analysis performed for the τ+any searches is described in appendix B.

5.5.3 Discrimination variables

After the topology selection, some kinematic variables were defined. Some of them are derived from the standard OPERA analysis while others were newly introduced as peculiar of such topology. Only variables which can be well measured for the interesting event were considered.

The first group is designed to characterize the 1pr-like vertex. These are:

- the *daughter momentum* coming from the vertex;
- the *daughter transverse momentum* with respect to the parent direction;
- the *kink* angle between parent and daughter;

- the *flight length* with respect to the primary vertex;

whose spectra can be seen in Figure 5.12. Others, see Figure 5.13, describe the 2pr-like vertex:

- the *daughters momentum*, which is the module of total momentum of the daughters;
- the *transverse daughters momentum* with respect to the parent direction;
- the *invariant mass* of the daughters, for which the daughters masses are assumed to be equal to the pion mass;
- the *flight length* with respect to the primary vertex.

Finally, other variables are related to the whole event:

- the *total EM energy* is the sum of all the visible photons energy, regardless of the photon origin vertex;
- the *transverse angle* with respect to the beam direction between the tracks which end up in 1pr-like and 2pr-like vertices, so called φ;
- the *missing transverse momentum at primary* with respect to the beam direction;
- the *other hadronic momentum*, which is the module of the momenta coming from the primary vertex discarding tracks that end up in a secondary 1pr-like or 2pr-like vertex.

Their spectra can be seen in Figure 5.14.

All these variables are weakly correlated among themselves and even in the few cases they are, the correlation has different strength between signal and background samples, see Figure 5.15. More variables could have been defined but there would not be much improvement: the extra ones would have been strongly correlated to the ones already defined.

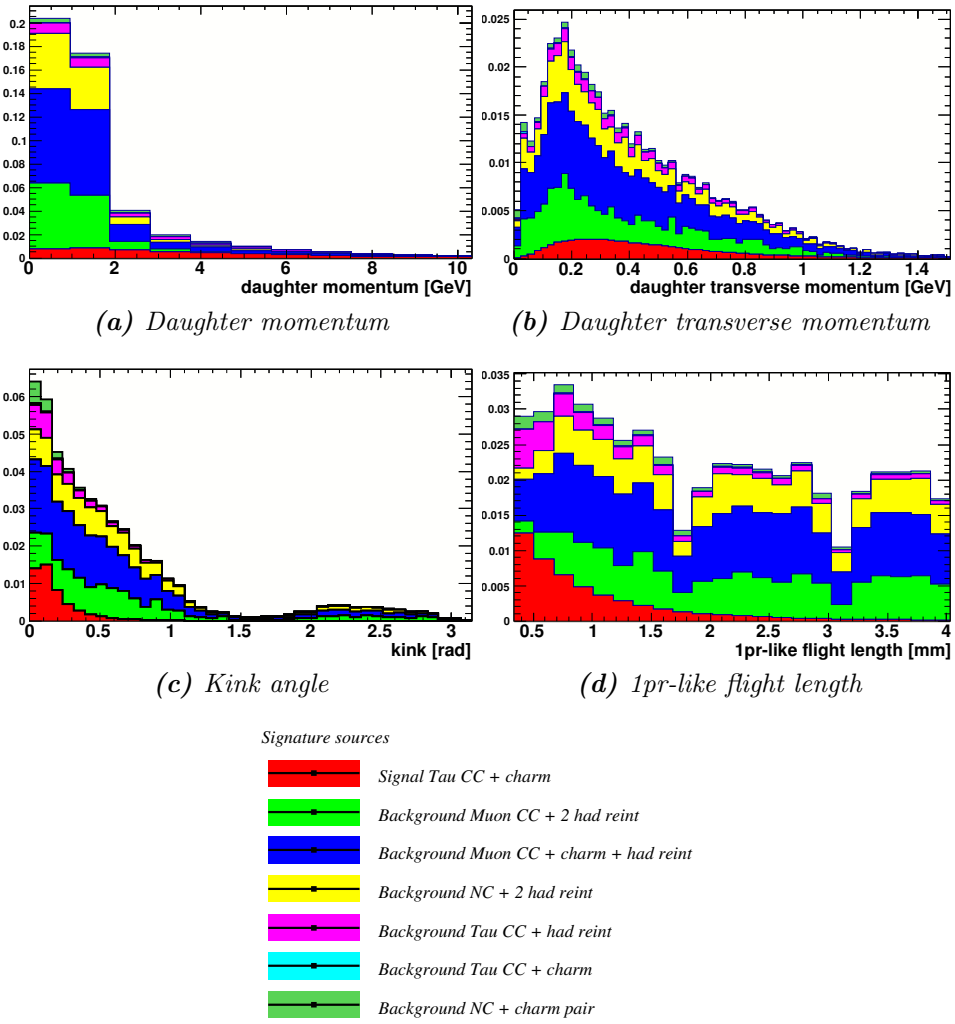

(a) Daughter momentum *(b) Daughter transverse momentum*

(c) Kink angle *(d) 1pr-like flight length*

Figure 5.12: *Spectra of the variables describing the 1pr-like secondary vertex.*

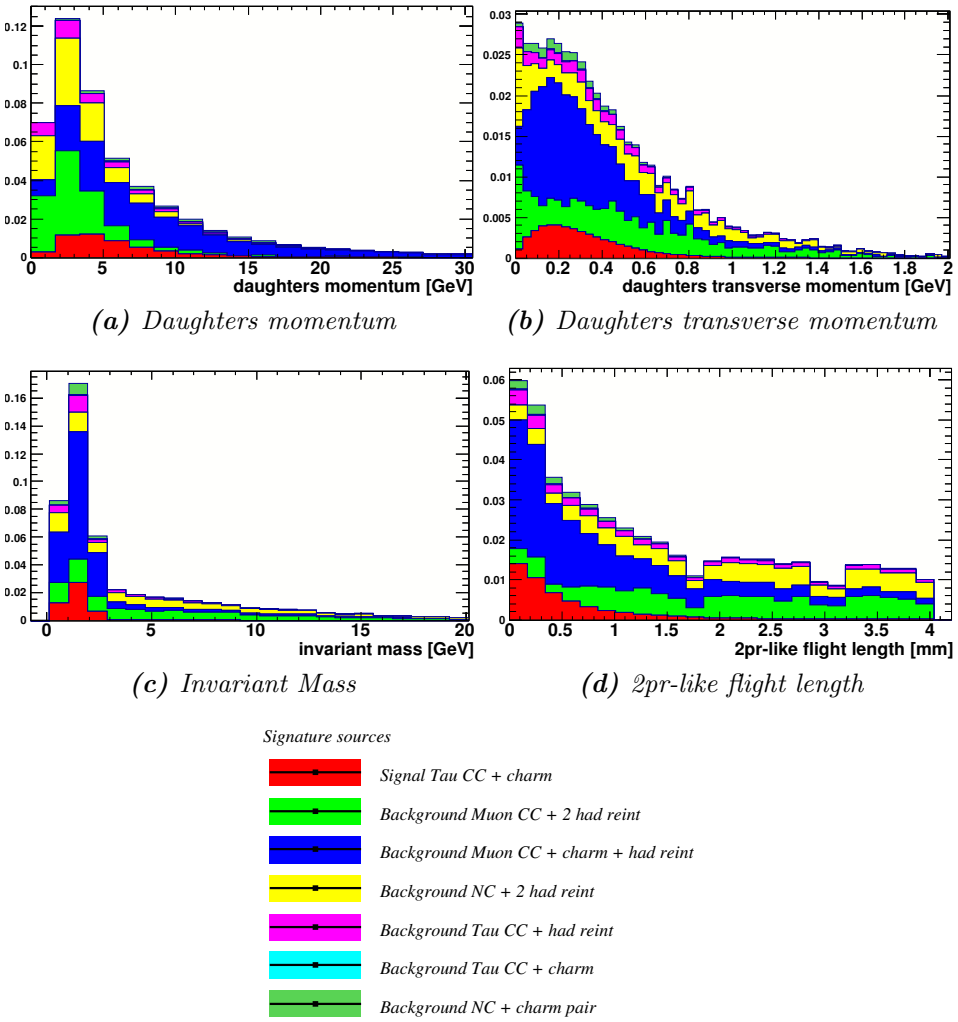

(a) *Daughters momentum* ***(b)*** *Daughters transverse momentum*

(c) *Invariant Mass* ***(d)*** *2pr-like flight length*

Figure 5.13: *Spectra of the variables describing the 2pr-like secondary vertex.*

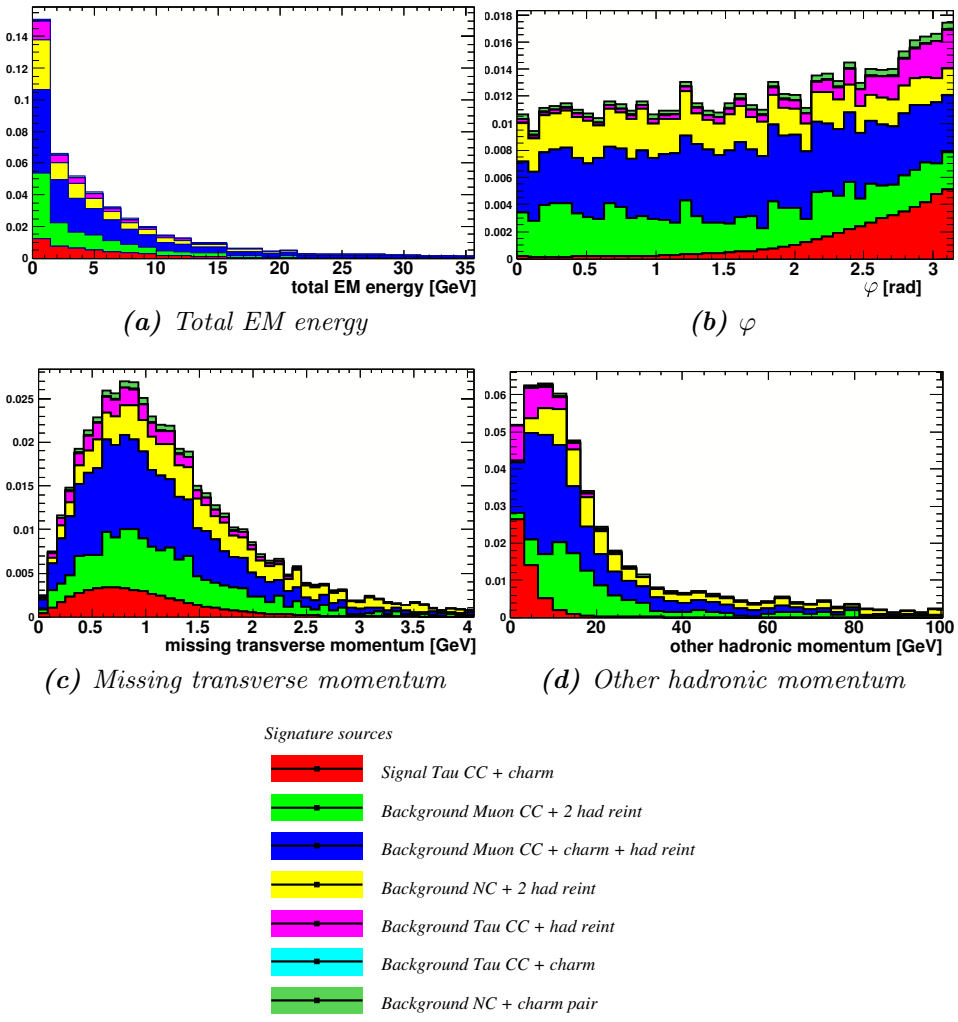

(a) Total EM energy *(b) φ*

(c) Missing transverse momentum *(d) Other hadronic momentum*

Figure 5.14: *Global variables spectra.*

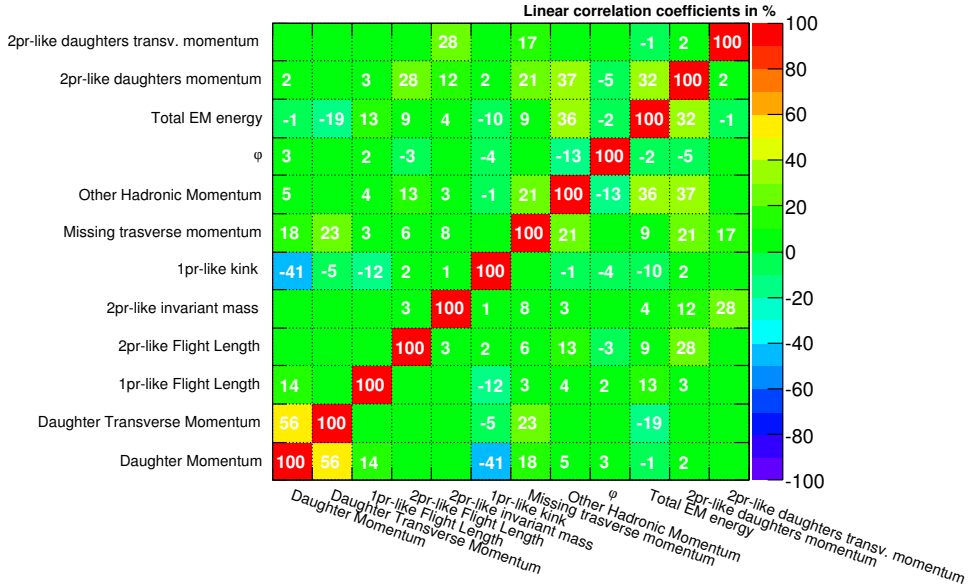

(a) Signal sample

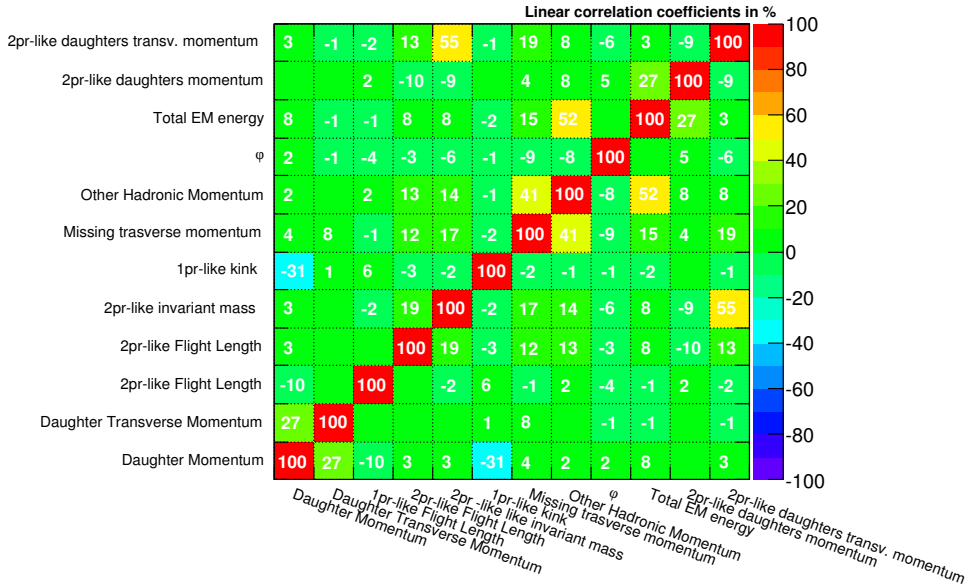

(b) Background sample

Figure 5.15: *Linear correlations between the variables.*

Chapter 6

Event analysis

Out of the peculiar topology of the interesting event, a lot of information was extracted, namely twelve variables were defined in order to characterize the events having two secondary vertices. This chapter presents how all this information is merged together. In particular, some refined algorithms are presented and the best one is used to evaluate the event's nature. For the most likely configuration, the significance of this observation is evaluated.

6.1 Multivariate classification

A multivariate classifier is a class of "supervised learning" algorithms. They make use of training events to determine the mapping function that describes a decision boundary. The mapping function can contain various degrees of approximations and it may be a single global function or a set of local models. All the classifiers used for this analysis are provided by the TMVA package [97].

In the presented analysis, the classifiers were trained to discriminate between events with a tau and a charmed particle in the final state against any other possibility. The search for tau with any other particle (tau+any) is described in appendix B.

6.1.1 The methods

In order to find the best method for the discrimination, several algorithms were tested. Four possibilities were explored.

ANN (Artificial Neural Network) is generally speaking any simulated collection of interconnected neurons, each neuron producing a certain response at a given set of input signals. By applying an external signal to some (input) neurons the network is set into a defined state that can be measured from the response of one or several (output) neurons.

The flavour used for this analysis is the MLP (Multi Layer Perceptron) implemented with two neuron layers between input and output neurons.

Boost Decision Trees are trees of binary choices taken on one single variable at a time until a stop criterion is fulfilled. Two different flavours were chosen: the default Adaptive Boost [98] (labeled **BDT**) and the Gradient Boost (**BDTG**). With respect to the Adaptive Boost, the latter is more stable with respect to outliers which can occur by chance in any distribution, especially heavy-tailed distribution.

Fisher discriminant [99] is a linear classifier. During the training, the input variables are transformed in order to remove the linear correlations, distinguishing between signal and background. Then, the selection is performed in this transformed variable space with zero linear correlations. The linear discriminant analysis determines an axis in the hyperspace of the input variables such that, when projecting the output classes (signal and background) upon this axis, they are pushed as far as possible away from each other, while events of a same class are confined in a close vicinity.

6.1.2 Training and overtraining

A proper training requires a large number of events, in order to cover the variable space. That is why the training was performed using the events with nuclear fragments included. After the training, only events without nuclear fragments are considered.

At first, the classifiers were tested to search for overtraining. Overtraining occurs when a machine learning problem has too few degrees of freedom, because too many model parameters of an algorithm were adjusted to too few data points. The sensitivity to overtraining therefore depends on the method.

The test is performed dividing the MC sample in two groups: one is used for training, the other just to obtain an independent output spectrum. If test and train samples have the same output distributions, the algorithm is not overtrained. The compatibility is performed using the Kolmogorov-Smirnov test [100]. Because of its structure, the Fisher discriminant can hardly ever be overtrained [97] and its compatibility is treated as a benchmark. The results of such a test is presented in Figure 6.1.

As can be seen, three of the discriminants have very high compatibility while the BDT compatibility is one order of magnitude worse, even if all the tests share the same train and test samples.

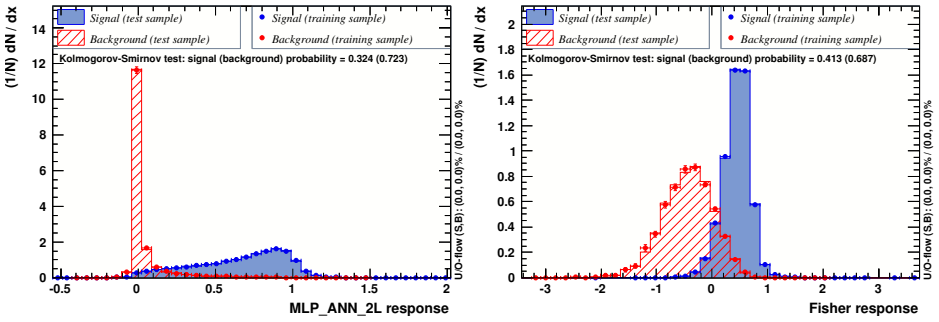

(a) Artificial Neural Network

(b) Fisher discriminant

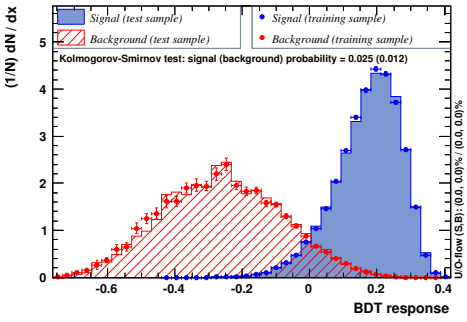

(c) BDT

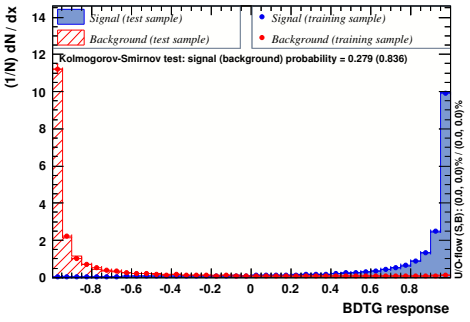

(d) BDTG

Figure 6.1: *Discriminants overtraining test results.*

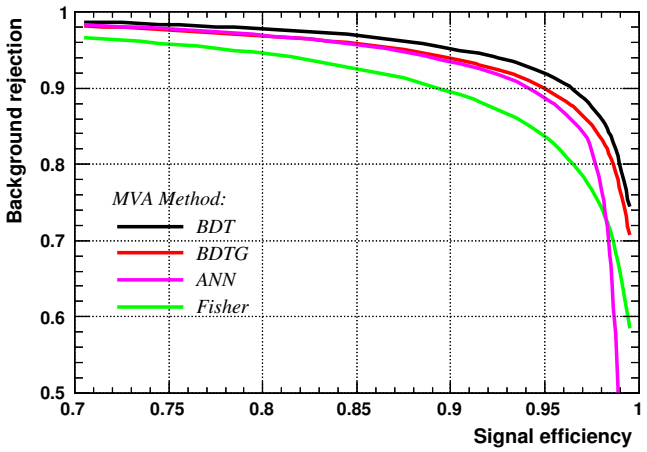

Figure 6.2: *Background rejection against signal efficiency for all the trained classifiers.*

6.1.3 Performances

In general, once a classifier output spectrum was obtained, a simple selection cut could be decided. This is enough to define a signal efficiency and a background rejection. In fact, the signal efficiency is the fraction of signal events above the cut and the background rejection is the fraction of background events below the cut. For every classifier, these two quantities are plotted one against the other, see Figure 6.2. Discriminant performance is as good as the curve is close to top-right edge of the plot.

The algorithm having the best discrimination power seems to be the BDT. BDTG and ANN have very similar properties, while the Fisher discriminant is definitely the worst. This was expected since Fisher discriminant is just a linear discriminant.

6.1.4 Discrimination effectiveness

Previous tests are typical for discriminators designed to select optimal samples, according to criteria which are generally purity and signal efficiency. In this case, it's known from the dedicated MC (chapter 5) that no more than one event is expected to be observed. Moreover, observing more events of this kind would prove that some important backgrounds were neglected. In this condition, the designed classifier has one more requirement: it is required to provide the best chance to give the "clearest indication" about the event nature. Of course this was done blindly with respect to the classifiers outputs evaluated on the event variables.

The probability to be a signal event is evaluated as a function of the classifier output variable. For completeness the probability was also evaluated

for each background source. In particular, these probabilities were evaluated as a function of the bins of the output classifier histograms. Being α the bin index, the probability of being from the i-th process is given by

$$p_i(\alpha) \equiv \frac{x_i(\alpha)}{\sum_k x_k(\alpha)} \tag{6.1}$$

where $x_i(\alpha)$ is the number of the expected events from the i-th source in bin α. In this case, events with associated fragments are not included and the spectra of x_i as a function of the classifier output variables can be seen in Figure 6.3. The probabilities are in Figure 6.4.

The statistical error on the expected events is also propagated, in order to understand whether the simulation statistics is large enough. Each component x_i has its variance σ_i, defined in equation 5.11, which is propagated according to

$$\sigma^2_{p_i} = \sum_j \left(\frac{\partial p_i}{\partial x_j}\right)^2 \sigma_j^2 \tag{6.2}$$

$$= \frac{1}{(\sum_k x_k)^2}\left[\sigma_i^2 + p_i^2 \sum_j \sigma_j^2 - 2p_i\sigma_i^2\right] \tag{6.3}$$

where the bin dependence was dropped for simplicity.

In this contest, an indication about the event nature is considered "clear" if the probability associated to the i-th sources is higher than any other option. From this point of view, the most effective classifier is then the ANN that has the largest region in which signal and background probabilities are well separated.

6.1.5 Result

After all previous considerations, the classifier used for the final evaluation is the ANN. The variables values used as input are presented in Table 6.1, while Table 6.2a shows the probabilities corresponding to each channel for all classifiers. The event is clearly in the region dominated by ν_τ CC with charm interactions.

A posterior test was performed on the classifiers in order to check if the result is stable with respect to measurement uncertainties. In fact, although the simulation considers some effects such as momentum resolution, it does not considers the ambiguity in track association, as happens for track 2. To perform such test, starting from the event measurements, a distribution of pseudo-events was generated and its output variable spectrum was evaluated. The event tracks were generated varying their momenta according to the experimental resolution. In this case, also the association of track 2 was changed between vertex I and II. For each pseudo-event, the ANN output

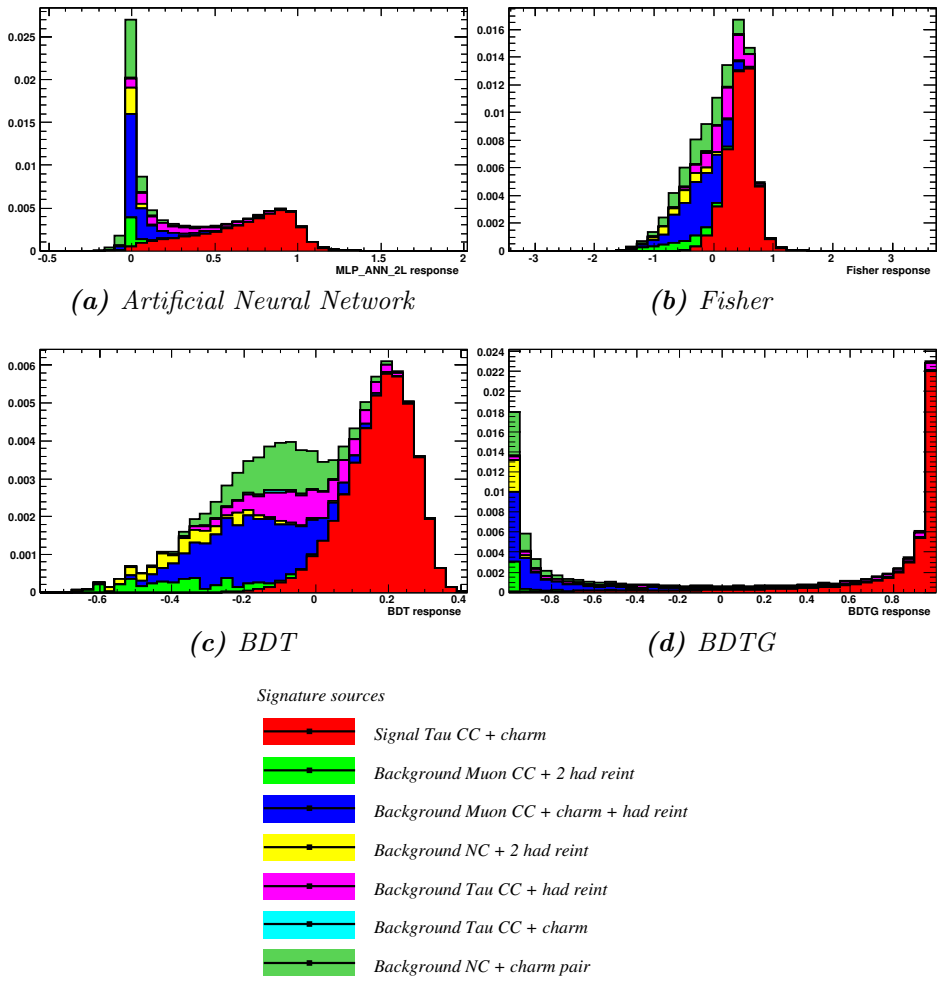

(a) *Artificial Neural Network* ***(b)*** *Fisher*

(c) *BDT* ***(d)*** *BDTG*

Figure 6.3: *Classifier spectra. The auto-contamination component is very small and hardly visible.*

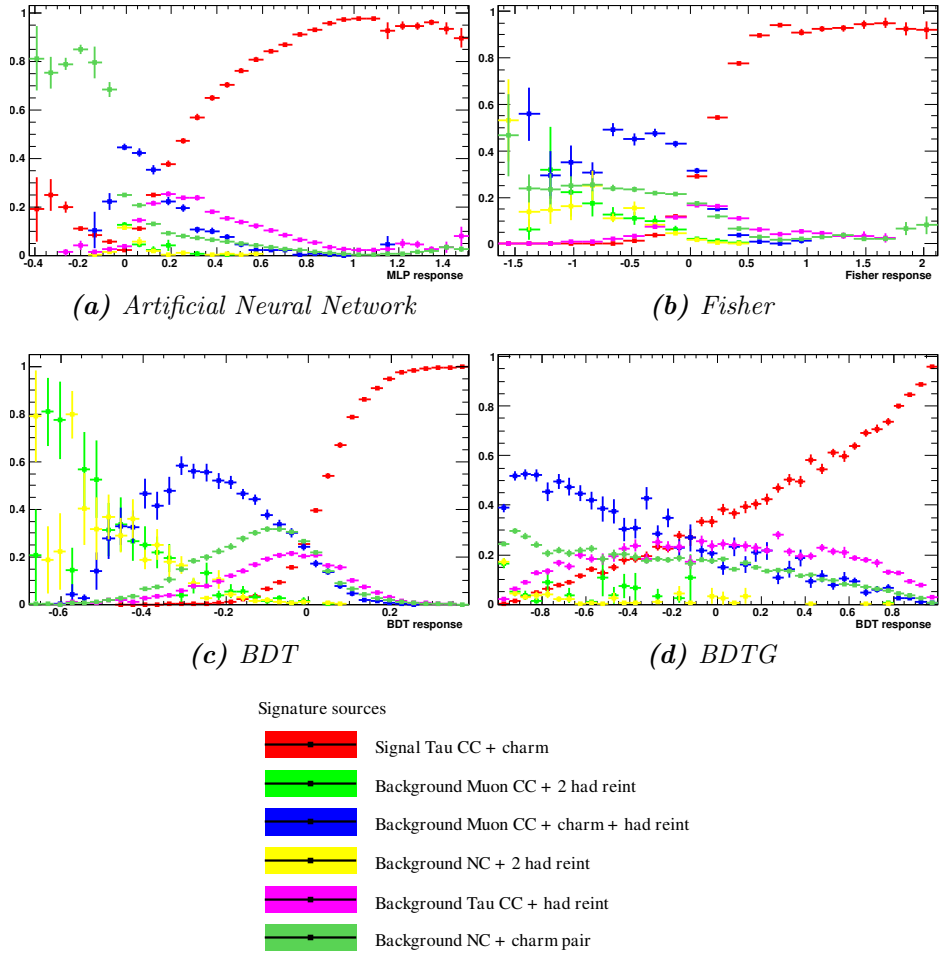

(a) Artificial Neural Network *(b) Fisher*

(c) BDT *(d) BDTG*

Figure 6.4: *Sources probabilities as a function of the discrimination response*

Table 6.1: *Variable used for the final evaluation.*

variable	value
1pr-like daughter momentum	2.7 GeV/c
1pr-like daughter transverse momentum	0.242 GeV/c
Kink angle	90 mrad
1pr-like flight length	1.16 mm
2pr-like daughters momentum	6.17 GeV/c
2pr-like daughters transverse momentum	0.542 GeV/c
2pr-like invariant mass	1.86 GeV/c^2
2pr-like flight length	103 μm
Total EM energy	13 GeV
φ angle	2.41 rad
Missing transverse momentum	0.876 GeV/c
Other hadronic momentum	0.850 GeV/c
ANN output	**0.957**

Table 6.2: *Probability of the interesting event for ANN and other classifiers algorithms.*

(a) *Event evaluation*

source	ANN	Fisher	BDT	BDTG
ν_μ CC DIS	0 %	0 %	0 %	0 %
ν_μ CC DIS + charm	0.02 %	0.95 %	0 %	0.47 %
ν NC DIS	0 %	0 %	0 %	0 %
ν NC DIS + $c\bar{c}$ pair	0.49 %	3.1 %	0.36 %	0.83 %
ν_τ CC DIS	2.5 %	6.3 %	0.64 %	3.0 %
ν_τ CC DIS + charm	97.0%	89.6 %	99.0 %	95.7 %

(b) *Pseudo-events*

source	ANN	Fisher	BDT	BDTG
ν_μ CC DIS	0 %	0.25 %	0 %	0 %
ν_μ CC DIS + charm	0.30 %	2.50 %	0.09 %	0.48 %
ν NC DIS	0 %	0.19 %	0 %	0 %
ν NC DIS + $c\bar{c}$ pair	0.82 %	4.85 %	0.60 %	0.86 %
ν_τ CC DIS	3.4 %	8.7 %	0.87 %	3.0 %
ν_τ CC DIS + charm	95.4 %	83.4 %	98.4 %	95.6 %

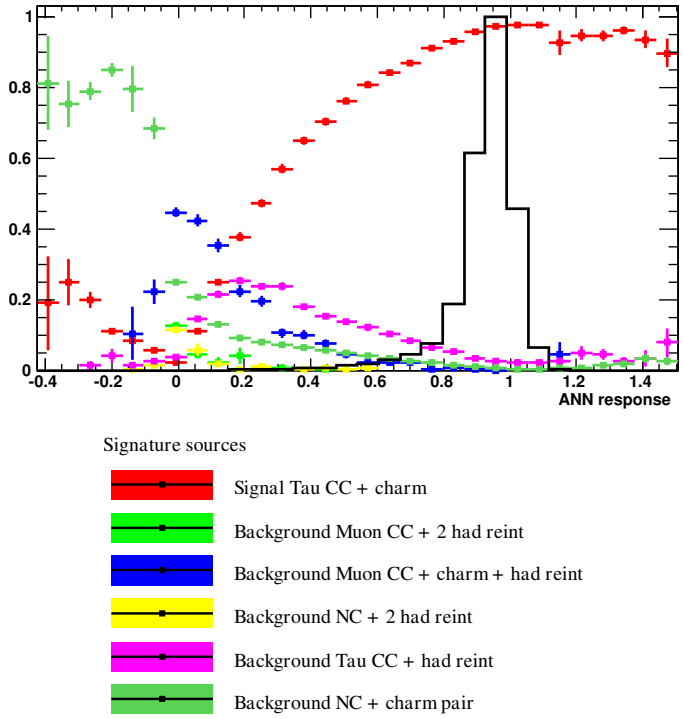

Figure 6.5: *Sample probability as a function of the ANN output variable (colored dots) compared to the pseudo-events distribution generated for posterior test (black line). The pseudo-events distribution was scaled so that the distribution maximum is 1.*

value is calculated, obtaining a distribution in the output classifier variable, called $h(\alpha)$, see Figure 6.5. So, the final event i-th source probability, p_i, has to be evaluated according to $h(\alpha)$:

$$p_i = \sum_{\alpha} p_i(\alpha) h(\alpha) \tag{6.4}$$

where $p_i(\alpha)$ is the probability defined in equation 6.1. These p_i values, Table 6.2b, are very close to the single event results proving the stability of the developed algorithms.

The nature of the event is also confirmed by the classifiers developed for tau+any searches. In that case, the signal sample used to train the classifiers is made of ν_τ CC DIS events with or without charm. Even though these classifiers are not trained to identify interactions with charm, our event is in a region where the probability to be a ν_τ CC interactions with charm is grater than 75 % for every classifier. Figure 6.6 shows the ANN spectrum and the probability curves.

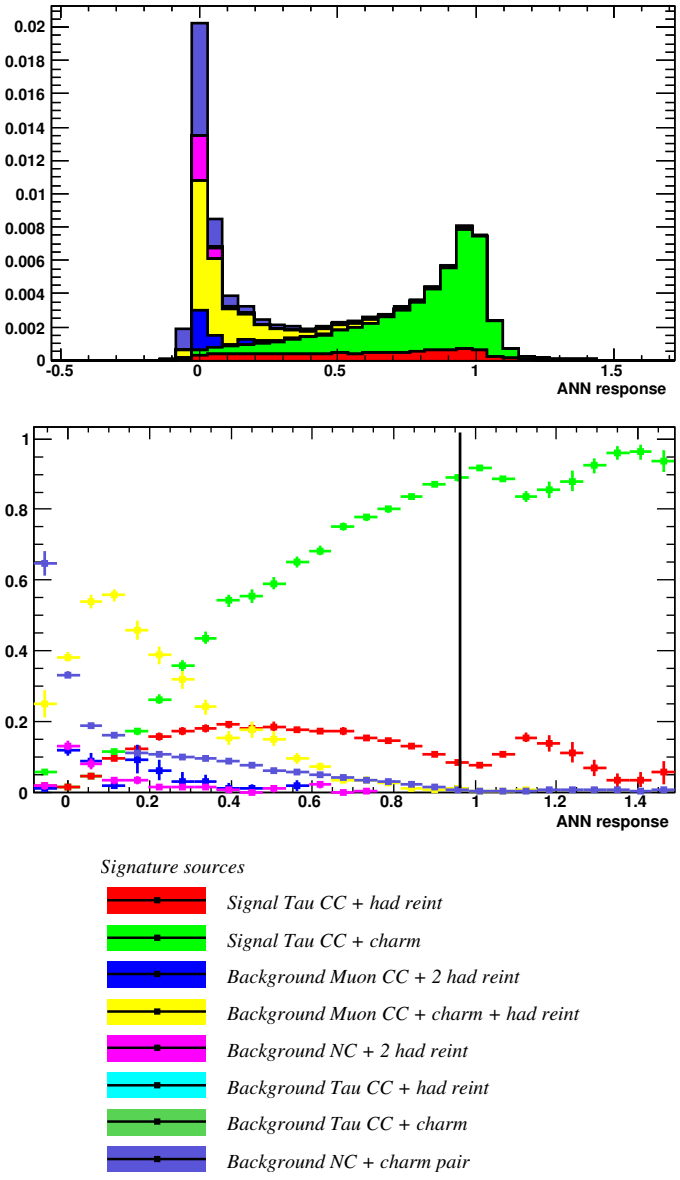

Figure 6.6: *ANN trained for tau+any events searches. The black line is the event position.*

6.2 Significance

Although the previous results are quite encouraging, up to now this analysis is just an ad-hoc procedure. In high energy physics, the analyses usually require the evaluation of the observation significance: this is the probability to observe the event assuming an only background hypothesis.

The tools used for this calculation are the RooFit and RooStats libraries [101] provided by the ROOT framework [89].

6.2.1 The model

In order to evaluate the significance, a statistical model has to be defined, namely the Probability Density Function (PDF). In this case, it is the PDF of the output classifier variable, from now on called x, that is the observable of our statistic problem. Roughly speaking, the x PDF is the overall ANN spectrum shown in Figure 6.3a. Being $f_i(x)$ the i-th source spectrum, normalized to 1, the total shape, $\mathbb{S}(x)$, is given by

$$\mathbb{S}\,(x) = \sum_i n_i \cdot f_i(x) \tag{6.5}$$

where n_i are the number of expected events for the i-th contribution, see Table 5.6. The number of expected events, n, has a Poissonian distribution with mean equal to $\sum_i n_i$.

In order to evaluate the significance, the background only model is required to be nested within the global PDF. This is implemented defining a parameter μ, the signal strength, such that it multiplies the n_i belonging to the signal sample. So, the background only hypothesis corresponds to $\mu = 0$, while $\mu = 1$ is the model with the expected signal. Finally, the likelihood can be written as

$$\mathcal{L}(\mu|x) = \sum_{i\in B} n_i \cdot f_i(x) + \mu \sum_{j\in S} n_j \cdot f_j(x)\ . \tag{6.6}$$

where S and B are the signal and background sources, respectively. In this model description, the number of expected events is given by:

$$N = \sum_{i\in B} n_i + \mu \sum_{j\in S} n_j\ . \tag{6.7}$$

The μ parameter is free and it can be fitted; results can be seen in Figure 6.7. For tau with charm searches, S is just the ν_τ CC DIS with charm production. This formalism was chosen because it can also be applied to tau+any searches.

Because of the poor statistics, it is interesting to evaluated the μ posterior probability distribution, Figure 6.8. This distribution is peaked at 22.7, the 68 and 95 % CL Bayesian shortest intervals are $[6.125; 56.55]$ and $[0.925; 108.2]$, respectively. Hence, the nominal signal expectation, $\mu = 1$, is contained in the 95 % CL region.

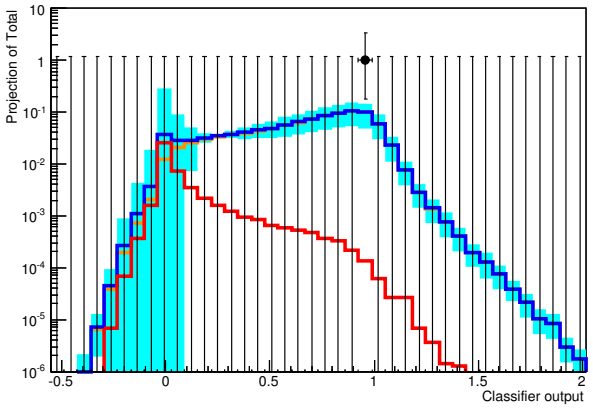

Figure 6.7: *Comparison between data and fitted model. The red curve is the background only hypothesis, the orange one is the signal component, while the blue is the total fitted value. The cyan area corresponds to the propagation of the fitted error on μ.*

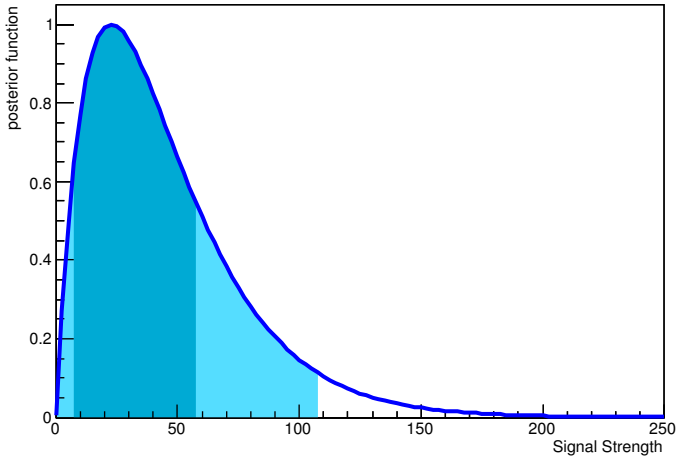

Figure 6.8: *Posterior μ distribution. The two interval are the 95 and 68 % CL Bayesian shortest intervals.*

6.2.2 The method

For the significance evaluation, a sample of toy MC experiments was generated according to the background only PDF. Then, for each MC experiment, a test statistic is evaluated on the pseudo-experiment.

A test statistic is a measure of some attribute of a sample used in statistical hypothesis testing [102]. The the most trivial example is given by the number of observed events. In general, a test statistic is selected or defined in such a way that it can quantify behaviours that would distinguish the null from the alternative hypothesis, namely background only from signal plus background model. The test statistic used for the analysis is the profile likelihood ratio, which is often used among high energy physics experiments [103, 104] because of its good performance in presence of nuisance parameters.

The test statistics spectra can be seen in Figure 6.9a. The CL of the background only hypothesis is evaluated as the fraction of events with test statistic result higher than the event value. The CL is then converted is terms of sigma, using

$$n_\sigma = \sqrt{2} \cdot \mathrm{Erf}^{-1}\left(2 \cdot CL - 1\right) \tag{6.8}$$

where Erf^{-1} is the inverse of the Gauss Error function. The significance of this event in this simple scenario is $3.4\,\sigma$.

6.2.3 Systematic contributions

So far, no systematic contributions were considered, thought some of them are know to be not negligible in the OPERA experiment. These effects are parameterized as scale factors, s_i, which multiply the number of expected events from each contribution; each source has different scale factors. These scale factors depend on some nuisance parameters, σ_k, that have a supposed know PDF, labeled g_k in the following.

The first nuisance parameter is a normalization factor, σ_N. The normalization is expected to be dominated by the CNGS flux uncertainty, which is estimated to be about 20 % [50]. Thus, the normalization factor is expected to be in the $[0; 2]$ range with a Gaussian PDF with mean and sigma equal to 1 and 0.2, respectively. The range was selected as it corresponds to $5\,\sigma$ from the mean value.

Another source of uncertainty is coming from the cross sections of rare processes such as ν_τ CC interactions or NC interactions with charm pair production. In particular, two processes were never observed in the OPERA experiment: NC interactions with charm pair and ν_τ CC interactions with single charm. For these two processes two different factors were defined, namely $\sigma_{c\bar{c}}$ and $\sigma_{\tau c}$. Both of them are assumed to have a uniform distribution in the 1 ± 20 % range. The 20 % uncertainty is the usual OPERA parameterization for quantities which are relatively unknown. For the ν_τ

Table 6.3: *Scale factors definitions as functions of the nuisance parameters.*

channel	s_i
ν_μ CC DIS	$\sigma_N \cdot \sigma_h^2$
ν_μ CC DIS + charm	$\sigma_N \cdot \sigma_h$
ν NC DIS	$\sigma_N \cdot \sigma_h^2$
ν NC DIS + $c\bar{c}$ pair	$\sigma_N \cdot \sigma_{c\hat{c}}$
ν_τ CC DIS	$\sigma_N \cdot \sigma_h \cdot \sigma_\tau$
ν_τ CC DIS + charm	$\sigma_N \cdot \sigma_{\tau c}$

CC interactions without charm, σ_τ, the cross section systematic is estimated from [105] to be about 6 % for ν_τ in the few tens of GeV range. Hence, this contributions is implemented as a Gaussian in the $[0.7; 1.3]$ interval with mean and standard deviation equal to 1 and 0.06, respectively. Also in this case, the parameter range corresponds to the $5\,\sigma$ region around the mean.

The last contribution is given by the hadron re-interaction uncertainty. As concluded at the end of chapter 4, the prediction from the GEANT4 simulation are expected to be true within 30 %. So, the assumed distribution for this factor is uniform in the $[0.7; 1.3]$ range. It is called σ_h.

Each nuisance parameter distribution g_k, depends on some constant parameters such as the range boundaries or other PDF parameters like Gaussian variances. These are different for each g_k and for completeness they are labeled $\hat{\boldsymbol{\sigma}}_k$. Hence, the nuisance parameters distributions will be identified as $g_k(\sigma_k|\hat{\boldsymbol{\sigma}}_k)$. Some of the fixed parameters are definitely chosen ad-hoc. This not very important: the main goal of this part of the analysis is to understand if the significance is stable with respect to variations of the model parameters.

6.2.4 Scale factors

Starting from the σ_k defined above, a scale factor for each process is evaluated, namely $s_i(\boldsymbol{\sigma})$, which can be a function of all the σ_k. The definitions are summarized in Table 6.3.

Some nuisance parameters are specifically defined for a particular channel, while others are common to more contributions, for instance the normalization factor is applied to every channel. The other shared contribution is the hadronic re-interaction uncertainty which is applied whenever one of the secondary vertex is required to be produced by an hadron re-interaction. If the topology requires two hadron re-interactions, σ_h will be squared.

Table 6.4: *CL and significance of the observed event with respect to the background only hypothesis.*

	CL (10^{-4})	n_σ
No systematics	3.0 ± 0.3	3.43 ± 0.03
With systematics	2.6 ± 0.2	3.47 ± 0.02

6.2.5 Global PDF

Using previous definitions, a global PDF can be constructed. The principle is the same as for the model without systematic, equation 6.7, although now the number of expected events n_i are multiplied by the scale factors s_i. Hence, the complete PDF is

$$\mathcal{L}(\mu, \boldsymbol{\sigma}|x) = \left[\sum_{i \in B} n_i \, s_i(\boldsymbol{\sigma}) \, f_i(x) + \mu \sum_{j \in S} n_j \, s_j(\boldsymbol{\sigma}) \, f_j(x) \right] \prod_k g_k(\sigma_k|\hat{\boldsymbol{\sigma}}_k) \ , \quad (6.9)$$

while the number of expected events is

$$N = \sum_{i \in B} n_i \, s_i(\boldsymbol{\sigma}) + \mu \sum_{j \in S} n_j \, s_j(\boldsymbol{\sigma}) \ . \quad (6.10)$$

This final PDF is the extension of the previous model. It aims to study how unknown parameters can effect the significance in order evaluate its reliability. The considered effects do not contain shape modification of the single PDF contributions, since the systematics were introduced as simple scale factors. Anyway, each background channel has different scale factors so, the systematics can actually change the PDF of the observable x.

The method used for the significance evaluation of this model is exactly the same presented in section 6.2.2 and the test statistic spectra can be seen in Figure 6.9b. Thanks to the test statistic properties, the significance remained almost constant including the systematic uncertainties. Results with and without systematic uncertainty can be seen in Table 6.4.

It can be concluded that the event significance is about $3.5\,\sigma$. This result was proved to be stable including systematic uncertainty.

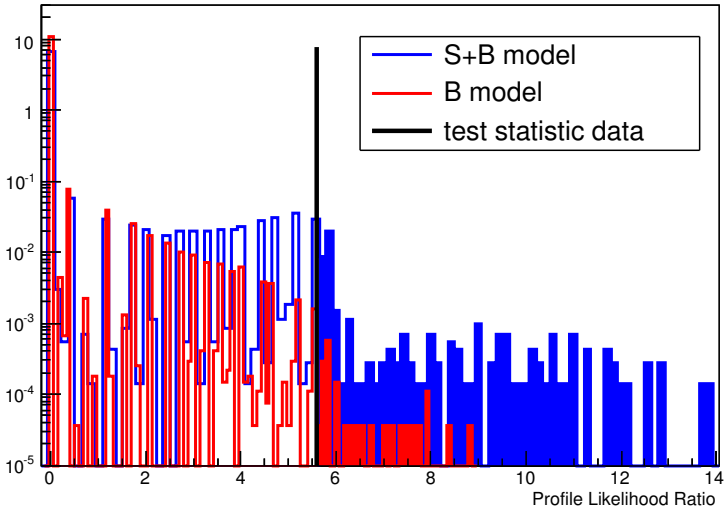

(a) Without systematic

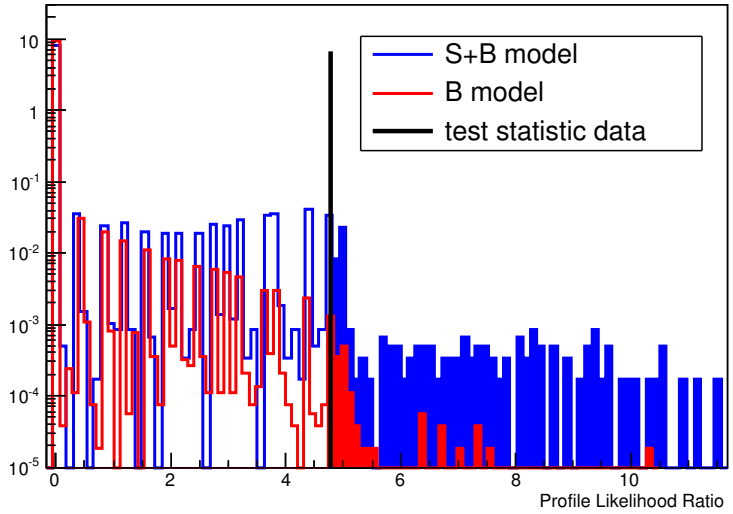

(b) Systematic included

Figure 6.9: *Hypothesis test samples.*

Chapter 7

Conclusions

The OPERA experiment operated between 2008 and 2012, in order to observe the ν_μ to ν_τ oscillation in a an almost pure ν_μ beam, the CNGS. During its operations, thousands of events were reconstructed in the detector target volume and more than five thousands had the primary vertex studied at the micrometer level. Such a precision allows the identification of very short decaying tracks typical of particles having mass around 2 GeV, like taus and charmed hadrons.

An event was observed with a very peculiar topology: it presents two secondary vertices within about 1 mm from the primary one. Possible interpretations include ν_τ interaction with charm production, or ν NC interaction with double charm production. OPERA considered negligible the observation of events with two secondary vertices and no analysis procedure was designed for such an observation. In fact, these rare processes were not even reproducible in the standard OPERA MC. Also, the OPERA analysis evaluates backgrounds in a way that can not be extended to more than one secondary vertex.

Thus, this dedicated analysis needed different software in all its components: from generators to signal–background discrimination. Some generators were studied in order to simulate all the relevant processes that could explain the event. Finally, two were used: GENIE and HERWIG.

The transport of primary particles was performed using GEANT4. This simulation propagates tracks through a portion of the OPERA detector and it was tested using data from a test beam beam dedicated to hadron interaction studies. The results were quite satisfactory and the newly developed simulation tool was successfully included in the two secondary vertices dedicated analysis.

Detector effects and OPERA standard procedure were not simulated, though their efficiencies were included in the analysis using data driven parameterizations. Finally a dedicated Monte Carlo production was obtained: it described in detail the properties of two secondary vertices events which

can be observed by the OPERA experiment. Out of the selected MC events, twelve variables were identified in order to discriminate between events with tau and a charmed particle against any other possibility.

The discrimination was performed using multivariate analysis methods typically used in high energy physics. This discrimination was prepared blindly with respect to the event properties, so that its evaluation would reveal the nature of the event. The event turned out to be very likely a ν_τ CC interaction with charm production. With respect to the non tau-charm hypothesis, the observed event has a very low probability, about 10^{-4}. This corresponds to a significance of $3.5\,\sigma$.

Appendices

Appendix A

Selected Tracks

The selection criteria described in chapter 5 are based on selection of 1pr-like and 2pr-like secondary vertices. It can happen in neutrino DIS interactions that an event has more one for each kind. It's also interesting to know what are the particles that produces secondary vertex, and their frequency. Of course, both number of secondary vertices and the kind of particles producing such vertices depend on the neutrino interaction process. Here, the plots summarizing these quantities are presented for each of the six channels listed in section 5.1.

For each channel, the top plot shows the number of 1pr-like and 2pr-like secondary vertices are shown together with their relative abundances. In the bottom plots, the particle producing the secondary vertex are presented in case of events with just one 1pr-like and one 2pr-like secondary vertices. For every plot, events with fragments are included and the weight due to location efficiency are not applied.

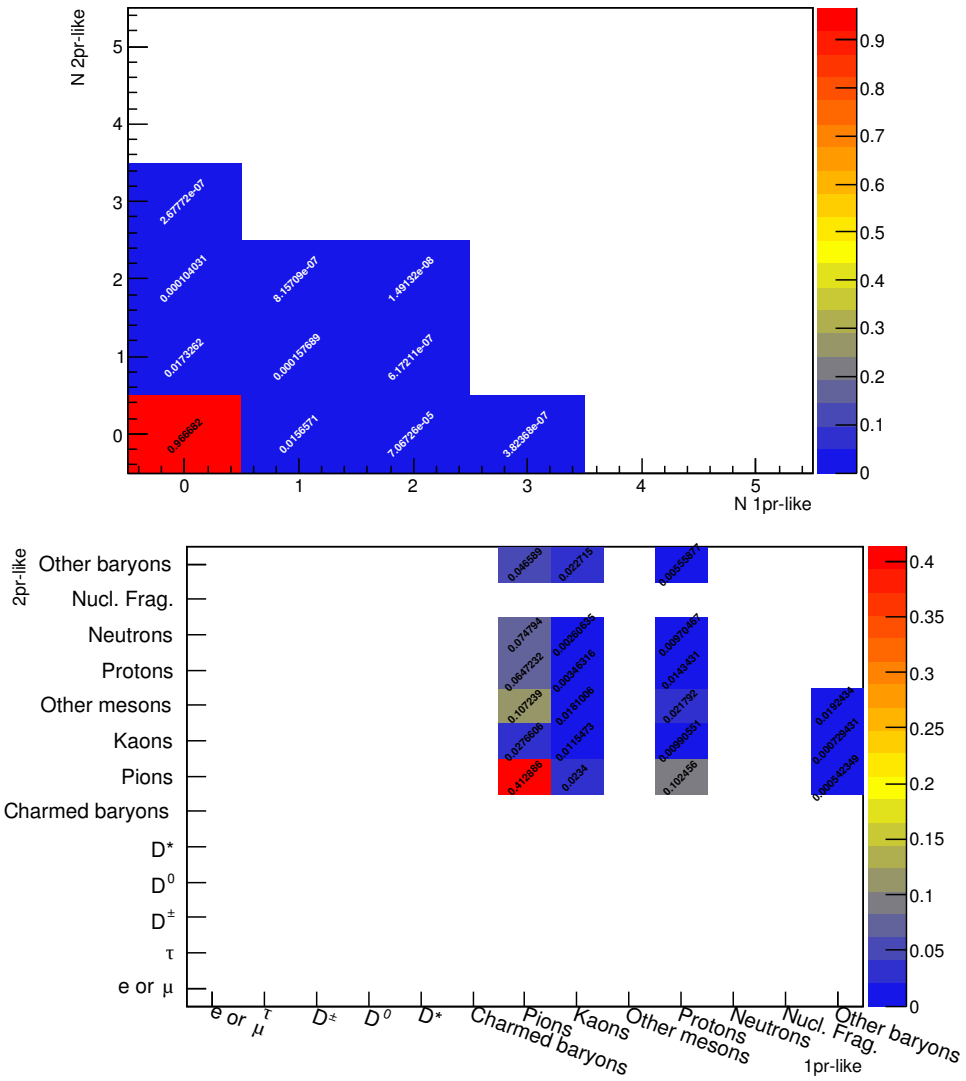

Figure A.1: *Particles selected by the selection described in section 5.5 in the ν_μ CC DIS sample.*

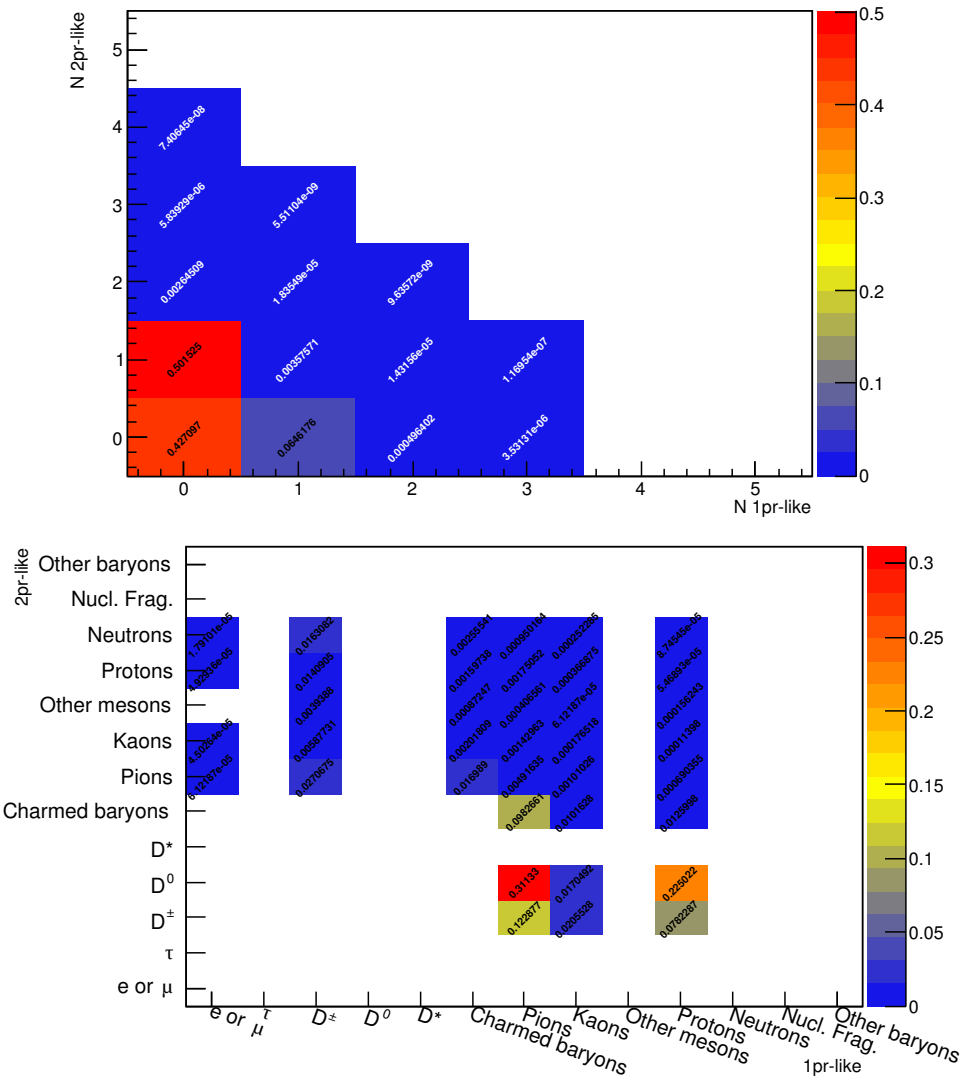

Figure A.2: *Particles selected by the selection described in section 5.5 in the ν_μ CC DIS with charm sample.*

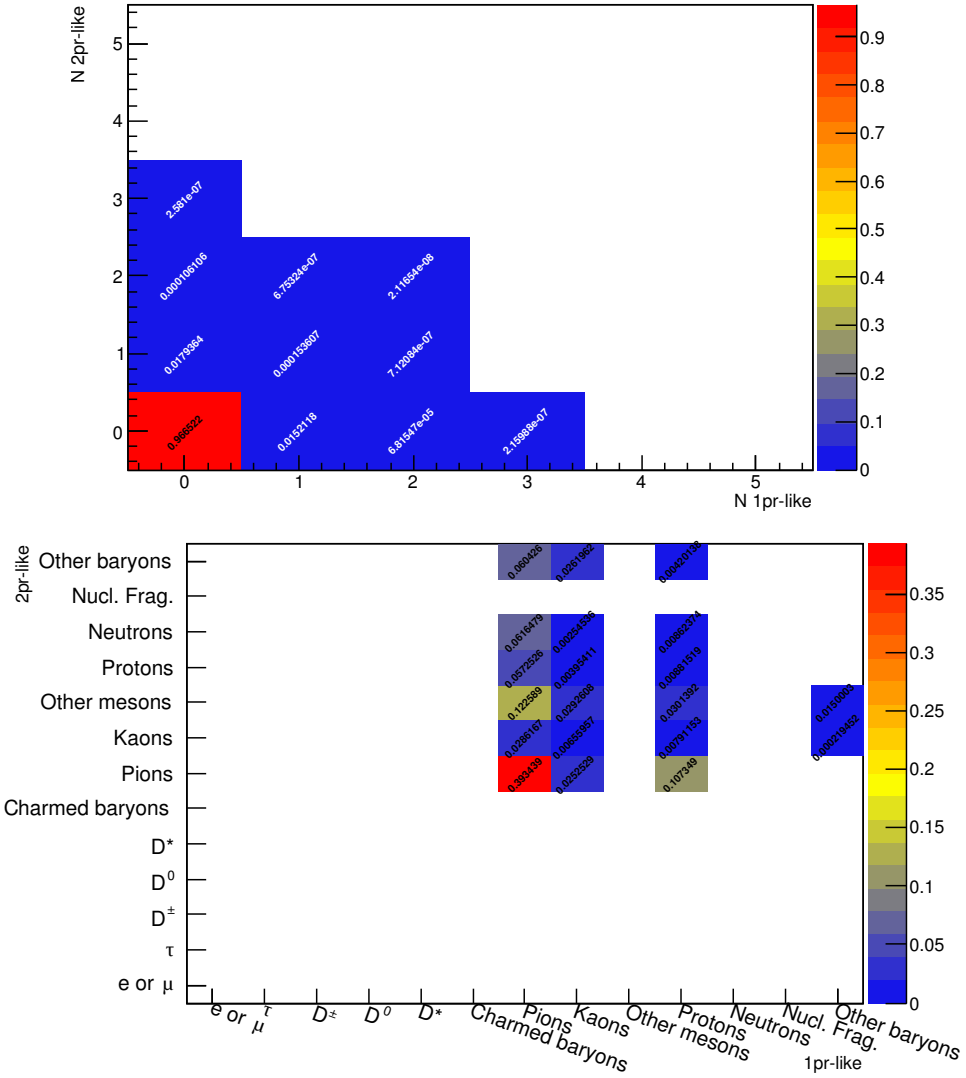

Figure A.3: *Particles selected by the selection described in section 5.5 in the ν NC DIS sample.*

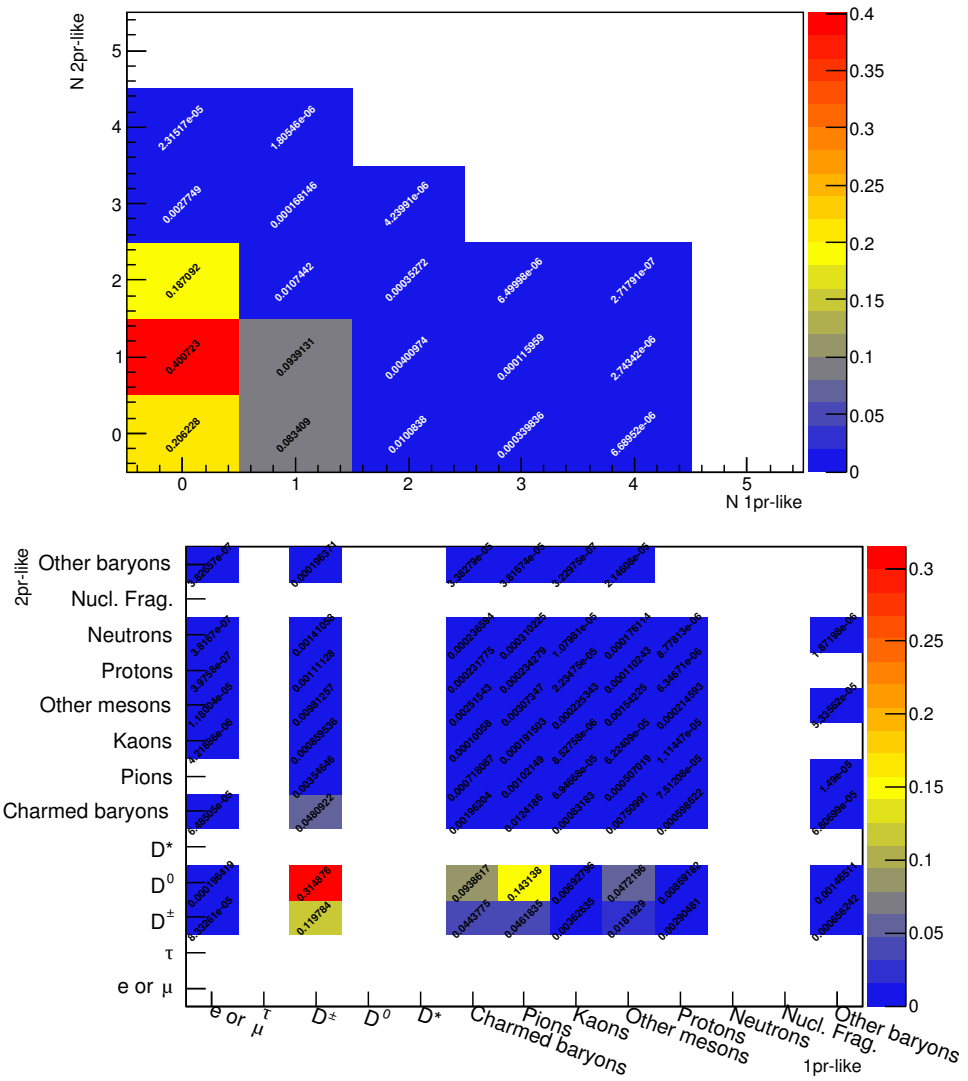

Figure A.4: *Particles selected by the selection described in section 5.5 in the ν NC DIS with charm pair sample.*

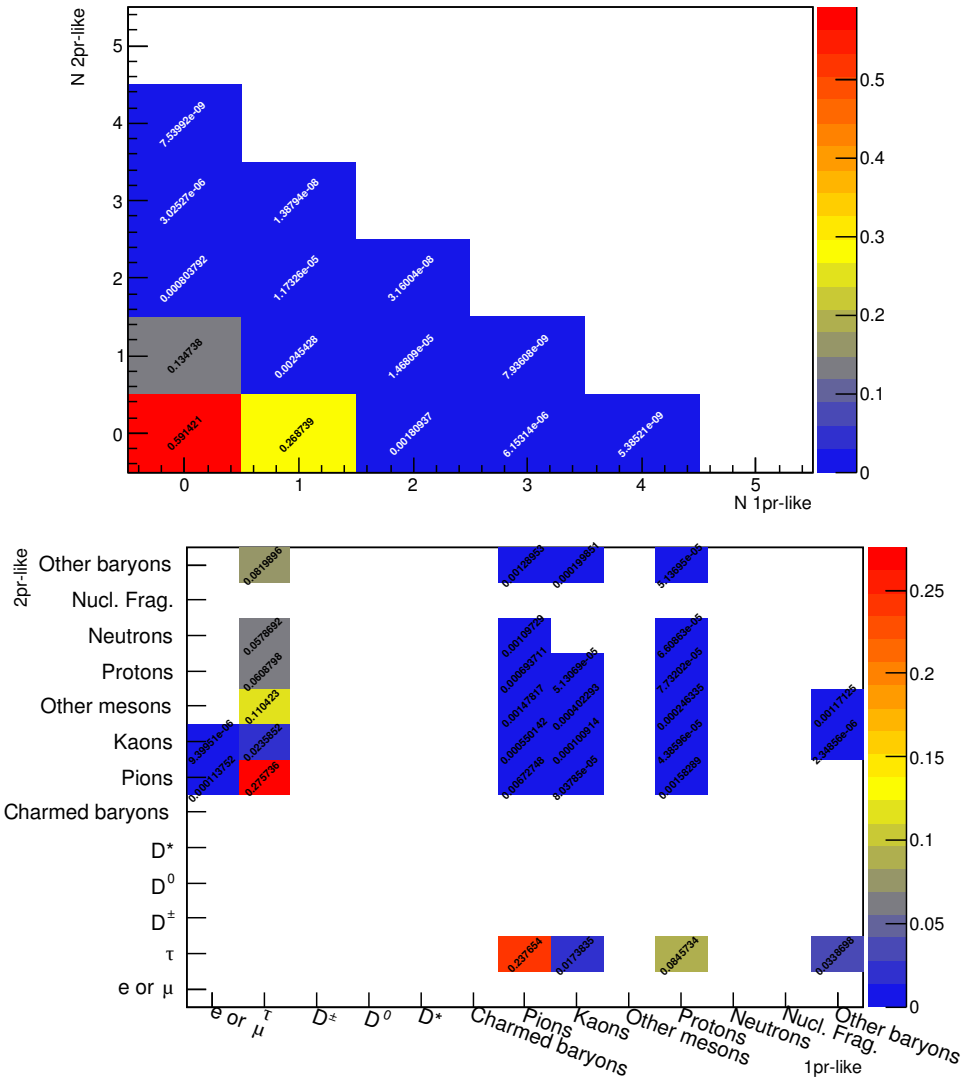

Figure A.5: *Particles selected by the selection described in section 5.5 in the ν_τ CC DIS sample.*

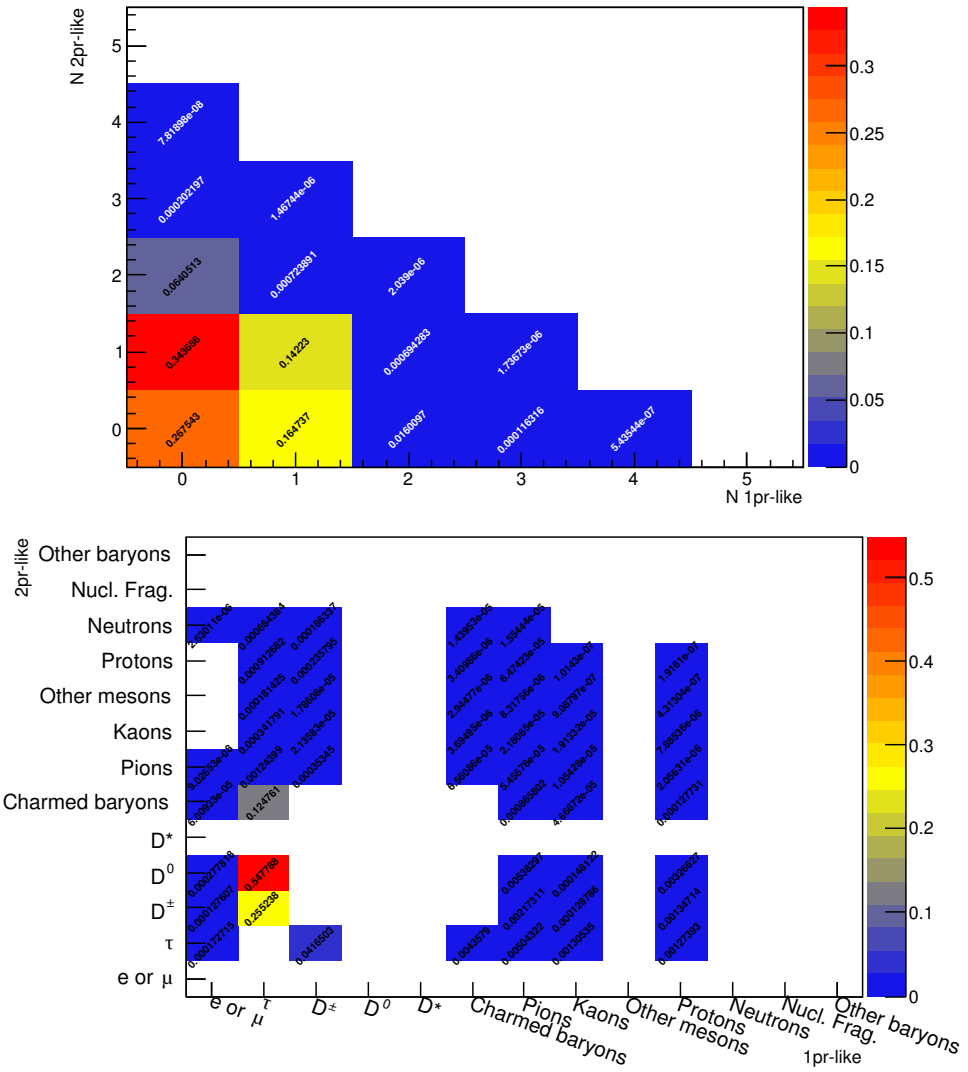

Figure A.6: *Particles selected by the selection described in section 5.5 in the ν_τ CC DIS with charm sample.*

Appendix B

Tau Selection

In chapter 6 only the search for ν_τ CC interaction with charm production was presented. Anyway, OPERA was designed to search only for tau events. Also for this purpose, the presence of a second secondary vertex reduces a lot the expected background, so the same MC sample presented in chapter 5 can be used to perform a τ search.

Here, the main analysis plots and tables are reported to describe the tau search in two secondary vertices events. The significance is evaluated using the same methods described in section 6.2. In this case, the classifiers performances are a bit worse since signal and background are more similar. Hence, also the significance is a bit lower, see Table B.2.

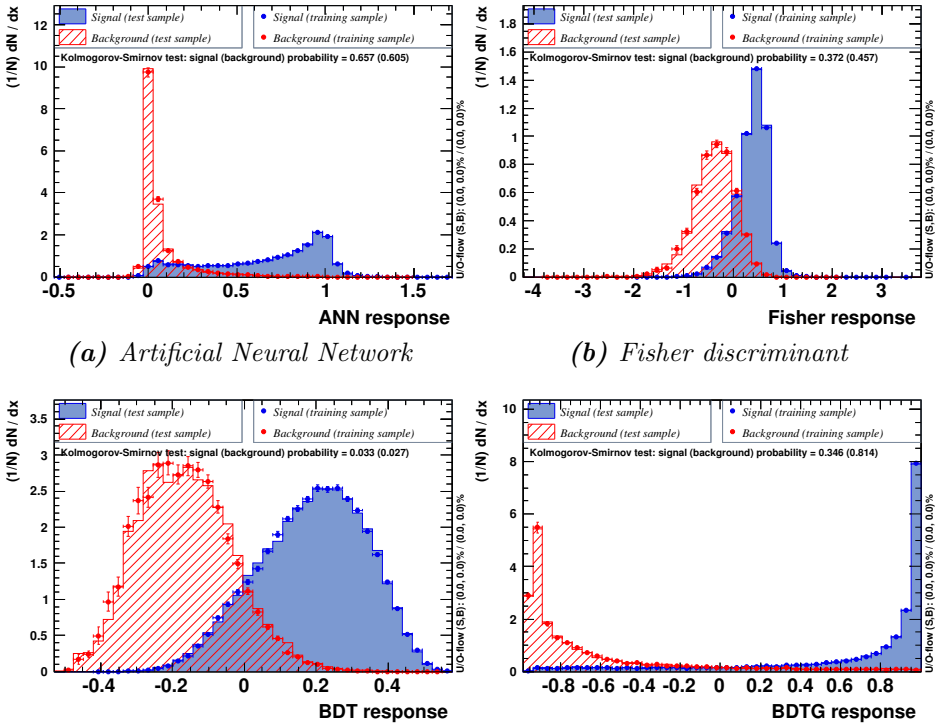

(a) Artificial Neural Network *(b) Fisher discriminant*

(c) BDT *(d) BDTG*

Figure B.1: *Discriminants overtraining test results.*

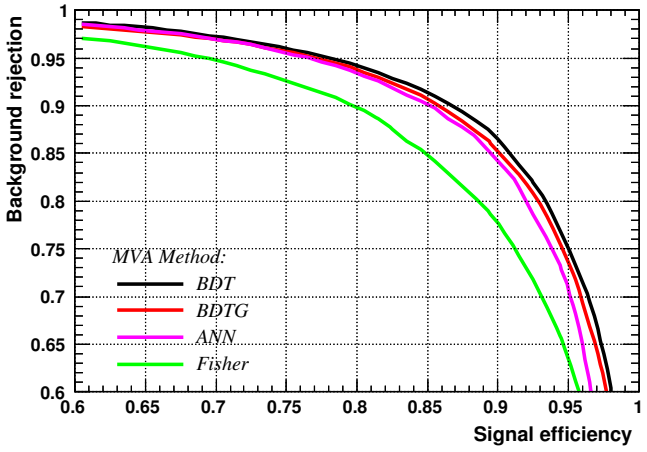

Figure B.2: *Background rejection against signal efficiency for all the trained classifiers.*

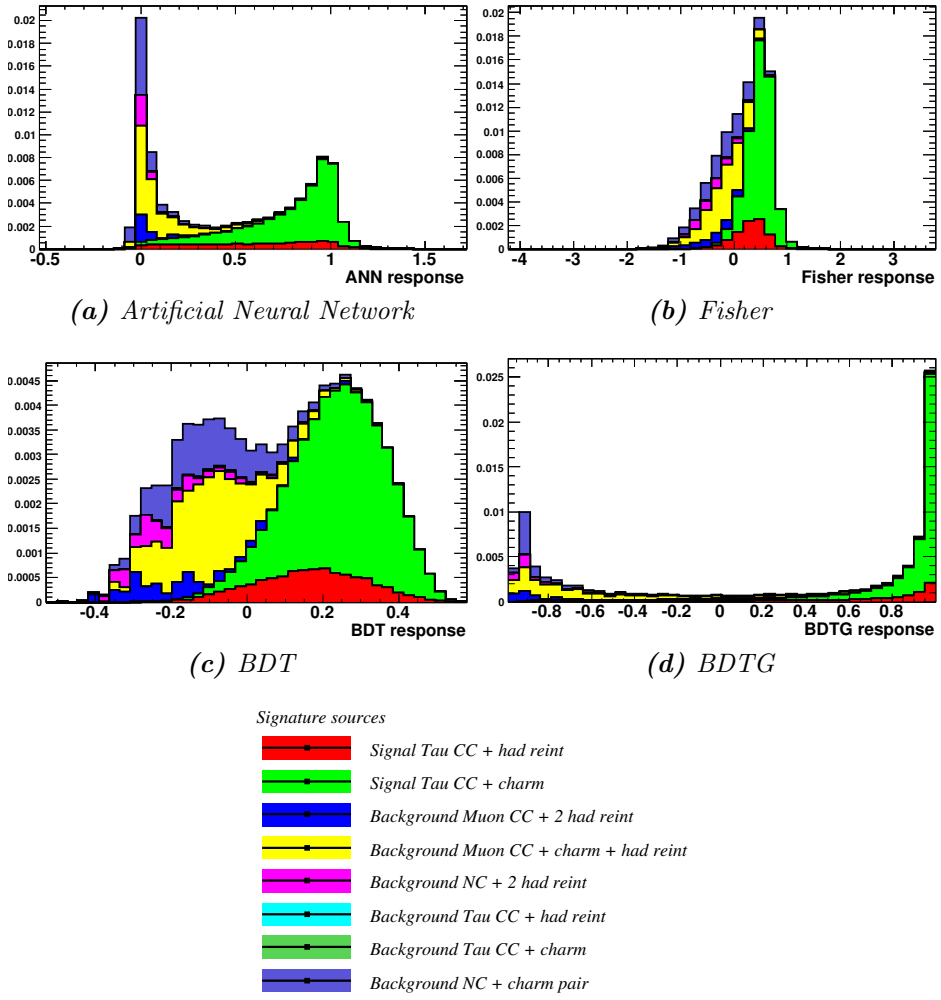

(a) Artificial Neural Network *(b) Fisher*

(c) BDT *(d) BDTG*

Figure B.3: *Classifier spectra. The auto-contamination components are small and hard to be visible*

Table B.1: *Probability of the interesting event for ANN and other classifiers algorithms.*

(a) *Event evaluation*

source	ANN	Fisher	BDT	BDTG
ν_μ CC DIS	0.96 %	0.80 %	0 %	0.30 %
ν_μ CC DIS + charm	0.89 %	3.85 %	0.58 %	0.59 %
ν NC DIS	0 %	0.23 %	0 %	0 %
ν NC DIS + $c\bar{c}$ pair	0.86 %	4.94 %	0.55 %	0.70 %
ν_τ CC DIS	8.37 %	12.77 %	9.21 %	8.33 %
ν_τ CC DIS + charm	88.92 %	77.34 %	89.66 %	90.08 %

(b) *Meta events*

source	ANN	Fisher	BDT	BDTG
ν_μ CC DIS	0.45 %	0.76 %	0.13 %	0.30 %
ν_μ CC DIS + charm	0.76 %	3.70 %	0.60 %	0.59 %
ν NC DIS	0 %	0.22 %	0 %	0 %
ν NC DIS + $c\bar{c}$ pair	0.99 %	4.80 %	0.68 %	0.70 %
ν_τ CC DIS	9.09 %	12.54 %	10.37 %	8.34 %
ν_τ CC DIS + charm	88.70 %	77.91 %	88.22 %	90.08 %

Table B.2: *CL and significance of the observed event with respect to the background only hypothesis.*

	CL (10^{-4})	n_σ
No systematics	4.8 ± 0.4	3.30 ± 0.02
With systematics	4.4 ± 0.3	3.33 ± 0.02

Bibliography

[1] Laurie M Brown. "The idea of the neutrino". In: *Physics Today* 31.9 (2008), pp. 23–28.

[2] C. L. Cowan Jr. et al. "Detection of the Free Neutrino: A Confirmation". In: *Science* 124 (July 1956), pp. 103–104. DOI: 10.1126/science.124.3212.103.

[3] James Chadwick. "Possible existence of a neutron". In: *Nature* 129.3252 (1932), p. 312.

[4] Y. Fukuda et al. "Evidence for Oscillation of Atmospheric Neutrinos". In: *Phys. Rev. Lett.* 81 (8 Aug. 1998), pp. 1562–1567. DOI: 10.1103/PhysRevLett.81.1562. URL: http://link.aps.org/doi/10.1103/PhysRevLett.81.1562.

[5] Serguei Chatrchyan et al. "A New Boson with a Mass of 125 GeV Observed with the CMS Experiment at the Large Hadron Collider". In: *Science* 338 (2012), pp. 1569–1575. DOI: 10.1126/science.1230816.

[6] M. Goldhaber, L. Grodzins, and A. W. Sunyar. "Helicity of Neutrinos". In: *Phys. Rev.* 109 (3 Feb. 1958), pp. 1015–1017. DOI: 10.1103/PhysRev.109.1015. URL: http://link.aps.org/doi/10.1103/PhysRev.109.1015.

[7] M. E. Peskin and D. V. Schroeder. *An Introduction to Quantum Field Theory*. Advanced book classics. Addison-Wesley Publishing Company, 1995. ISBN: 9780201503975. URL: https://books.google.hr/books?id=i35LALN0GosC.

[8] Carlo Giunti and Chung W. Kim. *Fundamentals of neutrino physics and astrophysics*. Oxford university press, 2007.

[9] J. Schechter and J. W. F. Valle. "Neutrino Decay and Spontaneous Violation of Lepton Number". In: *Phys. Rev.* D25 (1982), p. 774. DOI: 10.1103/PhysRevD.25.774.

[10] R. N. Mohapatra, A. Pérez-Lorenzana, and C. A. de S. Pires. "Type II seesaw and a gauge model for the bimaximal mixing explanation of neutrino puzzles". In: *Physics Letters B* 474.3–4 (2000), 355 –360. ISSN: 0370-2693. DOI: {http://dx.doi.org/10.1016/S0370-2693(00)00026-5}. URL: http://www.sciencedirect.com/science/article/pii/S0370269300000265.

[11] D. Ibanez, S. Morisi, and J. W. F. Valle. "Inverse tribimaximal type-III seesaw mechanism and lepton flavor violation". In: *Phys. Rev. D* 80 (5 Sept. 2009), p. 053015. DOI: 10.1103/PhysRevD.80.053015. URL: http://link.aps.org/doi/10.1103/PhysRevD.80.053015.

[12] S. M. Bilenky and S. T. Petcov. "Massive neutrinos and neutrino oscillations". In: *Rev. Mod. Phys.* 59 (3 July 1987), pp. 671–754. DOI: 10.1103/RevModPhys.59.671. URL: http://link.aps.org/doi/10.1103/RevModPhys.59.671.

[13] S. L. Glashow, J. Iliopoulos, and L. Maiani. "Weak Interactions with Lepton-Hadron Symmetry". In: *Phys. Rev. D* 2 (7 Oct. 1970), pp. 1285–1292. DOI: 10.1103/PhysRevD.2.1285. URL: http://link.aps.org/doi/10.1103/PhysRevD.2.1285.

[14] L. Wolfenstein. "Neutrino oscillations in matter". In: *Phys. Rev. D* 17 (9 May 1978), pp. 2369–2374. DOI: 10.1103/PhysRevD.17.2369. URL: http://link.aps.org/doi/10.1103/PhysRevD.17.2369.

[15] S. P. Mikheyev and A. Yu. Smirnov. "Resonant neutrino oscillations in matter". In: *Progress in Particle and Nuclear Physics* 23.0 (1989), pp. 41 –136. ISSN: 0146-6410. DOI: http://dx.doi.org/10.1016/0146-6410(89)90008-2. URL: http://www.sciencedirect.com/science/article/pii/0146641089900082.

[16] F. P. An et al. "Observation of Electron-Antineutrino Disappearance at Daya Bay". In: *Phys. Rev. Lett.* 108 (17 Apr. 2012), p. 171803. DOI: 10.1103/PhysRevLett.108.171803. URL: http://link.aps.org/doi/10.1103/PhysRevLett.108.171803.

[17] S.T. Petcov and M. Piai. "The LMA MSW solution of the solar neutrino problem, inverted neutrino mass hierarchy and reactor neutrino experiments". In: *Physics Letters B* 533.1–2 (2002), pp. 94 –106. ISSN: 0370-2693. DOI: http://dx.doi.org/10.1016/S0370-2693(02)01591-5. URL: http://www.sciencedirect.com/science/article/pii/S0370269302015915.

[18] Stephen F. King and Christoph Luhn. "Neutrino mass and mixing with discrete symmetry". In: *Reports on Progress in Physics* 76.5 (2013), p. 056201. URL: http://stacks.iop.org/0034-4885/76/i=5/a=056201.

[19] S. Abe et al. "Precision Measurement of Neutrino Oscillation Parameters with KamLAND". In: *Phys. Rev. Lett.* 100 (22 June 2008), p. 221803. DOI: 10.1103/PhysRevLett.100.221803. URL: http://link.aps.org/doi/10.1103/PhysRevLett.100.221803.

[20] F. P. An et al. "Independent measurement of the neutrino mixing angle θ_{13} via neutron capture on hydrogen at Daya Bay". In: *Phys. Rev. D* 90 (7 Nov. 2014), p. 071101. DOI: 10.1103/PhysRevD.90.071101. URL: http://link.aps.org/doi/10.1103/PhysRevD.90.071101.

[21] Liang Zhan et al. "Determination of the neutrino mass hierarchy at an intermediate baseline". In: *Phys. Rev. D* 78 (11 Dec. 2008), p. 111103. DOI: 10.1103/PhysRevD.78.111103. URL: http://link.aps.org/doi/10.1103/PhysRevD.78.111103.

[22] R. N. Cahn et al. "White Paper: Measuring the Neutrino Mass Hierarchy". In: (2013). arXiv: 1307.5487 [hep-ex].

[23] John N. Bahcall, Aldo M. Serenelli, and Sarbani Basu. "New Solar Opacities, Abundances, Helioseismology, and Neutrino Fluxes". In: *The Astrophysical Journal Letters* 621.1 (2005), p. L85. URL: http://stacks.iop.org/1538-4357/621/i=1/a=L85.

[24] F. Kaether et al. "Reanalysis of the GALLEX solar neutrino flux and source experiments". In: *Phys. Lett.* B685 (2010), pp. 47–54. DOI: 10.1016/j.physletb.2010.01.030. arXiv: 1001.2731 [hep-ex].

[25] K. Hirata et al. "Observation of ^{8}B solar neutrinos in the Kamiokande-II detector". In: *Phys. Rev. Lett.* 63 (1 July 1989), pp. 16–19. DOI: 10.1103/PhysRevLett.63.16. URL: http://link.aps.org/doi/10.1103/PhysRevLett.63.16.

[26] J. Boger et al. "The Sudbury Neutrino Observatory". In: *Nuclear Instruments and Methods in Physics Research Section A: Accelerators, Spectrometers, Detectors and Associated Equipment* 449.1-2 (2000), pp. 172 –207. ISSN: 0168-9002. DOI: http://dx.doi.org/10.1016/S0168-9002(99)01469-2. URL: http://www.sciencedirect.com/science/article/pii/S0168900299014692.

[27] N. Barros. "Final results from SNO". In: *Nucl.Phys.Proc.Suppl.* 237-238 (2013), pp. 107–110. DOI: 10.1016/j.nuclphysbps.2013.04.069.

[28] G. Bellini et al. "Final results of Borexino Phase-I on low-energy solar neutrino spectroscopy". In: *Phys. Rev. D* 89 (11 June 2014), p. 112007. DOI: 10.1103/PhysRevD.89.112007. URL: http://link.aps.org/doi/10.1103/PhysRevD.89.112007.

[29] G. Bellini et al. "Neutrinos from the primary proton–proton fusion process in the Sun". In: *Nature* 512.7515 (2014), pp. 383–386. DOI: 10.1038/nature13702.

[30] J. Hosaka et al. "Three flavor neutrino oscillation analysis of atmospheric neutrinos in Super-Kamiokande". In: *Phys. Rev. D* 74 (3 Aug. 2006), p. 032002. DOI: 10.1103/PhysRevD.74.032002. URL: http://link.aps.org/doi/10.1103/PhysRevD.74.032002.

[31] M. Ambrosio et al. "Low-energy atmospheric muon neutrinos in MACRO". In: *Phys. Lett.* B478 (2000), pp. 5–13. DOI: 10.1016/S0370-2693(00)00267-7. arXiv: hep-ex/0001044 [hep-ex].

[32] P. Adamson et al. "Combined Analysis of ν_μ Disappearance and $\nu_\mu \to \nu_e$ Appearance in MINOS Using Accelerator and Atmospheric Neutrinos". In: *Phys. Rev. Lett.* 112 (19 May 2014), p. 191801. DOI: 10.1103/PhysRevLett.112.191801. URL: http://link.aps.org/doi/10.1103/PhysRevLett.112.191801.

[33] Steinbrink, Nicholas and others. "Neutrino mass sensitivity by MAC-E-Filter based time-of-flight spectroscopy with the example of KATRIN". In: *New Journal of Physics* 15.11 (2013), p. 113020. URL: http://stacks.iop.org/1367-2630/15/i=11/a=113020.

[34] K. A. Olive et al. "Review of Particle Physics". In: *Chin. Phys.* C38 (2014), p. 090001. DOI: 10.1088/1674-1137/38/9/090001.

[35] Shaun A. Thomas, Filipe B. Abdalla, and Ofer Lahav. "Upper Bound of 0.28 eV on Neutrino Masses from the Largest Photometric Redshift Survey". In: *Phys. Rev. Lett.* 105 (3 July 2010), p. 031301. DOI: 10.1103/PhysRevLett.105.031301. URL: http://link.aps.org/doi/10.1103/PhysRevLett.105.031301.

[36] Gary C. Hill. "First detection of high-energy astrophysical neutrinos with IceCube". In: *AIP Conf. Proc.* 1666 (2015), p. 040001. DOI: 10.1063/1.4915550.

[37] A. N. Ivanov et al. "Deficit of reactor antineutrinos at distances smaller than 100 m and inverse β decay". In: *Phys. Rev. C* 88 (5 Nov. 2013), p. 055501. DOI: 10.1103/PhysRevC.88.055501. URL: http://link.aps.org/doi/10.1103/PhysRevC.88.055501.

[38] Carlo Giunti and Marco Laveder. "Statistical significance of the gallium anomaly". In: *Phys. Rev. C* 83 (6 June 2011), p. 065504. DOI: 10.1103/PhysRevC.83.065504. URL: http://link.aps.org/doi/10.1103/PhysRevC.83.065504.

[39] A. Aguilar et al. "Evidence for neutrino oscillations from the observation of $\overline{\nu}_e$ appearance in a $\overline{\nu}_\mu$ beam". In: *Phys. Rev. D* 64 (11 Nov. 2001), p. 112007. DOI: 10.1103/PhysRevD.64.112007. URL: http://link.aps.org/doi/10.1103/PhysRevD.64.112007.

[40] K. Kodama et al. "Final tau-neutrino results from the DONuT experiment". In: *Phys. Rev. D* 78 (5 Sept. 2008), p. 052002. DOI: 10.1103/PhysRevD.78.052002. URL: http://link.aps.org/doi/10.1103/PhysRevD.78.052002.

[41] E Eskut et al. "The CHORUS experiment to search for $\nu_\mu \to \nu_\tau$ oscillation". In: *Nuclear Instruments and Methods in Physics Research Section A: Accelerators, Spectrometers, Detectors and Associated Equipment* 401.1 (1997), pp. 7–44.

[42] E. Eskut et al. "Final results on nu(mu) —> nu(tau) oscillation from the CHORUS experiment". In: *Nucl. Phys.* B793 (2008), pp. 326–343. DOI: 10.1016/j.nuclphysb.2007.10.023. arXiv: 0710.3361 [hep-ex].

[43] K. Abe et al. "Evidence for the Appearance of Atmospheric Tau Neutrinos in Super-Kamiokande". In: *Phys. Rev. Lett.* 110 (18 May 2013), p. 181802. DOI: 10.1103/PhysRevLett.110.181802. URL: http://link.aps.org/doi/10.1103/PhysRevLett.110.181802.

[44] N Ushida et al. "Experimental details on lifetime measurements of neutrino-produced charmed particles in a tagged emulsion spectrometer". In: *Nuclear Instruments and Methods in Physics Research* 224.1 (1984), pp. 50–64.

[45] P. Annis et al. "Observation of neutrino induced diffractive D_s^{*+} production and subsequent decay $D_s^{*+} \to D_s^+ \to \tau^+ \to \mu^+$". In: *Phys. Lett. B* 435.CERN-EP-98-087. 3-4 (May 1998), 458–464. 6 p. URL: http://cds.cern.ch/record/359239.

[46] Giovanni De Lellis, Pasquale Migliozzi, and Pietro Santorelli. "Charm physics with neutrinos". In: *Physics reports* 399.5 (2004), pp. 227–320.

[47] A. Kayis-Topaksu et al. "Measurement of charm production in neutrino charged-current interactions". In: *New J. Phys.* 13 (2011), p. 093002. DOI: 10.1088/1367-2630/13/9/093002. arXiv: 1107.0613 [hep-ex].

[48] M. Guler et al. "OPERA: An appearance experiment to search for $\nu_\mu \longleftrightarrow \nu_\tau$ oscillations in the CNGS beam". In: *Experimental proposal CERN-SPSC-2000-028* (2000).

[49] N. Agafonova et al. "Discovery of τ Neutrino Appearance in the CNGS Neutrino Beam with the OPERA Experiment". In: *Phys. Rev. Lett.* 115 (12 Sept. 2015), p. 121802. DOI: 10.1103/PhysRevLett.115.121802. URL: http://link.aps.org/doi/10.1103/PhysRevLett.115.121802.

[50] K. Elsener, ed. *The CERN neutrino beam to Gran Sasso (NGS) - Conceptual technical design*. CERN - Service d'information scientifique, May 1998. URL: http://proj-cngs.web.cern.ch/proj-cngs/.

[51] R. Acquafredda et al. "The OPERA experiment in the CERN to Gran Sasso neutrino beam". In: *JINST* 4 (2009), P04018. DOI: 10.1088/1748-0221/4/04/P04018.

[52] A. Lucotte et al. "A front-end read out chip for the OPERA scintillator tracker". In: *Nucl. Instrum. Meth.* A521 (2004), pp. 378–392. DOI: 10.1016/j.nima.2003.10.104.

[53] N. Agafonova et al. "Procedure for short-lived particle detection in the OPERA experiment and its application to charm decays". In: *Eur. Phys. J. C* 74.8 (2014), p. 2986. DOI: 10.1140/epjc/s10052-014-2986-0. URL: http://dx.doi.org/10.1140/epjc/s10052-014-2986-0.

[54] Matteo Tenti. "Electron identification and reconstruction with the OPERA ECC bricks and search for $\nu_\mu \to \nu_e$ oscillations". PhD Thesis. Università degli studi di Bologna, 2012. URL: http://www.bo.infn.it/opera/docs/phd_thesis-BO-2012-tenti.pdf.

[55] R. Acquafredda et al. "The OPERA experiment in the CERN to Gran Sasso neutrino beam". In: *JINST* 4 (2009), P04018. DOI: 10.1088/1748-0221/4/04/P04018.

[56] A. Anokhina et al. "Study of the effects induced by lead on the emulsion films of the OPERA experiment". In: *JINST* 3 (2008), P07002. DOI: 10.1088/1748-0221/3/07/P07002. arXiv: 0805.0123 [physics.ins-det].

[57] A. Anokhina et al. "Emulsion sheet doublets as interface trackers for the OPERA experiment". In: *JINST* 3 (2008), P07005. DOI: 10.1088/1748-0221/3/07/P07005. arXiv: 0804.1985 [physics.ins-det].

[58] L. Arrabito et al. "Hardware performance of a scanning system for high speed analysis of nuclear emulsions". In: *Nuclear Instruments and Methods in Physics Research Section A: Accelerators, Spectrometers, Detectors and Associated Equipment* 568.2 (2006), pp. 578 –587. ISSN: 0168-9002. DOI: http://dx.doi.org/10.1016/j.nima.2006.06.072. URL: http://www.sciencedirect.com/science/article/pii/S0168900206012198.

[59] Gabriele Sirri. "Automatic scanning of emulsion films for the OPERA experiment". PhD Thesis. Università degli studi di Bologna, 2003. URL: http://www.bo.infn.it/opera/docs/phd_thesis-BO-2003_06_05-sirri.pdf.

[60] L. Arrabito et al. "Track reconstruction in the emulsion-lead target of the OPERA experiment using the ESS microscope". In: *JINST* 2 (2007), P05004. arXiv: 0705.3102 [physics.ins-det].

[61] N. Armenise et al. "High-speed particle tracking in nuclear emulsion by last-generation automatic microscopes". In: *Nuclear Instruments and Methods in Physics Research Section A: Accelerators, Spectrometers, Detectors and Associated Equipment* 551.2–3 (2005), pp. 261 –270. ISSN: 0168-9002. DOI: http://dx.doi.org/10.1016/j.nima.2005.06.072. URL: http://www.sciencedirect.com/science/article/pii/S0168900205013240.

[62] A. Bertolin et Ngoc-Tiem Tran. *OpCarac: an algorithm for the classification of the neutrino interactions recorded by the OPERA experiment.* Tech. rep. OPERA note, 2009.

[63] N. Agafonova et al. "Study of neutrino interactions with the electronic detectors of the OPERA experiment". In: *New J. Phys.* 13 (2011), p. 053051. DOI: 10.1088/1367-2630/13/5/053051. arXiv: 1102.1882 [hep-ex].

[64] Fabio Pupilli. "Search for ν_τ interactions in the OPERA experiment". PhD thesis. Università degli studi dell'Aquila, Jan. 2011.

[65] E. Barbuto et al. "Atmospheric muon flux measurements at the external site of the Gran Sasso Lab". In: *Nuclear Instruments and Methods in Physics Research Section A: Accelerators, Spectrometers, Detectors and Associated Equipment* 525.3 (2004), pp. 485 –495. ISSN: 0168-9002. DOI: http://dx.doi.org/10.1016/j.nima.2004.01.078. URL: http://www.sciencedirect.com/science/article/pii/S0168900204002426.

[66] N. Agafonova et al. "Momentum measurement by the Multiple Coulomb Scattering method in the OPERA lead emulsion target". In: *New J. Phys.* 14 (2012), p. 013026. DOI: 10.1088/1367-2630/14/1/013026. arXiv: 1106.6211 [physics.ins-det].

[67] Gerald R. Lynch and Orin I. Dahl. "Approximations to multiple Coulomb scattering". In: *Nuclear Instruments and Methods in Physics Research Section B: Beam Interactions with Materials and Atoms* 58.1 (1991), pp. 6 –10. ISSN: 0168-583X. DOI: http://dx.doi.org/10.1016/0168-583X(91)95671-Y. URL: http://www.sciencedirect.com/science/article/pii/0168583X9195671Y.

[68] Antonia Di Crescenzo. "Search for $\nu_\mu \to \nu_\tau$ oscillations in the OPERA experiment". PhD Thesis. Università degli studi di Napoli "Federico II", Mar. 2013.

[69] N. Agafonova et al. "Procedure for short-lived particle detection in the OPERA experiment and its application to charm decays". In: *Eur. Phys. J. C* 74.8 (2014), p. 2986. DOI: 10.1140/epjc/s10052-014-2986-0. URL: http://dx.doi.org/10.1140/epjc/s10052-014-2986-0.

[70] E.L. Berger et al. "The minimum invariant mass – A technique for heavy quark searches at collider energy". In: *Physics Letters B* 140.3–4 (1984), pp. 259 –263. ISSN: 0370-2693. DOI: http://dx.doi.org/10.1016/0370-2693(84)90931-6. URL: http://www.sciencedirect.com/science/article/pii/0370269384909316.

[71] N. Agafonova et al. "Observation of a first ν_τ candidate in the OPERA experiment in the CNGS beam". In: *Phys. Lett.* B691 (2010), pp. 138–145. DOI: 10.1016/j.physletb.2010.06.022. arXiv: 1006.1623 [hep-ex].

[72] N. Agafonova et al. "Observation of tau neutrino appearance in the CNGS beam with the OPERA experiment". In: *PTEP* 2014.10 (2014), p. 101C01. DOI: 10.1093/ptep/ptu132. arXiv: 1407.3513 [hep-ex].

[73] N. Agafonova et al. "Evidence for $\nu_\mu \to \nu_\tau$ appearance in the CNGS neutrino beam with the OPERA experiment". In: *Phys. Rev.* D89.5 (2014), p. 051102. DOI: 10.1103/PhysRevD.89.051102. arXiv: 1401.2079 [hep-ex].

[74] N. Agafonova et al. "New results on $\nu_\mu \to \nu_\tau$ appearance with the OPERA experiment in the CNGS beam". In: *JHEP* 11 (2013). [Erratum: JHEP04,014(2014)], p. 036. DOI: 10.1007/JHEP11(2013)036, 10.1007/JHEP04(2014)014. arXiv: 1308.2553 [hep-ex].

[75] A. Alexandrov, V. Tioukov, and M. Vladymyrov. "Further progress for a fast scanning of nuclear emulsions with Large Angle Scanning System". In: *Journal of Instrumentation* 9.02 (2014), p. C02034. URL: http://stacks.iop.org/1748-0221/9/i=02/a=C02034.

[76] M. J. Berger et al. *Stopping-Power and Range Tables for Electrons, Protons, and Helium Ions*. NIST, Physical Measurement Laboratory. 2009. URL: http://www.nist.gov/pml/data/star/.

[77] D. Ashery et al. "True absorption and scattering of pions on nuclei". In: *Phys. Rev. C* 23 (5 May 1981), pp. 2173–2185. DOI: 10.1103/PhysRevC.23.2173. URL: http://link.aps.org/doi/10.1103/PhysRevC.23.2173.

[78] R. A. Giannelli et al. "Multiproton final states in positive pion absorption below the $\Delta(1232)$ resonance". In: *Phys. Rev. C* 61 (5 Apr. 2000), p. 054615. DOI: 10.1103/PhysRevC.61.054615. URL: http://link.aps.org/doi/10.1103/PhysRevC.61.054615.

[79] Chiara Sirignano et al. *Electromagnetic showers study by detailed image analysis*. 2015. URL: https://indico.cern.ch/event/365741/session/4/contribution/3/attachments/727206/997866/shower_sirignano_15_3_2015.pdf.

[80] A. Kayis-Topaksu et al. "Associated Charm Production in Neutrino-Nucleus Interactions". In: *Eur. Phys. J.* C52 (2007), pp. 543–552. DOI: 10.1140/epjc/s10052-007-0410-8. arXiv: 0708.2820 [hep-ex].

[81] Hirokazu Ishida et al. "Study of hadron interactions in a lead–emulsion target". In: *PTEP* 2014.9 (2014), p. 093C01. DOI: 10.1093/ptep/ptu119. arXiv: 1408.0386 [physics.ins-det].

[82] A. Ferrari et al. "FLUKA: a multi-particle transport code". In: *CERN 2005-10 (2005), INFN/TC 05/11, SLAC-R-773.*

[83] T. T. Böhlen et al. "The FLUKA Code: Developments and Challenges for High Energy and Medical Applications". In: *Nuclear Data Sheets* 120 (June 2014), pp. 211–214. DOI: 10.1016/j.nds.2014.07.049.

[84] K. Morishima and T. Nakano. "Development of a new automatic nuclear emulsion scanning system, S-UTS, with continuous 3D tomographic image read-out". In: *Journal of Instrumentation* 5.04 (2010), P04011. URL: http://stacks.iop.org/1748-0221/5/i=04/a=P04011.

[85] T. Fukuda et al. "Automatic scanning of nuclear emulsions with wide-angle acceptance for nuclear fragment detection". In: *Journal of Instrumentation* 8.01 (2013), P01023. URL: http://stacks.iop.org/1748-0221/8/i=01/a=P01023.

[86] S. Agostinelli, J. Allison, K. Amako, et al. "Geant4–a simulation toolkit". In: *Nuclear Instruments and Methods in Physics Research Section A: Accelerators, Spectrometers, Detectors and Associated Equipment* 506.3 (2003), pp. 250 –303. ISSN: 0168-9002. DOI: http://dx.doi.org/10.1016/S0168-9002(03)01368-8. URL: http://www.sciencedirect.com/science/article/pii/S0168900203013688.

[87] J. Allison et al. "Geant4 developments and applications". In: *Nuclear Science, IEEE Transactions on* 53.1 (Feb. 2006), pp. 270–278. ISSN: 0018-9499. DOI: 10.1109/TNS.2006.869826.

[88] T. Sjöstrand, G. Altarelli, et al. "Z physics at LEP 1". In: *CERN Report CERN-89-08.* Vol. 3. CERN Geneva, 1989, p. 143.

[89] Rene Brun and Fons Rademakers. "ROOT – An object oriented data analysis framework". In: *Nuclear Instruments and Methods in Physics Research Section A: Accelerators, Spectrometers, Detectors and Associated Equipment* 389.1–2 (1997). New Computing Techniques in Physics Research V, pp. 81 –86. ISSN: 0168-9002. DOI: 10.1016/S0168-9002(97)00048-X. URL: http://root.cern.ch/.

[90] Silvia Pascoli. *Theory and Phenomenology of neutrino oscillations.* BUSSTEPP. Sept. 2013. URL: http://www.phys.susx.ac.uk/~sj209/busstepp13/lectures/L1_Neutrinooscill.pdf.

[91] C. Andreopoulos et al. "The GENIE Neutrino Monte Carlo Generator". In: *Nucl. Instrum. Meth.* A614 (2010), pp. 87–104. DOI: 10.1016/j.nima.2009.12.009. arXiv: 0905.2517 [hep-ph].

[92] G. Corcella et al. "HERWIG 6: An Event generator for hadron emission reactions with interfering gluons (including supersymmetric processes)". In: *JHEP* 01 (2001), p. 010. DOI: 10.1088/1126-6708/2001/01/010. arXiv: hep-ph/0011363 [hep-ph].

[93] Torbjorn Sjostrand, Stephen Mrenna, and Peter Z. Skands. "PYTHIA 6.4 Physics and Manual". In: *JHEP* 05 (2006), p. 026. DOI: 10.1088/1126-6708/2006/05/026. arXiv: hep-ph/0603175 [hep-ph].

[94] S. Kretzer and M. H. Reno. "Tau neutrino deep inelastic charged current interactions". In: *Phys. Rev. D* 66 (11 Dec. 2002), p. 113007. DOI: 10.1103/PhysRevD.66.113007. URL: http://link.aps.org/doi/10.1103/PhysRevD.66.113007.

[95] J. Meija et al. "Isotopic compositions of the elements 2013". In: *Pure and Applied Chemistry* 88 (2016).

[96] Alessandro Bertolin. *CNGS neutrino beam direction as measured by the OPERA Electronic Detectors*. OPERA internal note 163. Aug. 2013.

[97] Andreas Hoecker et al. "TMVA: Toolkit for Multivariate Data Analysis". In: *PoS* ACAT (2007), p. 040. arXiv: physics/0703039.

[98] Yoav Freund and Robert E Schapire. "A Decision-Theoretic Generalization of On-Line Learning and an Application to Boosting". In: *Journal of Computer and System Sciences* 55.1 (1997), pp. 119 –139. ISSN: 0022-0000. DOI: http://dx.doi.org/10.1006/jcss.1997.1504. URL: http://www.sciencedirect.com/science/article/pii/S002200009791504X.

[99] Ronald A Fisher. "The use of multiple measurements in taxonomic problems". In: *Annals of eugenics* 7.2 (1936), pp. 179–188.

[100] AN Kolmogorov. "Sulla determinazione empirica delle leggi di probabilita". In: *Giorn. Ist. Ital. Attuari* 4 (1933), pp. 1–11.

[101] Wouter Verkerke and David P. Kirkby. "The RooFit toolkit for data modeling". In: *eConf* C0303241 (2003). [,186(2003)], MOLT007. arXiv: physics/0306116 [physics].

[102] R. L. Berger and G. Casella. *Statistical Inference*. Ed. by Duxbury Press. Second Edition. 2001.

[103] Gioacchino Ranucci. "The profile likelihood ratio and the look elsewhere effect in high energy physics". In: *Nuclear Instruments and Methods in Physics Research Section A: Accelerators, Spectrometers, Detectors and Associated Equipment* 661.1 (2012), pp. 77 –85. ISSN: 0168-9002. DOI: http://dx.doi.org/10.1016/j.nima.2011.09.047. URL: http://www.sciencedirect.com/science/article/pii/S0168900211018420.

[104] Glen Cowan et al. "Asymptotic formulae for likelihood-based tests of new physics". In: *The European Physical Journal C* 71.2 (2011), pp. 1–19.

[105] Yu Seon Jeong and Mary Hall Reno. "Tau neutrino and antineutrino cross sections". In: *Phys. Rev.* D82 (2010), p. 033010. DOI: 10.1103/PhysRevD.82.033010. arXiv: 1007.1966 [hep-ph].

List of Figures

List of Tables

Acknowledgments

Dear reader,

thanks for having read my thesis to this very end. I want you to be aware of all the people involved in this work, of all the people who have meant something to me during my PhD.

First of all I like to thanks the Bologna-Padova OPERA group, especially Alessandro, Chiara , Eduardo and Gabriele. Thanks for your suggestions, the discussion we had, the travels and the happy moments we shared all together. Edu, Chiara and Gabriele deserve a special mention: this thesis wouldn't have been possible without you.

Among the other OPERA members, I need to thank Matteo, Nicoletta and Giuliana for being the most patient travel companions ever and Budimir for having provided me a wonderful home in Zagreb.

Thanks to Kate for being my office mate for more than two years and never complaining about me being loud. You taught me a lot and you made the office time always pleasant.

Thanks to all the people whom I had the pleasure to sing and make music with. In particular, thanks to Ignatio for the opportunities he gave me during our concerts, especially Monteverdi's vesper: it was indeed a dream which came true. Music is a very important part of my life and these years would have been meaningless without it.

Thank to all the friends I met during my travels. Hopefully, there will be time to see all of you once again. Thanks to all the friends here in Padova, old and new, for being my family when I'm far from mine, for the magic dinners we had and the support I got from you when I was in need. Thanks to Cristina for being the best flatmate anyone would hope for: I miss you!!

Finally, thanks to my sister, to whom this thesis is dedicated, and my mother, since you both are the most important members of my family. They say every family has its own problems, anyway I would bet that during the last three years we have faced something more intense than usual. I know for sure that this work couldn't be completed without your support: to you I owe my deepest gratitude.

Padova, January 31, 2016
Marco Roda